Manipulating Energetic and Electronic Performance in Multicomponent Crystals through Discrete and Continuous Compositional Variation

by

Ren Alessandra Wiscons

A dissertation submitted in partial fulfillment
of the requirements for the degree of
Doctor of Philosophy
(Chemistry)
in the University of Michigan
2019

Doctoral Committee:

Professor Adam J. Matzger, Chair
Professor Bart M. Bartlett
Assistant Professor John T. Heron
Assistant Professor Charles C. L. McCrory

Ren A. Wiscons

renwis@umich.edu

ORCID iD: 0000-0002-8281-0343

Dedication

I often don’t give myself enough credit, so this one’s for me.

Acknowledgements

I would like to thank my mentor, Professor Adam J. Matzger, for pushing me to be better for the last four years of graduate school. I am aware that I can be frustrating to work with by having strong opinions but being quiet about them and all the while being generally indecisive. But I told him from the start that I did know I wanted to be a professor at a small college and, since then, I've felt like the two of us have been on the same page towards reaching that goal. I couldn't have asked for anything more.

I am thankful to my dissertation committee, Professors Bart Bartlett, John Heron, and Charles McCrory, for their support and suggestions throughout the years. In addition to their encouragement at each stage of my graduate career, I also don't want to underemphasize the impact of having additional friendly faces around campus.

It is because of Antek Wong-Foy and Leila Foroughi that I know scientists to be so much more than people who do research. They dedicate themselves so much to everything that goes into developing an environment in which doing research is even possible, whether providing support to the instruments or providing support to the graduate students. Though their methods can be unconventional on occasion, they're always effective and I can only hope to graduate with a fraction of the knowledge and dedication these two have. Thank you for your friendship, the coffee, and the bagels over the years.

I decided to major in chemistry in my junior year of college and I have three people to blame for this: Professors Jesse Rowsell, Rebecca Whalen, and Liso Ryno. They gave me

opportunities when I didn't deserve them and made space for me in their community when they didn't have to. It is because of them that I will likely spend my career trying to do the same for the next generation of students.

I feel quite lucky to have been mentored by the labmates who came before me and to have had the opportunity to share their wisdom with the present members of the Matzger lab. Jon Bennion taught me that being dedicated to my research doesn't mean that I have to give up who I am and I will always be grateful for that lesson. Kyle McDonald and Rosalyn Kent are constant sources of inspiration to engineer new intersections between STEM and the larger community that I live in. They both made it look absolutely effortless and I know better now. Kortney Kersten, Jake Boissonault, and Jialiu Ma brought an insane and boisterous environment into lab and I appreciated it every day even if I said otherwise. All of that said, I think that if I could have chosen two labmates with whom to share nearly all of the past four years, I still would've chosen Ryan Dodson and Derek Frank for valuing me as a friend rather than just a coworker. I would also like to thank Michael Bellas, Taylor Bramlett, Derek DuBois, Chris Swendris, and Maiko Lunn. They have all been fantastic labmates and mentees and always keep me on my toes with what in the world they decide to ask me next.

I would also like to acknowledge my friends within and outside of the department. Will Austin, Joe MacPhail, Justin Kang, and Kai Gardener are still my crew and while it's disappointing that we've been apart for the last four years, it's been awesome to see how their lives have evolved in that time. I always had the best conversations with Ryan Harding, Max Bilodeau, and Greg Rosenhauer. I am really proud to have been your friend during your time here and I am glad you were able to find your paths outside of the doctorate program. Jessica Yazarians and Matthew Hannigan I need to thank for helping me celebrate the best and get through the worst. These two have supported me more than they know. I also need to thank Molly MacInnes who is probably one of the best people and scientists that I know and I would like to acknowledge her for her constant support, friendship, and inspiring me to take responsibility for the decisions that I make around my balance between work and life. Taking responsibility was the first step towards finding my balance.

Finally, I would like to thank my family, Brad, Brenda, and Lucas. Though we have been separated by over 2,000 miles for eight years, they have provided me with the strength of character that has been critical up until the end.

Table of Contents

List of Tables

List of Figures

Abstract

Organic crystalline materials demonstrate a diversity of properties that arise from a balance between the composition and structural phase of the solid. While deconvoluting the effects that chemical composition, molecular conformation, intermolecular interactions, and packing forces can have on performance is a powerful tool towards developing solid-state design strategies for improved performance, separating the independent effects of these factors on bulk properties is a challenge. In rare cases, the composition of a crystalline material can be held constant while the structural phase is modified (polymorphism) or, conversely, the structural phase kept unaltered while the composition is varied. It is from these systems that a deeper mechanistic understanding of the physical origins that give rise to bulk properties can be extracted. This dissertation focuses on the identification of multicomponent crystalline systems that accept compositional variation, allowing the effects of composition and structural phase on performance to be separated. These studies have enabled reinvestigation of paradigms held in the areas of energetic hydrates and charge-transfer ferroelectrics.

Crystalline hydrates are multicomponent crystals in which one or more molecules of water occupy defined sites within the crystal lattice. The formation of crystalline hydrates has long been recognized to erode performance of traditional energetic materials (e.g. HMX, CL-20, tetryl) and is becoming a much more pervasive challenge for modern heterocyclic energetics. Unfortunately no single energetic compound was known to form a great enough diversity of crystalline hydrates to enable meaningful investigation of the effects of hydration on energetic

performance. The energetic compound 5,5'-dinitro-2*H*,2*H*'-3,3'-bi-1,2,4-triazole, DNBT, is found to produce a remarkable number of anhydrous and hydrate crystal forms, which is exploited to investigate the effects of hydration on energetic performance. It is found that hydrate formation leads to degradation of the energetic performance by decreasing the crystallographic density of the solid form without contributing to the heat release.

Ferroelectric behavior is exceedingly rare in organic charge-transfer (CT) cocrystals, a class of multicomponent crystalline materials formed between π-electron donating (*D*) and accepting (*A*) species. In the solid state, *D* and *A* demonstrate unequal sharing of electron density, leading to predominantly neutral ($<$ 0.5 electron) or predominantly ionic ($>$ 0.5 electron) charge-transfer states. Since the mid-1980s, ferroelectricity in this class of materials has been attributed to temperature-dependent transitions between neutral and ionic CT states, which has since served as a basis for design strategies towards the discovery of novel CT ferroelectrics. Unfortunately, this approach has failed to produce CT ferroelectrics that demonstrate room-temperature ferroelectricity. The CT cocrystal formed between acenaphthene (AN) and 2,3,5,6-tetrafluoro-7,7,8,8-tetracyanoquinodimethane (F_4TCNQ) is found to demonstrate room-temperature ferroelectricity without transitioning between neutral and ionic CT states. The absence of a neutral-ionic transition in AN-F_4TCNQ is further investigated through the formation of solid solutions based on the AN-F_4TCNQ structural phase. Ionic CT states are doped into AN-F_4TCNQ through the inclusion of dihydronaphtho[1,8*bc*]furan and dihydronaphtho[1,8*bc*]-thiophene, which is found to significantly increase the average ionicity but does not lead to a neutral-ionic transition. These results demonstrate that a material with the appropriate symmetry changes for ferroelectricity and intermediate ionicity does not necessarily show competitive ferroelectric performance, indicating the failure of conventional design strategies towards ferroelectric CT cocrystals to fully capture the factors relevant to ferroelectricity in this class of materials.

Chapter 1 : Compositional Variation in Energetic and Charge-Transfer Crystals

1.1 Multicomponent Organic Crystals

The properties exhibited by a crystalline solid arise from a balance between the chemical composition and structural phase of the material.[1] The incorporation of a new chemical species into a material leads not only to the emergence of properties attributable to the compositional change, but also properties that result from the formation of new intermolecular interactions and/or changes to the crystal packing arrangement. Generally, the independent effects that composition, intermolecular interactions, and crystal packing have on the performance of a material cannot be deconvoluted; however, in cases where crystal packing is unchanged (isomorphous) upon introduction of a new chemical species, structure-function relationships may be investigable. Within the area of solid-state organic materials, multicomponent crystallization broadly describes the formation of a crystalline solid containing two or more discrete chemical species occupying well-defined lattice positions (see Figure 1.1), although the ratio between the species can be discrete (stoichiometric) or continuously variable (non-stoichiometric).[2]

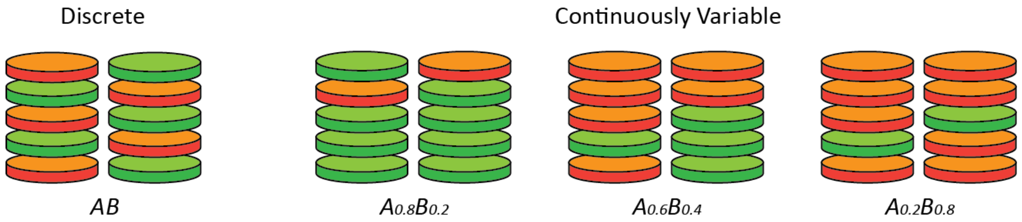

Figure 1.1. Diagram of Stoichiometric and Non-Stoichiometric Multicomponent Crystals

Green and orange discs represent two chemically distinct molecular species *A* and *B*. Multicomponent crystals with discrete compositions are stoichiometric and those with continuously variable compositions are non-stoichiometric.

1.1.1 Stoichiometric Multicomponent Crystals: Cocrystals and Solvates

Stoichiometric multicomponent crystals are crystalline solids containing two or more distinct molecular species in a well-defined stoichiometric ratio, such as a salt formed between two or more formally charged species in which the ratio between species is enforced by charge balance.[2, 3] In addition to salts, stoichiometric multicomponent crystals can be divided into two classes: cocrystals and crystalline solvates (see Figure 1.2).[3] Cocrystals are defined as stoichiometric multicomponent crystals in which all molecular species in the crystal lattice are neutral molecular solids when pure at standard temperature and pressure.[3] In contrast, a crystalline solvate is formed when at least one of the components is a liquid or gas when pure at standard temperature and pressure.[3] A recent investigation of the organic crystals deposited in the Cambridge Structural Database revealed that nearly 30% of all organic crystal structures are stoichiometric multicomponent crystals: salts (14%), solvates (19%), and/or cocrystals (4%).[3]

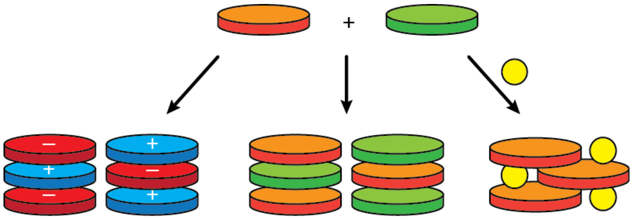

Figure 1.2. Diagram Differentiating between Salts, Cocrystals, and Solvates

The combination of the orange and green discs have three multicomponent crystallization outcomes: 1) the exchange of a proton or electron to form a salt (red and blue discs with formal charges); 2) a cocrystal of the orange and green discs; and 3) a solvate shown by the orange disc crystallizing with a solvent molecule (yellow circle).

Similar to single-component molecular crystals, multicomponent crystals are generally assembled through a combination of packing forces and non-covalent interactions that bring together functional groups with complementary electrostatic potentials, such as hydrogen-bonding[4] and π-stacking interactions[5].[2] In systems where identifying regions of electron density or deficiency is less obvious, calculation of electrostatic potential maps may be used to facilitate the selection of cocrystallization partners or retrospectively justify cocrystallization between molecular species in order to update design strategies and inform the selection of similar coformers in the future.[6] Developing robust design principles to specifically target and attenuate the physical properties of compounds of interest remains a challenge in all fields of solid-state organic chemistry, although significant improvements in performance have been achieved through multicomponent crystallization in the areas of pharmaceuticals,[7-10] energetics,[11-13] and molecular electronics[14] [15, 16] [17].

1.1.2 Non-stoichiometric Multicomponent Crystals: Solid Solutions

In rare cases, molecular dopants or impurities can be incorporated into an organic crystalline structural phase (host phase) at continuously variable concentrations[1] through occupation of interstices or substitutional replacement of molecular species present in the host phase (see Figure 1.3).[18] The material resulting from dopant incorporation is referred to as a solid solution. Solid solutions describe extrinsically defected materials that can accept relatively high concentrations of dopant species (>1-5 mol%) without introducing composition-dependent changes to the solid-state arrangement of chemical species in the material (e.g. crystal packing).[2, 19] While solid solutions can refer to crystalline or amorphous solids, discussion of amorphous solid solutions is beyond the scope of this research.

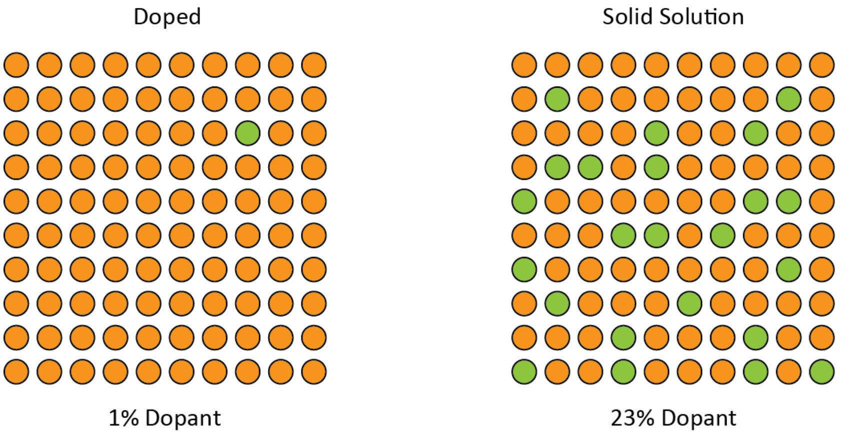

Figure 1.3. Diagram of Non-Stoichiometric Multicomponent Crystals

The orange and green circles represent molecules that can be combined at variable stoichiometries to produce a doped crystal with 1% dopant (green circle) or 23% dopant.

Solid solutions often demonstrate properties intermediate between those of the host and dopant, although in some cases, new properties can arise.[1] Utilizing solid solutions as a design strategy provides new opportunities to finely tune properties of molecular solids, while enabling investigation of structure-property relationships.[1] Unfortunately, applying solid solution formation as a general design approach to altering the performance of organic molecular solids presents several challenges that are less obvious in the field of inorganic metal and salt solid solutions, most notably the diversity of organic molecular structures,[20] anisotropy of electron density distribution about the surface of molecular species, and, in many cases, molecular flexibility. It is due to these factors, that crystallization of organic molecular species generally leads to purification of the solid (exclusion of dopants at significant concentrations), often precluding solid solution formation.[20]

1.1.3 The Effects of Solid Solutions on the Properties of Molecular Crystals

Despite the challenges associated with designing and synthesizing molecular solid solutions compared to inorganic solid solutions, several features, such as molecular similarity[21] and crystallographic isostructurality, can be sufficient indicators for potential solid solution formation between organic species. This reasoning has led to the discovery of several organic solid solutions, whose properties demonstrate the breadth and potential that this design approach can have on the performance of organic materials. Most notably, organic solid solutions have shown enhanced conductivity,[22] pyroelectricity,[23] crystallographic polarity,[24] optical absorbance,[25] dissolution rate,[26-29] and tuning of the melt temperature,[30] performance improvements that motivate the development of reliable design principles for the discovery of new solid solutions within other areas of molecular crystal engineering.

1.2 Energetic Materials

1.2.1 An Introduction to Energetic Materials

Energetic materials refer to a class of inorganic and organic compounds and mixtures (formulations) that rapidly react to release chemical energy as light, heat, sound, and gas.[31] Energetics can be differentiated from combustible materials (e.g. propane) because the energetic material or formulation contains a balance of fuel and oxidant that leads to decomposition without reaction with external sources of oxygen. This balance between fuel and oxidant is referred to as the oxygen balance (OB) and is one of several parameters that can be used to approximate how efficiently the energetic can decompose to neutral molecular species.[32]

$$\mathrm{OB} = -1600(M_\mathrm{g})^{-1}(2N_\mathrm{C}+(N_\mathrm{H}/2)+N_\mathrm{M}-N_\mathrm{O}),$$

wherein M_g is the molecular weight of the energetic and N_C, N_H, N_M, and N_O refer to the number of carbon, hydrogen, metal, and oxygen atoms present in the formula unit of the energetic.

Energetic materials can be subdivided into three classes based on the rate of chemical decomposition of the energetic: explosives, propellants, and pyrotechnics. Explosives release energy through detonation, in which the reaction front propagates faster than the speed of sound by compression-induced heating of unreacted material. In contrast, propellants deflagrate, showing sustained reaction traveling below the speed of sound by burning of unreacted material. Pyrotechnics are often a combination of explosives and propellants and are designed to produce a visual or audible effect for use in applications such as fireworks, airbags, and signal flares.

Explosives can be further classified as either primaries or secondaries,[33] differentiated by the sensitivity to impact of the explosive, although other properties, such as detonation performance (power) and thermal stability, are important considerations for distinguishing primary and secondary explosives as well. For example, the detonation velocity for primary explosives generally ranges from 3500-5500 m s^{-1},[34] while that for secondaries is usually between 5500-9000 m s^{-1}.[34] Primary explosives are typically metal salts, such as lead azide, lead syphnate, and more recently, copper (I) 5-nitrotetrazolate,[35] whereas secondary explosives are small organic compounds (see Figure 1.4), such as 2,4,6-trinitrotoluene (TNT), hexahydro-1,3,5-trinitro-*s*-triazine (RDX), and octahydro-1,3,5,7-tetranitro-1,3,5,7-tetrazocine (HMX). Recent advancements in primary energetics have focused on the development of ‘greener’ primaries that lack heavy metals,[36] while current research on secondaries has focused on synthesizing more powerful and less sensitive compounds.

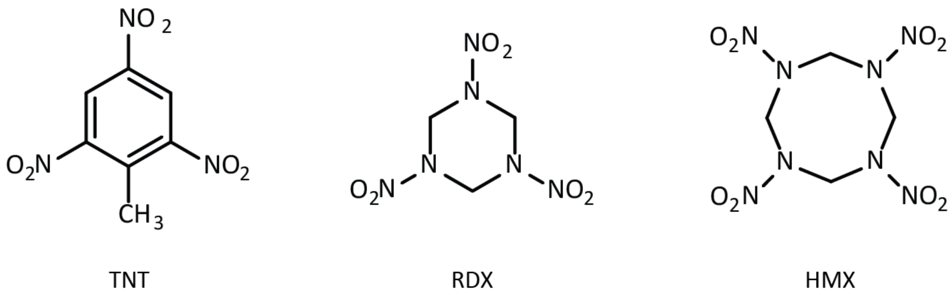

Figure 1.4. Molecular Structures of Common Secondary Explosives

Molecular structures of 2,4,6-trinitrotoluene (TNT, left), hexahydro-1,3,5-trinitro-*s*-triazine (RDX, center), and octahydro-1,3,5,7-tetranitro-1,3,5,7-tetrazocine (HMX, right).

1.2.2 Form Diversity of Energetic Materials and Effects on Performance

The power of an energetic material is often evaluated by determining the detonation velocity (V_d) and detonation pressure (P_d) of an energetic or energetic formulation. The detonation velocity and pressure of a novel energetic material can be measured experimentally through large-scale testing or approximated using thermochemical calculations that rely on the molar mass (M_g) and heat of detonation (Q) for the energetic as well as the moles of product gases predicted to result from detonation (N_g). The Kamlet-Jacobs equations[37] and derivations thereof have been used for theoretical determination of the detonation performance at particular charge densities (ρ_o).

$$V_d = 1.01(1 + 1.30\rho_o)\,(N_g(M_gQ)^{1/2})^{1/2}$$

$$P_d = 15.58\rho_o^2N_g(M_gQ)^{1/2}$$

When using theoretical calculations to determine detonation performance in academic settings, the charge density is conventionally equivalent to the theoretical maximum density for the energetic material (crystallographic density). The dependence of the detonation performance on crystallographic density leads to the understanding that differences in crystal packing can alter energetic performance if different crystal forms of the energetic species have different crystallographic densities.[31]

There are two common mechanisms by which the crystal packing of energetic compounds can be altered under standard crystallization conditions: polymorphism and hydrate formation. Polymorphism occurs when the same molecule or formula unit can crystallize into two or more distinct crystal structures,[3] whereas a crystalline hydrate describes a crystal structure in which one or more molecules of water occupy defined sites within the crystal lattice.[38] The energetic 2,4,6,8,10,12-hexanitro-2,4,6,8,10,12-hexaazoisowurtzitane (CL-20), for example, has three well-accepted polymorphs and a crystalline hydrate,[31] each with different crystallographic densities. Using the thermochemical code Cheetah 7.0,[39] ε-CL-20 is predicted to detonate 426 m s^{-1} faster than γ-CL-20 (see Table 1.1). HMX shows similar form diversity under standard crystallization conditions, which also leads to differences in detonation performance.[31] For this reason, controlling the solid forms of energetics that show a propensity towards polymorphism is necessary for ensuring reproducibility in performance. Similarly, hydrate formation is determinedly avoided as molecules of water trapped in the crystal lattice often leads to decreases in crystallographic density without contributing to heat release during detonation, degrading the detonation performance.

Table 1.1. CL-20 Solid Forms and Calculated Detonation Velocity, V_d

	Density (g cm^{-3})	V_d (m s^{-1})
γ-CL-20	1.92	9085
α-CL-20	1.97	9271
β-CL-20	1.99	9333
ε-CL-20	2.04	9511

1.2.3 Cocrystallization and Productive Solvate Formation in Energetic Materials

One approach that can be employed to limit the propensity for polymorphism and/or solid-state hydration as well as improve energetic performance is the formation of a multicomponent solid phase, such as a cocrystal or solvate. Salts are often avoided in the field of energetic materials as they can lead to hygroscopicity and dramatic changes to the thermal and impact sensitivities. In 2011, the Matzger group presented the first cocrystal between two energetic species in a 1:1 stoichiometric ratio, TNT/CL-20 (see Figure 1.5).[40] This cocrystal introduced the field of energetic materials to the concept that physical properties critical to the performance of the energetic could be improved through cocrystallization, such as a reduction in the impact sensitivity of the cocrystal relative to pure CL-20.

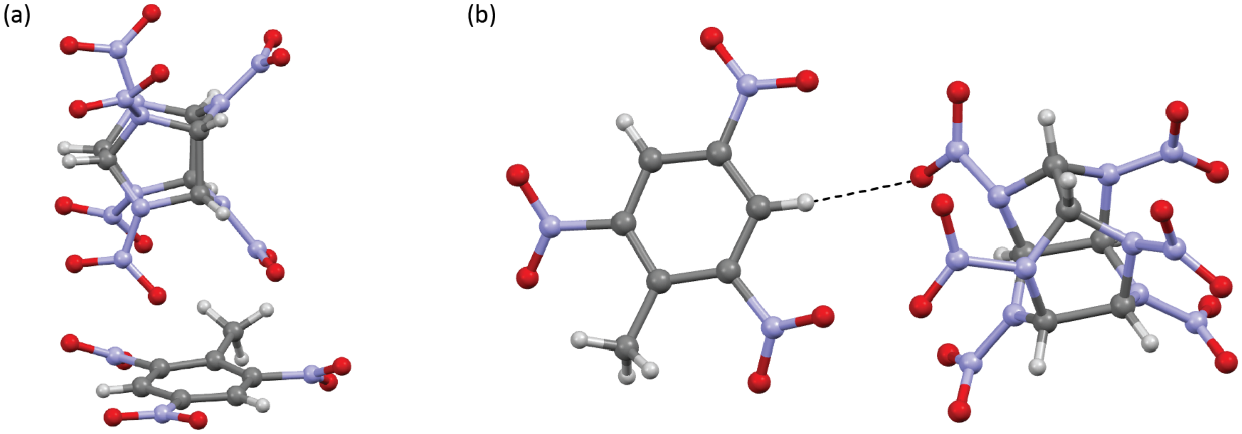

Figure 1.5. Interactions between TNT and CL-20 in the Cocrystal Structure

Two views of the TNT/CL-20 cocrystal highlighting the (a) nitro-π interactions and (b) non-classical hydrogen bonding interaction from TNT to CL-20.

The discovery of TNT/CL-20 brought forth an era of multicomponent materials in which both species contribute productively to the energetic performance,[32, 40-50] ultimately leading to the discovery of the most powerful non-nuclear explosive known today, the CL-20/HP solvate (HP = hydrogen peroxide) in 2016.[32] Multicomponent energetic materials are rarely designed based on supramolecular concepts or crystal engineering strategies because energetic compounds often lack functional groups that can participate in strong and directional intermolecular interactions (e.g. hydrogen bonding),[51] a challenge that has slowed the discovery of energetic-energetic cocrystals and solvates. That said, CL-20/HP was conceptualized based on substitutional replacement of the water molecules in α-CL-20 with molecules of hydrogen peroxide (see Figure 1.6). The simplicity of this approach seemed likely to lead to a general crystallization strategy for energetic hydrates, but unfortunately, unpublished results in our group have shown that formation of hydrogen peroxide solvates is not guaranteed for all energetic hydrates. In order to develop more general guidelines for hydrogen peroxide solvate formation, a more comprehensive understanding of energetic hydrate formation and the effects of hydration on detonation performance must first be developed.

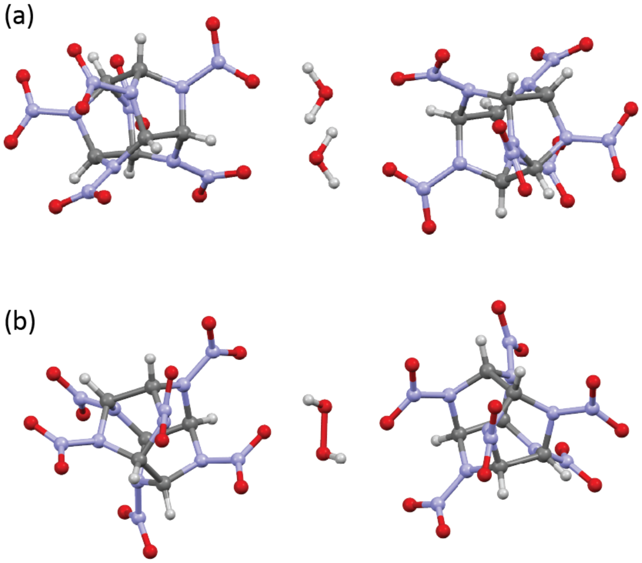

Figure 1.6. Substitutional Replacement of Water with Hydrogen Peroxide in α-CL-20

(a) The crystal structure of α-CL-20 showing the interaction between water molecules and molecules of CL-20 and (b) the CL-20/HP solvate highlighting the molecule of hydrogen peroxide replacing the two molecules of water.

1.3 Charge-Transfer Ferroelectric Materials

1.3.1 An Introduction to Charge-Transfer Cocrystals

Charge-transfer cocrystals describe a class of multicomponent crystalline solids that typically contain two electronically complementary molecular components that display unequal sharing of an electron in the solid-state.[52] The degree of charge-transfer is primarily influenced by the relative energies of the ionization potential of the donor and the electron affinity of the acceptor, which can be approximated by the energies of the highest occupied molecular orbital (HOMO) and lowest unoccupied molecular orbital (LUMO), respectively.[52, 53] The relative closeness in energy of the HOMO and LUMO positions of the donor and acceptor molecules generally gives rise to stark color changes in the complexed state compared to the isolated materials, providing a convenient and reliable visual cue for successful cocrystallization.

There are two models (see Figure 1.7) commonly invoked to describe the sharing of electron density (degree of charge-transfer, ionicity, ρ) between the donor (D) and acceptor (A) molecules: 1) each DA pair related by symmetry in crystal lattice displays identical partial electron-transfer through the formation of new frontier molecular orbitals in the complexed state that show HOMO character on A and LUMO character on the D; 2) alternatively, each charge-transfer cocrystal contains two types of DA pairs, those that show no charge-transfer and those that are fully ionized and the proportion of neutral and ionized DA pairs average to a partial charge-transfer value identical to that predicted by the first model.[54] Advancements in computational treatment of orbital exchange has led to the consensus that the first model of charge-transfer is a more accurate representation of charge-transfer in the studied systems. Regardless of which charge-transfer model is being employed, a charge-transfer cocrystal that displays an average degree of charge-transfer of less than half an electron (ρ < 0.5 e) is considered primarily neutral, while a charge-transfer cocrystal that displays an average degree of charge-transfer that is greater than half an electron ($\rho > 0.5$ e) is considered primarily ionic.[52, 55]

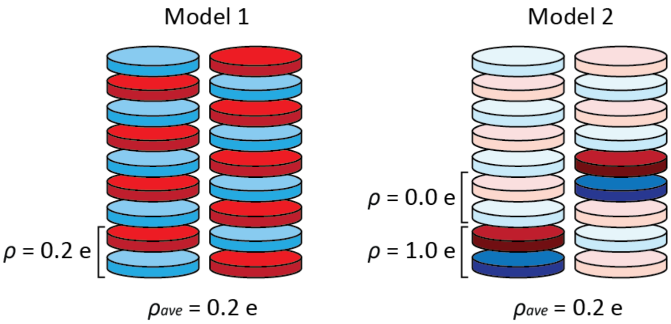

Figure 1.7. The Two Models of Charge-Transfer Ionicities in CT Cocrystals

Two models of charge-transfer in which each disc represents a CT donor (red) or acceptor (blue) and the light/darkness of the color corresponds to the degree of CT. Model 1 shows that all CT pairs show and equal and intermediate ionicity and Model 2 only shows fully neutral or fully ionic pairs.

While the field of charge-transfer cocrystals almost exclusively refers to π-electron charge-transfer between donor and acceptor molecules, instances of σ-charge transfer have also been reported (e.g. halogen bonding interactions) but are beyond the scope of the research described here. Within the field of planar π-electron charge-transfer cocrystals (i.e. CT cocrystals), intermolecular interactions present in the solid-state affect the localization of the transferred charge,[56] leading to materials properties that range from conduction[57] to polarization switching[58] for use in lightweight metal-free electronics. For example, CT cocrystals that show a segregated stacking motif free of stacking distortions are generally conductive,[57] while CT cocrystals that adopt alternating or mixed stacking motifs generally form semiconductors[56] or dielectrics depending on whether the stack is distorted or free of distortions (see Figure 1.8).[52] Unlike multicomponent energetic materials, cocrystallization of π-electron donor and acceptor molecules is almost always guaranteed by the electrostatic attraction between the two species;

however, these materials rarely display the appropriate combination of crystal packing and partial charge-transfer to demonstrate electronic properties of interest to the electronic materials community.

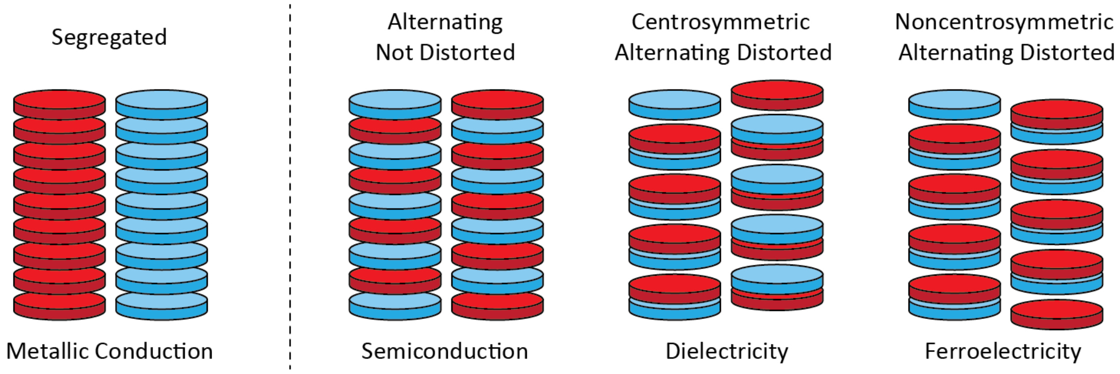

Figure 1.8. Common Packing Motifs for CT Cocrystals and Associated Properties

Common packing motifs and predicted electronic behavior for CT cocrystals where the red discs represent CT donors and the blue discs represent CT acceptors.

1.3.2 An Introduction to Ferroelectricity

Of particular interest is the identification of ferroelectricity in CT cocrystals. Ferroelectric materials adopt noncentrosymmetric crystal symmetries, leading to a measurable separation of positive and negative charge that gives rise to a bulk polarization vector.[59, 60] The polarization direction of the ferroelectric material can be aligned and redirected by an applied coercive electric field, E_C, and the new charge distribution is maintained as the remanent polarization when the E_C is removed.[59, 60] This phenomenon can be exploited for a diversity of electronic properties, most notably data storage but also thermal and mechanical sensing. When heated above a temperature termed the Curie temperature (T_C), the individual dipoles of each unit cell become disordered and can no longer remain aligned upon removal of the E_C.[59] Unfortunately, due to the symmetry requirements necessary for ferroelectricity, ferroelectric CT cocrystals are rare and those that are known show low working temperature ranges barred by cryogenic T_C values, precluding practical application.

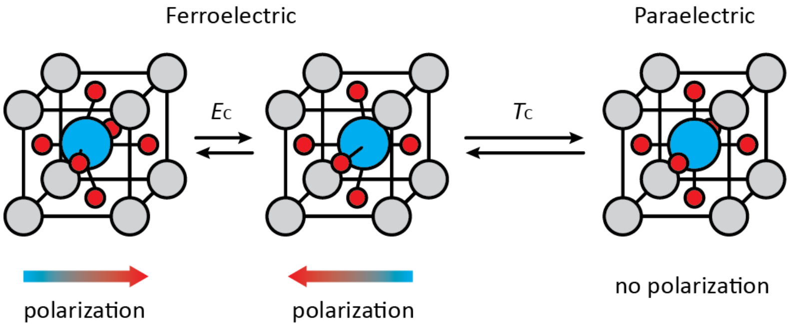

Figure 1.9. Ferroelectricity in a Perovskite, Barium Titanate

The ferroelectric and paraelectric phases of a unit cell of barium titanate. The grey circles represent Ba^{2+}, the red circles represent O^{2-}, and the blue circles represent Ti^{4+}. In the ferroelectric phase, the Ti^{4+} cation is displaced leading to the polarization vector drawn below the unit cells. The polarization vector can be switched by applying a coercive field, E_C, but when heated above the Curie temperature, T_C, the material has no polarization vector and is considered paraelectric.

1.3.3 A Brief History of Ferroelectric Charge-Transfer Cocrystals

In 1980, the first observation of CT cocrystals reversibly transitioning between primarily neutral and primarily ionic states was reported by Torrance *et al.*.[61] It was found that applying pressure to several neutral CT cocrystals predicted to be close to the border between neutral and ionic states gave rise to a color change that was attributed to a change in the ionicity.[61] The pressure-induced color change for the CT cocrystal formed between tetrathiafulvalene and chloranil (TTF-CA) was investigated using solid-state absorption spectroscopy and by comparing the shift in the spectrum upon applying pressure to TTF-CA to the solution-phase absorption spectra of the ionic standards $[TTF^+][Br^-]$ and $[K^+][CA^-]$.[61] Submitted in the same week was a manuscript by Batail *et al.* detailing the crystallographic origins of this electronic transition induced instead by temperature rather than pressure.[62] It was found that below 85 K, TTF-CA shows alternating short and long π-stacking distances attributed to dimerization of ionic D^+A^- pairs as well as non-classical C=O···H-C hydrogen bonds that are both absent above 85 K, leading to the neutralization of the *DA* pair. The transition between the low-temperature ionic and high-temperature neutral phase is associated with a change in space group from *Pn* to $P2_1/n$.

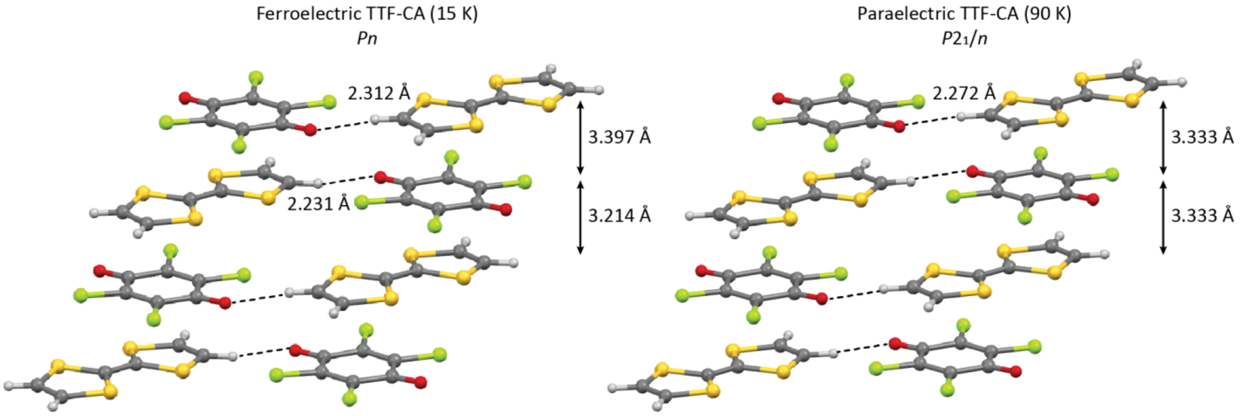

Figure 1.10. Low and High-Temperature Crystal Structures of TTF-CA

The ferroelectric (low-temperature) and paraelectric (high-temperature) phases of TTF-CA with intermolecular non-classical hydrogen bonding and π-stacking distances given for each structure. Both the hydrogen bonding and π-stacking distances are asymmetrical (have two measured values) at low temperature and symmetrize (one measured value) at high temperature.

In 1987, the pressure-induced ionic phase of TTF-CA was described as having antiparallel domain structures similar to those of well-known inorganic ferroelectric materials by Kaneko *et al*..[63] TTF-CA was first described as ferroelectric by Tokura *et al*. in 1989,[64] which was later confirmed with a polarization hysteresis loop at 54 K.[58] Low-temperature (< 77 K) ferroelectricity was also confirmed in structurally-related CT cocrystals formed between TTF and various halobenzoquinones (e.g. TTF-$QBrCl_3$ and TTF-BA, where $QBrCl_3$ = bromotrichloro-*p*-benzoquinone and BA = bromanil).[58, 65]

The ferroelectricity confirmed for the TTF-CA cocrystal is most often ascribed to the neutral-to-ionic transition of the *DA* pair ($D^+A^- D^+A^- D^+A^-$ to *D A D A D A*),[58] although additional CT complexes presented in Torrance *et al*.'s original report that were shown to undergo neutral-to-ionic transitions do not show ferroelectric behavior. Additionally, examples of CT cocrystals that have been shown to undergo neutral-to-ionic transitions do not undergo crystallographic Peierls-type distortions as a result of the ionicity change.[55, 66] Given the extensive studies on TTF-CA, the predominant design mechanism towards producing novel ferroelectric CT cocrystals is to produce a material that undergoes a neutral-to-ionic transition, as this transition has been assumed to be the driving force for polarization switching; however, this approach has failed to produce CT cocrystals that demonstrate room temperature ferroelectricity. In order to more reliably design room temperature ferroelectric CT cocrystals, the role of the neutral-to-ionic transition on polarization switching must be clarified.

Figure 1.11. Peierls Distortion in the Model System and TTF-CA

Diagram of a Peierls distortion in a chain of metals (grey spheres, left) and in CT cocrystals (right), in which the red discs represent CT donor molecules and the blue discs represent CT acceptor molecules.

1.4 Organization of the Thesis

This thesis focuses on taking advantage of compositional variation to design improved energetic and ferroelectric materials as well as further investigate structure-property relationships within the context of these materials. Confirming successful doping, substitutional replacement, and solid solution formation is challenging as no single characterization technique can be used to identify molecular substitution and determine structural similarity. Additionally, solid solution formation often leads to characterization data that only subtly deviates from that of the host material. Even in the area of cocrystallization, where the formation of a true multicomponent crystal is generally much more obvious than substitutional solid solution formation, there still exist several misunderstandings with respect to rigorous characterization that have led to false reports of novel cocrystals within the field of energetic materials. Chapter 2 revisits these reports and provides guidelines for 'best practices' for cocrystal identification in the absence of single-crystal X-ray data.

Chapter 3 describes the hydration behavior of the energetic azole 5,5'-dinitro-2*H*,2*H*'-3,3'-bi-1,2,4-triazole (DNBT). DNBT was found to form two anhydrous polymorphs as well as six different hydrate forms, an unprecedented number of hydrates that were used to investigate the effects of hydration on detonation performance. It was found that the degree of hydration leads to a linear decrease in the crystallographic density, which results in decreases in the detonation velocity and pressure. This hydration behavior is exploited to achieve a high-performing phase-pure DNBT form in bulk through the substitutional replacement of the water molecules with molecules of hydrogen peroxide. The discussions of hydration and hydrogen peroxide formation are particularly relevant to the next generation of explosives, which show a greater susceptibility to hydrate formation, making high-performance anhydrous forms difficult to access at scale.

Chapter 4 revisits the conventional design techniques employed to target ferroelectricity in organic cocrystals within the context of the charge-transfer cocrystal formed between acenaphthene and 2,3,5,6-tetrafluoro-7,7,8,8-tetracyanoquinodimethane (AN-F_4TCNQ). AN-F_4TCNQ was found to exhibit room temperature ferroelectricity and shows polarization switching facilitated by non-charge-transfer interactions (reversible order-disorder transition of AN), a departure from design paradigms currently employed around displacive ferroelectrics. The results of this chapter suggest diversification of the principles considered towards the design of displacive ferroelectrics is necessary.

Chapter 5 explores solid solution formation between four charge-transfer cocrystals, yielding a quaternary solid solution with a tunable degree of charge-transfer. Computational prediction of the density of states and band diagrams of these materials reveals that the structural phase adopted by the solid solution may show semiconductivity along π-stacking (charge-transfer) direction of the crystal (*a*-axis). The data presented in this chapter suggest that molecular size differences and isomorphism between structural phases contribute to the selectivity for dopant incorporation in organic solid solutions. Finally, it is shown that controlling the ratio of dopant and host molecules present in solution during crystal growth can lead to compositional zoning in crystals that may lead to new approaches to passivation and electrode deposition for organic molecular electronics, two major limitations currently limiting the field of organic semiconductors.

Chapter 6 extends the work of both Chapters 4 and 5 by combining the concepts of charge-transfer ferroelectric cocrystals with charge-transfer solid solutions to investigate the role of the degree of charge-transfer on the Curie temperature and remanent polarization. It was found that the Curie temperature can be varied dramatically by incorporation of a dopant, while the remanent polarization remains relatively unaffected. In addition to characterizing the effects of solid solution formation on the ferroelectric performance, this chapter examines the composition-dependent changes to the structural phase that result from solid solution formation from nonisostructural cocrystalline phases.

1.5 References

1. Lusi, M., Engineering Crystal Properties through Solid Solutions. *Cryst. Growth Des.* **2018**, *18*, 3704-3712.
2. Steed, J. W.; Atwood, J. L., *Supramolecular Chemistry*. 2 ed.; Wiley: Oxford, 2009; p 1002.
3. Kersten, K. M.; Kaur, R.; Matzger, A. J., Survey and analysis of crystal polymorphism in organic structures. *IUCrJ* **2018**, *5*, 124-129.
4. Jeffrey, G. A., *An introduction to hydrogen bonding*. Oxford University Press: New York, 1997.
5. Hunter, C. A.; Lawson, K. R.; Perkins, J.; Urch, C. J., Aromatic interactions. *J. Chem. Soc., Perkin Trans.* **2001**, *2*, 651-669.
6. Musumeci, D.; Hunter, C. A.; Prohens, R.; Scuderia, S.; McCabe, J. F., Virtual cocrystal screening. *Chem. Sci.* **2011**, 883-890.
7. Fleischman, S. G.; Kuduva, S. S.; McMahon, J. A.; Moulton, B.; Walsh, R. D. B.; Rodríguez-Hornedo, N. r.; Zaworotko, M. J., Crystal Engineering of the Composition of Pharmaceutical Phases: Multiple-Component Crystalline Solids Involving Carbamazepine. *Cryst. Growth Des.* **2003**, 909-919.
8. Porter III, W. W.; Elie, S. C.; Matzger, A. J., Polymorphism in Carbamazepine Cocrystals. *Cryst. Growth Des.* **2008**, *8*, 14-16.
9. Sanphui, P.; Goud, N. R.; Khandavilli, U. B. R.; Nangia, A., Fast Dissolving Curcumin Cocrystals. *Cryst. Growth Des.* **2011**, *11*, 4135-4145.
10. Schultheiss, N.; Newman, A., Pharmaceutical Cocrystals and Their Physicochemical Properties. *Cryst. Growth Des.* **2009**, *9*, 2950-2967.
11. Landenberger, K. B.; Matzger, A. J., Cocrystal Engineering of a Prototype Energetic Material: Supramolecular Chemistry of 2,4,6-Trinitrotoluene. *Cryst. Growth Des.* **2010**, *10*, 5341-5347.
12. Landenberger, K. B.; Matzger, A. J., Cocrystals of 1,3,5,7-Tetranitro-1,3,5,7-tetrazacyclooctane (HMX). *Cryst. Growth Des.* **2012**, *12*, 3603-3609.
13. Millar, D. I. A.; Maynard-Casely, H. E.; Allan, D. R.; Cumming, A. S.; Lennie, A. R.; Mackay, A. J.; Oswald, I. D. H.; Tang, C. C.; Pulham, C. R., Crystal engineering of energetic materials: Co-crystals of CL-20. *CrystEngComm* **2012**, *14*, 3742-3749.
14. Kapadia, P. P.; Ditzler, L. R.; Baltrusaitis, J.; Swenson, D. C.; Tivanski, A. V.; Pigge, F. C., Semiconducting Organic Assemblies Prepared from Tetraphenylethylene Tetracarboxylic Acid and Bis(pyridine)s via Charge-Assisted Hydrogen Bonding. *J. Am. Chem. Soc.* **2011**, *133*, 8490-8493.
15. Sato, S.; Nikawa, H.; Seki, S.; Wang, L.; Luo, G.; Lu, J.; Haranaka, M.; Tsuchiya, T.; Nagase, S.; Akasaka, T., A Co-Crystal Composed of the Paramagnetic Endohedral Metallofullerene La@C82 and a Nickel Porphyrin with High Electron Mobility *Angew. Chem. Int. Ed.* **2012**, *51*, 1589-1591.
16. Sokolov, A. N.; Friščić, T.; MacGillivray, L. R., Enforced Face-to-Face Stacking of Organic Semiconductor Building Blocks within Hydrogen-Bonded Molecular Cocrystals. *J. Am. Chem. Soc.* **2006**, *128*, 2806-2807.

17. Yan, D.; Delori, A.; Lloyd, G. O.; Friščić, T.; Day, G. M.; Jones, W.; Lu, J.; Wei, M.; Evans, D. G.; Duan, X., A Cocrystal Strategy to Tune the Luminescent Properties of Stilbene- Type Organic Solid-State Materials. *Angew. Chem. Int. Ed.* **2011**, *50*, 12483-12486.
18. Nesse, W. D., *Introduction to Mineralogy*. Oxford University Press: New York, 2000.
19. West, A. R., *Solid State Chemistry and its Applications*. 2 ed.; Wiley: New York, 2014.
20. Sada, K.; Inoue, K.; Tanaka, T.; Epergyes, A.; Tanaka, A.; Tohnai, N.; Matsumoto, A.; Miyata, M., Multicomponent Organic Alloys Based on Organic Layered Crystals. *Angew. Chem. Int. Ed.* **2005**, *44*, 7059-7062.
21. Kitaigorodsky, A. I., *Mixed Crystals*. Springer: Berlin, 1984.
22. Engler, E. M.; Scott, B. A.; Etemad, S.; Penney, T.; Patel, V. V., Organic Alloys: Synthesis and Properties of Solid Solutions of Tetraselenafulvalene-Tetracyano-*p*-quinodimethane (TSeF-TCNQ) and Tetrathiafulvalene-Tetracyano-*p*-quinodimethane (TTF-TCNQ). *J. Am. Chem. Soc.* **1977**, *99*, 5909-5916.
23. Vaida, M.; Shimon, L. J. W.; Van Mil, J.; Ernst-Cabrera, K.; Addadi, L.; Leiserowitz, L.; Lahav, M., Absolute Asymmetric Photochemistry Using Centrosymmetric Single Crystals. The Host/Guest System (*E*)-Cinnamamide/(*E*)-Cinnamic Acid. *J. Am. Chem. Soc.* **1989**, *111*, 1029-1034.
24. Gervais, C.; Wüst, T.; Hulliger, J., Polarity of Organic Supramolecular Materials: A Tunable Crystal Property. *J. Phys. Chem. B* **2005**, *109*.
25. Morimoto, M.; Kobatake, S.; Irie, M., Multicolor Photochromism of Two- and Three-Component Diarylethene Crystals. *Cryst. Growth Des.* **2017**, *17*, 3040-2047.
26. Cherukuvada, S.; Nangia, A., Eutectics as improved pharmaceutical materials: design, properties and characterization. *Chem. Commun.* **2014**, *50*, 906-923.
27. Goldberg, A. H.; Gibaldi, M.; Kanig, J. L., Increasing Dissolution Rates and Gastrointestinal Absorption of Drugs via solid Solutions and Eutectic mixtures II: Experimental Evaluation of a Eutectic Mixture: Urea-acetaminophen System. *J. Pharm. Sci.* **1966**, *55*, 482-487.
28. Goldberg, A. H.; Gibaldi, M.; Kanig, J. L., Increasing dissolution rates and gastrointestinal absorption of drugs via solid solutions and eutectic mixtures III: Experimental evaluation of griseofulvin—succinic acid solid solution. *J. Pharm. Sci.* **1966**, *55*, 487-492.
29. Goldberg, A. H.; Gibaldi, M.; Kanig, J. L.; Mayersohn, M., Increasing dissolution rates and gastrointestinal absorption of drugs via solid solutions and eutectic mixtures. IV. Chloramphenicol--urea system. *J. Pharm. Sci.* **1966**, *55*, 581-583.
30. Romasanta, A. K. S.; Braga, D.; Duarte, M. T.; Grepioni, F., How similar is similar? Exploring the binary and ternary solid solution landscapes of p-methyl/chloro/bromo-benzyl alcohols. *CrystEngComm* **2017**, *19*, 653-660.
31. Bernstein, J., *Polymorphism in Molecular Crystals*. Oxford Science Publications: New York, 2002.
32. Bennion, J. C.; Chowdhury, N.; Kampf, J. W.; Matzger, A. J., Hydrogen Peroxide Solvates of 2,4,6,8,10,12-Hexanitro-2,4,6,8,10,12-hexaazaisowurtzitane. *Angew. Chem. Int. Ed.* **2016**, *55*, 13118-13121.
33. Cooper, P. W.; Kurowski, S. R., *Introductions to the Technology of Explosives*. VCH: New York, 1996.
34. Akhavan, J., *The Chemistry of Explosives*. 2 ed.; The Royal Society of Chemistry: Cambridge, UK, 2004.
35. Klapötke, T. M., *Chemistry of High-Energy Materials*. 2 ed.; Walter de Gruyter: Berlin/Boston, 2012.

36. Fronabarger, J. W.; Williams, M. D.; Sanborn, W. B.; Bragg, J. G.; Parris, D. A.; Bichay, M., DBX-1 – A Lead Free Replacement for Lead Azide. *Propellants Explos. Pyrotech.* **2011**, *36*, 541-550.
37. Kamlet, M. J.; Jacobs, S. J., Chemistry of Detonations. I. A Simple Method for Calculating Detonation Properties of C–H–N–O Explosives. *J. Chem. Phys.* **1968**, *48*, 23-35.
38. Damron, J. T.; Kersten, K. M.; Pandey, M. K.; Nishiyama, Y.; Matzger, A. J.; Ramamoorthy, A., Role of Anomalous Water Constraints in the Efficacy of Pharmaceuticals Probed by ^{1}H Solid-State NMR. *ChemistrySelect* **2017**, *2*, 6797-6800.
39. Cheetah 7.0 calculations were performed with the Sandia JCZS product library revision 32
40. Bolton, O.; Matzger, A. J., Improved Stability and Smart-Material Functionality Realized in an Energetic Cocrystal. *Angew. Chem. Int. Ed.* **2011**, *50*, 8960-8963.
41. Bolton, O.; Simke, L. R.; Pagoria, P. F.; Matzger, A. J., High Power Explosive with Good Sensitivity: A 2:1 Cocrystal of CL-20:HMX. *Cryst. Growth Des.* **2012**, *12*, 4311-4313.
42. Landenberger, K. B.; Bolton, O.; Matzger, A. J., Two Isostructural Explosive Cocrystals with Significantly Different Thermodynamic Stabilities. *Angew. Chem. Int. Ed.* **2013**, *52*, 6468-6471.
43. Landenberger, K. B.; Bolton, O.; Matzger, A. J., Energetic–Energetic Cocrystals of Diacetone Diperoxide (DADP): Dramatic and Divergent Sensitivity Modifications via Cocrystallization. *J. Am. Chem. Soc.* **2015**, *137*, 5074-5079.
44. Bennion, J. C.; McBain, A.; Son, S. F.; Matzger, A. J., Design and Synthesis of a Series of Nitrogen-Rich Energetic Cocrystals of 5,5′-Dinitro-2H,2H′-3,3′-bi-1,2,4-triazole (DNBT). *Cryst. Growth Des.* **2015**, *15*, 2545-2549.
45. Yang, Z. W.; Li, H. Z.; Zhou, X. Q.; Zhang, C. Y.; Huang, H.; Li, J. S.; Nie, F. D., Characterization and Properties of a Novel Energetic–Energetic Cocrystal Explosive Composed of HNIW and BTF. *Cryst. Growth Des.* **2012**, *12*, 5155-5158.
46. Guo, C.; Zhang, H.; Wang, X.; Liu, X.; Sun, J., Study on a novel energetic cocrystal of TNT/TNB. *J. Mater. Sci.* **2013**, *48*, 1351-1357.
47. Wang, Y.; Yang, Z.; Li, H.; Zhou, X.; Zhang, Q.; Wang, J.; Liu, Y., A Novel Cocrystal Explosive of HNIW with Good Comprehensive Properties. *Propellants Explos. Pyrotech.* **2014**, *39*, 590-596.
48. Yang, Z.; Wang, Y.; Zhou, J.; Li, H.; Huang, H.; Nie, F., Preparation and Performance of a BTF/DNB Cocrystal Explosive. *Propellants Explos. Pyrotech.* **2014**, *39*, 9-13.
49. Zhang, H.; Guo, C.; Wang, X.; Xu, J.; He, X.; Liu, Y.; Liu, X.; Huang, H.; Sun, J., Five Energetic Cocrystals of BTF by Intermolecular Hydrogen Bond and π-Stacking Interactions. *Cryst. Growth Des.* **2013**, *13*, 679-687.
50. Wu, J.-T.; Zhang, J.-G.; Li, T.; Li, Z.-M.; Zhang, T.-L., A novel cocrystal explosive NTO/TZTN with good comprehensive properties. *RSC Adv.* **2015**, *5*, 28354-28359.
51. Wiscons, R. A.; Matzger, A. J., Evaluation of the Appropriate Use of Characterization Methods for Differentiation between Cocrystals and Physical Mixtures in the Context of Energetic Materials. *Cryst. Growth Des.* **2017**, *17*, 901-906.
52. Goetz, K. P.; Vermeulen, D.; Payne, M. E.; Kloc, C.; McNeil, L. E.; Jurchescu, O. D., Charge-transfer complexes: new perspectives on an old class of compounds. *J. Mater. Chem. C* **2014**, *2*, 3065-3076.
53. Bredas, J.-L., Mind the Gap! *Mater. Horiz.* **2014**, *1*, 17-19.
54. Kampar, E.; Neilands, O., Degree of Charge Transfer in Donor–Acceptor Systems of the π–π Type. *Russ. Chem. Rev.* **1986**, *55*, 334-342.

55. Castagnetti, N.; Masino, M.; Rizzoli, C.; Girlando, A.; Rovira, C., Mixed stack charge transfer crystals: Crossing the neutral-ionic borderline by chemical substitution. *Phys. Rev. Mater.* **2018**, *2*, 024602.
56. Zhu, L.; Yi, Y.; Fonari, A.; Corbin, N. S.; Coropceanu, V.; Bredas, J.-L., Electronic Properties of Mixed-Stack Organic Charge-Transfer Crystals. *J. Phys. Chem. C* **2014**, *118*, 14150-14156.
57. Ferraris, J.; Cowan, D. O.; Walatka, V.; Perlstein, J. H., Electron transfer in a new highly conducting donor-acceptor complex. *J. Am. Chem. Soc.* **1973**, *95*, 948-949.
58. Kobayashi, K.; Horiuchi, S.; Kumai, R.; Kagawa, F.; Murakami, Y.; Tokura, Y., Electronic Ferroelectricity in a Molecular Crystal with Large Polarization Directing Antiparallel to Ionic Displacement. *Phys. Rev. Lett.* **2012**, *108*, 237601.
59. Hill, N. A., Why Are There So Few Magnetic Ferroelectrics? *J. Phys. Chem. B* **2000**, *104*, 6694-6709.
60. Tayi, A. S.; Kaeser, A.; Matsumoto, M.; Aida, T.; Stupp, S. I., Supramolecular ferroelectrics. *Nat. Chem.* **2015**, *7*, 281-294.
61. Torrance, J. B.; Vazquez, J. E.; Mayerle, J. J.; Lee, V. Y., Discovery of a Neutral-to-Ionic Phase Transition in Organic Materials. *Phys. Rev. Lett.* **1981**, *46*, 253-257.
62. Batail, P.; LaPlaca, S. J.; Mayerle, J. J.; Torrance, J. B., Structural characterization of the neutral-ionic phase transition in tetrathiafulvalene-chloranil: evidence for C-H···O hydrogen bonding. *J. Am. Chem. Soc.* **1981**, *103*, 951-953.
63. Kaneko, Y.; Tanuma, S.; Tokura, Y.; Koda, T.; Mitani, T.; Saito, G., Optical reflectivity spectra of the mixed-stack organic charge-transfer crystal tetrathiafulvalene-p-chloranil under hydrostatic pressure. *Phys Rev B Consens. Matter* **1987**, *35*, 8024-8029.
64. Tokura, Y.; Koshihara, S.; Iwasa, Y.; Okamoto, H.; Komatsu, T.; Koda, T.; Iwasawa, N.; Saito, G., Domain-wall dynamics in organic charge-transfer compounds with one-dimensional ferroelectricity. *Phys Rev. Lett.* **1989**, *63*, 2405-2408.
65. Horiuchi, S.; Kobayashi, K.; Kumai, R.; Minami, N.; Kagawa, F.; Tokura, Y., Quantum ferroelectricity in charge-transfer complex crystals. *Nat. Commun.* **2015**, *6*, 7469.
66. Lieffrig, J.; Jeannin, O.; Frąckowiak, A.; Olejniczak, I.; Świetlik, R.; Dahaoui, S.; Aubert, E.; Espinosa, E.; Auban-Senzier, P.; Fourmigué, M., Charge-Assisted Halogen Bonding: Donor–Acceptor Complexes with Variable Ionicity. *Chem. Euro. J.* **2013**, *19*, 14804-14813.

Chapter 2 : Differentiation between Cocrystals and Physical Mixtures in Energetic Materials*

2.1 Introduction

Energetic materials require an appropriate balance of fuel and oxidizer to achieve a high energy density and high detonation velocity.[1,2] Additional desirable characteristics of energetic materials include controllable impact sensitivity, insensitivity towards thermal shock, resistance towards the spontaneous formation of hydrates, and melt castability. Many of these attributes are traditionally tuned through chemical functionalization of existing, and synthesis of novel, energetic compounds. However, scaling syntheses of energetic compounds to industrial volumes for use in military and civilian settings is a time consuming and expensive process with no guarantee of success. For this reason, relatively few new energetic materials have been fielded in the past few decades. Cocrystallization provides a distinct method by which to tune the physical properties of existing energetic compounds and circumvents additional synthetic steps by leveraging established energetic materials and combining them in new modes in the solid state.

A cocrystal can be defined as a crystal in which two or more neutral molecular components interact noncovalently, typically in a defined stoichiometric ratio.[3,4] Within the last decade, formation of multicomponent materials (cocrystals, solvates, and salts) from two energetic molecules has become an increasingly employed strategy to tune the physical characteristics of energetic materials.[5-16] Unfortunately, many energetic compounds tend to form solvates and exhibit extensive polymorphism, which can lead to confusion during the discovery and characterization of novel energetic cocrystals.[7,17] Octahydro-1,3,5,7-tetranitro-1,3,5,7-

---

* Published: Wiscons, R. A.; Matzger, A. J. *Cryst. Growth Des.* **2017**, *17*, 901-906

tetrazocine (HMX) has three polymorphs (α-, β-, δ-),[18] and numerous solvated forms (including γ-, HMX hydrate),[19,20] while 2,4,6,8,10,12-hexanitro-2,4,6,8,10,12-hexaazaisowurtzitane (CL-20) forms three polymorphs (β-, γ-, ε-), one hydrate (α-)[17,21] and additional solvated forms.[6,22]

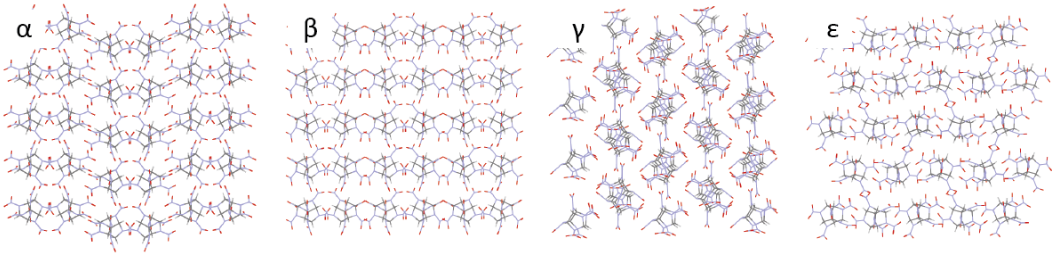

Figure 2.1. Solid-state Packing Motifs for the Polymorphs of CL-20

In this paper experimental claims of forming cocrystals from two energetic components are critically assessed.[23] Although single-crystal X-ray diffraction (SCXRD) measurement can provide unambiguous evidence for the formation of a cocrystal, this technique is not suitable for all cocrystals formed by the many different techniques employed for cocrystallization. Therefore, authors have sought to employ techniques including morphological observations, infrared (IR)/Raman spectroscopy, and powder XRD to substantiate claims for the existence of new phases. Upon careful reinterpretation of these observations, it is found that characterization data for many of the claimed energetic cocrystals in the literature are more consistent with a physical mixture of multiple components than with a new cocrystalline material. The limitations of these techniques will be addressed within the context of novel energetic-energetic cocrystal discovery and appropriate application these characterization techniques will also be discussed.

2.2 Discussion

Discovering new cocrystalline materials formed from two energetic compounds is challenging due to the functional groups common to energetics and their limited interaction modes.[19] Nitro groups, for example, although one of the most pervasive functionalities on energetic molecules, have been underutilized in crystal engineering due to their shallow potential energy well for hydrogen bonding interactions.[24,25] This results in unpredictable interaction directionalities that are heavily influenced by crystal packing.[24-26] In addition to these considerations, energetics often display dramatic differences in solubilities. This can make cocrystallization challenging because large differences in solubility between components generally leads to the recrystallization of the least soluble component.

Identifying cocrystals requires a combination of both spectroscopic and structural characterization methods, of which IR and Raman spectroscopies and XRD are most commonly employed. Although it is possible to identify cocrystals using one of these methods alone, samples must be prepared and data collected with precision and careful attention paid to the likely possibility of forming single-component polymorphs and/or solvates. Without confirmed sample identity and homogeneity, thermal characterization or sensitivity testing cannot be relied upon as a basis for claiming a novel cocrystal.[27]

2.2.1 Crystal Morphology

The morphology of a crystal can be defined as the macroscopic three-dimensional geometry, or habit, adopted by a crystal and arises, primarily, from the spacing between points on the corresponding Bravais lattice. For well over a century, analysis of crystal morphology has been employed as a technique by which to identify materials as diverse as minerals and pharmaceuticals. The law of constancy of interfacial angles states that the angular relations between faces of a crystal remain constant despite elongation or truncation of various crystal faces arising from growth conditions.[28-31] For this reason, the interfacial angles on a crystal can be measured and directly compared to a prediction of the morphology (using the Bravais-Friedel-Donnay-Harker approach, for example)[32] from known crystal structures to discern single component polymorphs and multicomponent cocrystals.[28-30] Optical or electron microscopy can be used to visualize changes in morphology to provide evidence of changes in unit cell parameters. However, complications arise in identifying single-component polymorphs by morphology when produced from multicomponent crystallizations. In these cases, physical mixtures of phase-pure components or solvates may be misidentified as novel cocrystalline materials.

In 2011 an energetic-energetic cocrystal between HMX and 1,3,5-triamino-2,4,6-trinitrobenzene (TATB) was claimed,[33] following computational predictions of the cocrystal structure.[23a,23c] In the original publication for the claimed TATB/HMX cocrystal,[33] SEM, Raman spectroscopy, terahertz time-domain spectroscopy (THz-TDS), and X-ray photoelectron spectroscopy (XPS) were employed for characterization. Raman spectroscopy, THz-TDS and XPS indicated the presence of HMX and TATB, although the SEM image suggested that the sample was heterogeneous. Multiple morphologies and irregular secondary growth adhered to the surface of well-formed crystals are visible upon further analysis of the SEM image (Figure 2.2). The interfacial angles, 1 through 6, of the well-formed crystals were measured from the SEM image of the reported cocrystal (Figure 2.2) and compared against the BFDH morphology predictions for the pure components. The interfacial angles of the well-formed crystals in the SEM image were found to match those of β-HMX (see Figure 2.2). Although the material bound to the surface of the β-HMX crystals is too irregular in morphology to measure the interfacial angles, from the Raman, THz-TDS, and XPS spectra it can be assumed that this material is TATB or TATB-containing. Minor shifting in the Raman signal of the claimed cocrystal can possibly be attributed to HMX polymorphism or solvate formation although further characterization is necessary to confirm the outcome of the crystallization.

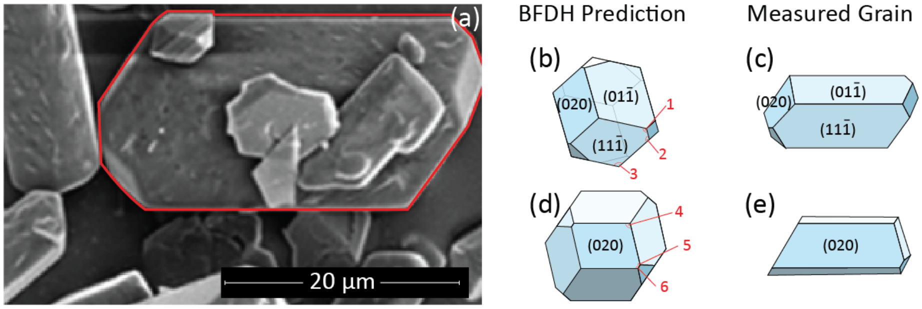

Figure 2.2. SEM Image and BFDH Morphology Prediction of β-HMX

(a) SEM image of reported HMX/TATB cocrystal adapted from Shen *et al.*[33]; (b) BFDH calculation result for β-HMX morphology showing the (11-1) face and highlighting the three measured angles (1, 2, 3); (c) reconstruction of imaged grain from SEM for measurement of the (11-1) face; (d) BFDH calculation result for β-HMX morphology showing the (020) face and highlighting the three measured angles (4, 5, 6); (e) reconstruction of imaged grain for measurement of the (020) face.

In order to identify the origin of the observed shift in Raman scattering in HMX/TATB, the crystallization protocol[33] was repeated (see Experimental Methods Section). The sample was dispersed onto a steel slide to separate individual crystal grains for Raman spectroscopy. A map (Figure 2.3) was generated by comparing spectra taken over a region of the dispersed crystallites against standard spectra of the pure components. The chemical heterogeneity illustrated by the Raman map demonstrates that the sample is a physical mixture of TATB and γ-HMX.

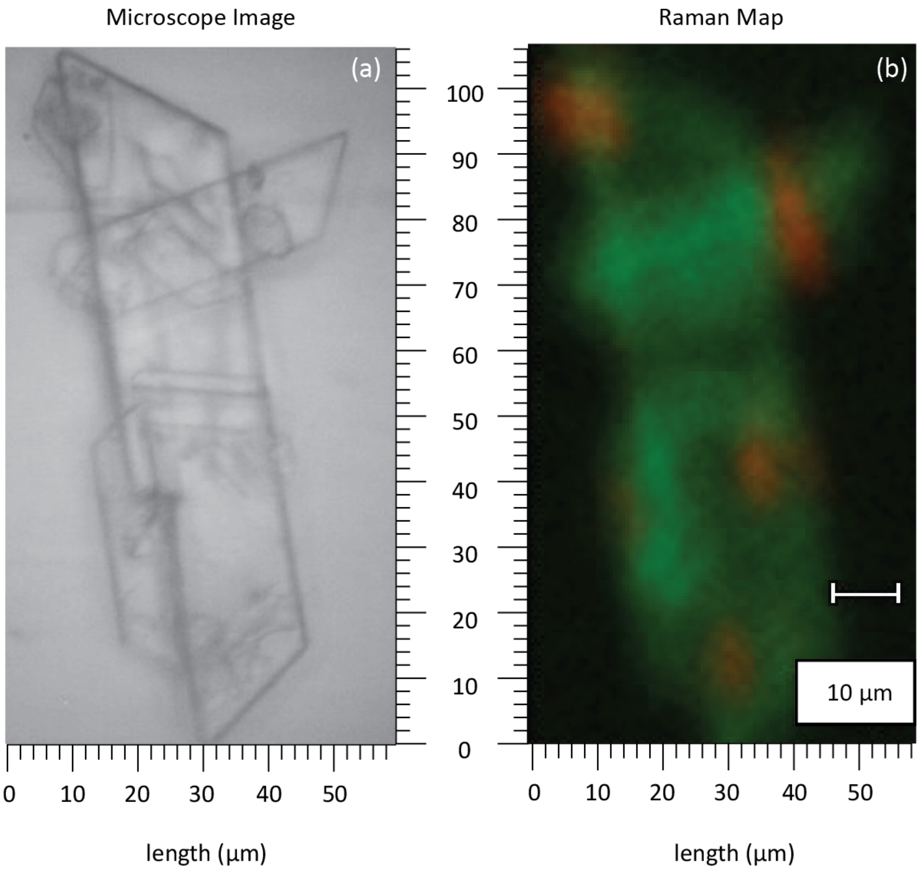

Figure 2.3. Raman Map of Crystallized HMX/TATB Material

(a) Optical microscope image and (b) Raman map of the material crystallized from the replicated HMX/TATB procedure with false color coding based on Direct Classical Least Squares 1st derivative fitting to standard spectra. γ-HMX is shown in green and TATB in red.

Crystallization of γ-HMX is not unexpected considering the preparation involves precipitating the material in water, conditions under which HMX readily converts to the hydrate. The γ-HMX phase was identified by comparing the powder XRD pattern of the HMX control against the patterns of all other known forms of HMX (Figure 2.4). Additionally, γ-HMX gives rise to shifting in the Raman signal relative to β-HMX, explaining the origin of the Raman shifts noted in the original publication.[33]

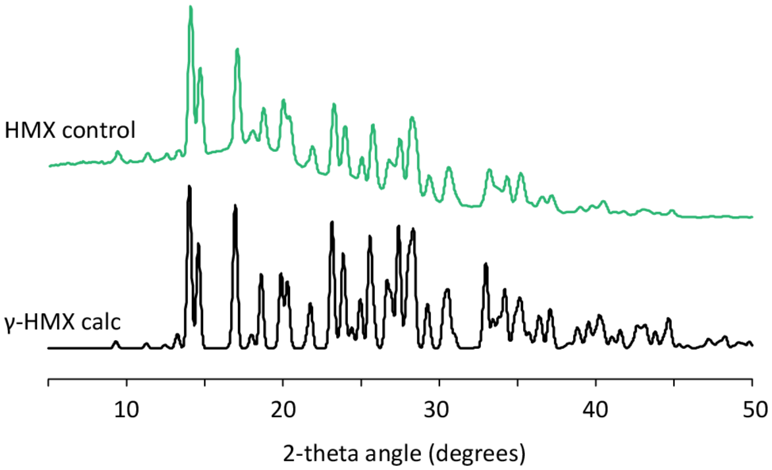

Figure 2.4. PXRD of Simulated and Control HMX

PXRD pattern of HMX control experiment from dimethylsulfoxide (DMSO)/water in comparison to that simulated from the SCXRD structure.

2.2.2 Infrared and Raman Spectroscopies

IR and Raman spectroscopies are well-established methods by which to identify phases present in a sample. Polymorphs and cocrystals typically display replicable shifting in the position of one or more vibrational bands, which signifies the presence of different intermolecular interactions relative to reference material. The cocrystal vibrational spectrum should be recognizable as a combination of both single-component spectra typically with slight shifting in peak position; extreme shifts often indicate salt formation or decomposition of the starting components.

The use of IR and Raman microscopes has improved the applicability of these techniques by enabling measurement on single crystals, which are, at least in principle, chemically homogenous. Ambiguous results or misinterpretation can occur much more frequently when measuring bulk material, where multiple phases can be present. An additional challenge, and one that is particularly problematic for energetic materials, is the propensity to form solvates or recrystallize in a different polymorph of one or both intended coformers as this would cause peak shifting in the resultant vibrational spectrum that could be misinterpreted as cocrystal formation. For this reason, IR and Raman microscopies should be considered methods by which to screen for the presence of cocrystalline material but should be followed up with powder and/or SCXRD to confirm that the material is structurally new relative to the known polymorphs and solvates of the starting materials.

In 2014, three materials containing 2,6-diamino-3,5-dinitropyrazine-1-oxide (LLM-105) cocrystallized with CL-20, 1,3,5-trinitro-*s*-triazine (RDX), and HMX were claimed and IR spectra were used to conclude that cocrystals were formed (Figure 2.5).[34] These materials were produced by dissolving the starting materials in DMSO at 90 °C, cooling the solutions to room temperature, and adding ethanol as an antisolvent.[34] In the case of LLM-105 and CL-20, crystallization was attempted in the absence and presence of trifluoroacetic acid in DMSO.[34] In all three attempted cocrystallizations, the precipitate was filtered and dried.

The IR spectrum of the material produced from LLM-105 and RDX (Figure 2.5a) resembles RDX predominantly, although weak peaks in the amine (3200-3500 cm^{-1}) and C=C (1600-1700 cm^{-1}) regions may be attributed to LLM-105. LLM-105 N-H bands (Figure 2.5b) show minor peak shifting between the reference (3225 cm^{-1} and 3431 cm^{-1}) and claimed cocrystal spectra (3229 cm^{-1} and 3433 cm^{-1}). More dramatic peak shifting in this region would be expected if the pattern of amine-nitro hydrogen bonding were disrupted to form new intermolecular interactions between LLM-105 and RDX. The remaining peaks below a 95% transmission threshold in the claimed cocrystal spectrum show overlap with the RDX reference within one wavenumber shifts with two exceptions: a sharp peak at 1567.8 cm^{-1} and a broad peak at 1650.9 cm^{-1} (Figure 2.5c). The 1567.8 cm^{-1} vibrational band shows a 2 cm^{-1} shift relative to the reference RDX spectrum (1569.9 cm^{-1}). Spectra of physical mixtures can exhibit minor peak shifting if two vibrations are close enough in energy that the peaks cannot be resolved. LLM-105 has a vibrational band at 1563.2 cm^{-1}, which when combined with reference RDX spectrum would appear as if the RDX peak were shifted to lower energy in the resulting spectrum if these two peaks were not resolved. The nearest reference peaks to the 1650.9 cm^{-1} band are the 1632.3 and 1610.9 cm^{-1} C=C vibrations in LLM-105. However, the likelihood of forming solvates or incomplete sample drying should also be considered. DMSO has a vibrational mode at 1659 cm^{-1} that may account for this peak and also displays intensity that could result in the shifts observed in the N-H stretching region discussed above.

To resolve these ambiguities, the cocrystallization protocols for the LLM-105/RDX and LLM-105/HMX samples were repeated and the resultant material analyzed by PXRD (Figure 2.6a,b) and Raman spectroscopy (Figure 2.6c,d). During reproduction of the protocol, it was found that LLM-105 precipitates rapidly upon the addition of ethanol, while RDX remains dissolved. However, this does not explain the presence of RDX in the IR spectrum from the original cocrystal report. Repeating the crystallization protocol and allowing the sample to crystallize over a two-week period results in physical mixtures of LLM-105 and RDX as evidenced by PXRD (see Figure 2.6a) and Raman spectroscopic analysis (see Figure 2.6c).

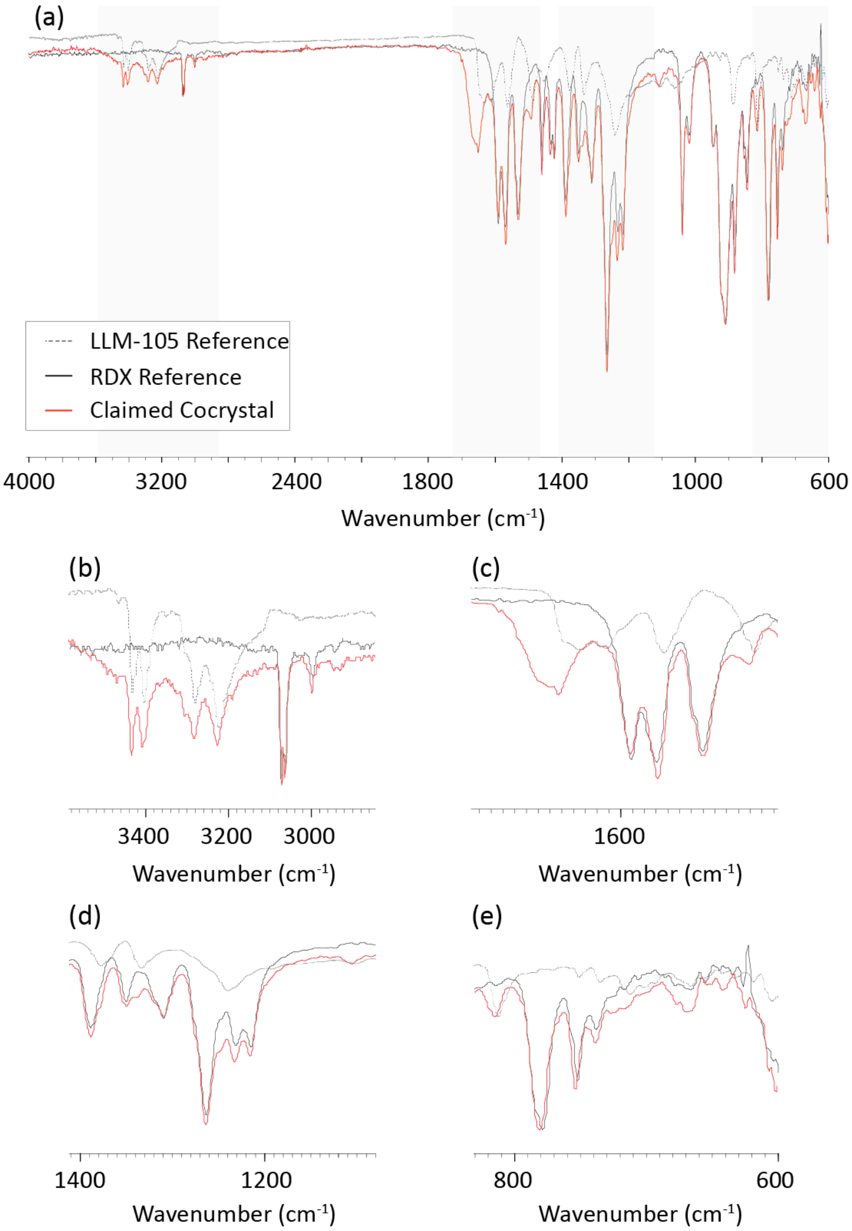

Figure 2.5. IR Spectra Adapted from Zhang and Zhao[34]

(a) LLM-105, RDX, and the claimed LLM-105/RDX cocrystal; (b) the 2800-3600 cm^{-1}, (c) 1400-1800 cm^{-1}, (d) 1100-1400 cm^{-1}, and (e) 600-800 cm^{-1} regions of the LLM-105, RDX, and claimed cocrystal spectra.

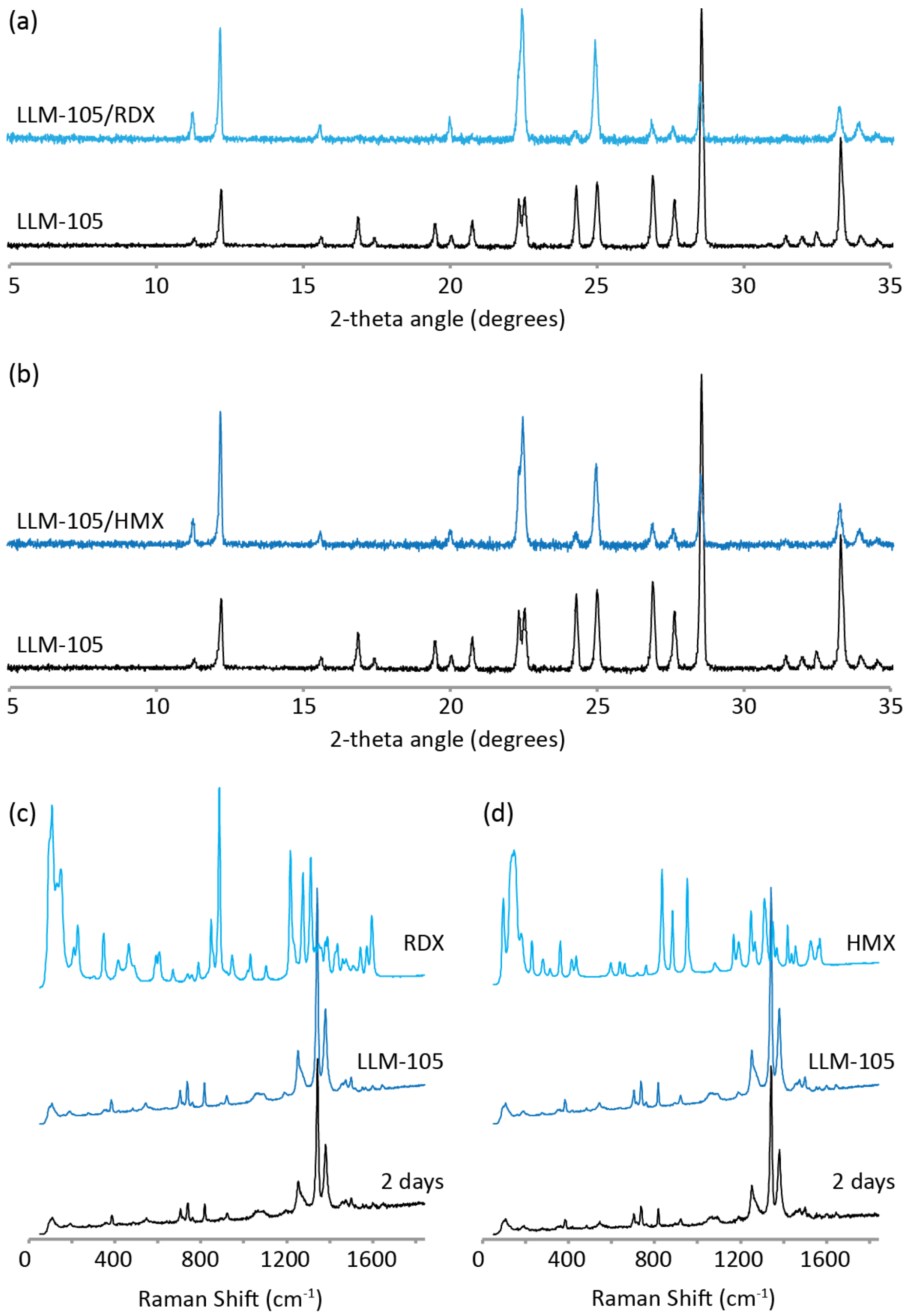

Figure 2.6. Characterization of LLM-105/RDX and LLM-105/HMX Material

PXRD patterns of (a) LLM-105/RDX and (b) LLM-105/HMX material and Raman spectra of (c) LLM-105/RDX and (d) LLM-105/HMX material produced from replicated crystallization protocols reported in Zhang and Zhao[34].

Similar conclusions were drawn for the LLM-105/HMX material, which are consistent with an optical microscope image of resultant LLM-105 and HMX material given in the original publication[34] (Figure 2.7a) that highlighted both the irregularity in crystal morphology and the presence of particulates adhered to the surface of the crystals, indicating that the result of crystallization is possibly phase impure. This hypothesis was investigated further by analyzing the LLM-105/HMX material produced from DMSO/ethanol by Raman spectroscopy (Figure 2.7b). The results from this experiment confirm that the material is heterogeneous and the colorless coarse-grain particles are HMX, while the yellow fine-grain particles are LLM-105. These data suggest that the DMSO/ethanol crystallization protocol forms physical mixtures of the two components, which further supports DMSO as the origin of the 1650.9 cm^{-1} peak in the original report.

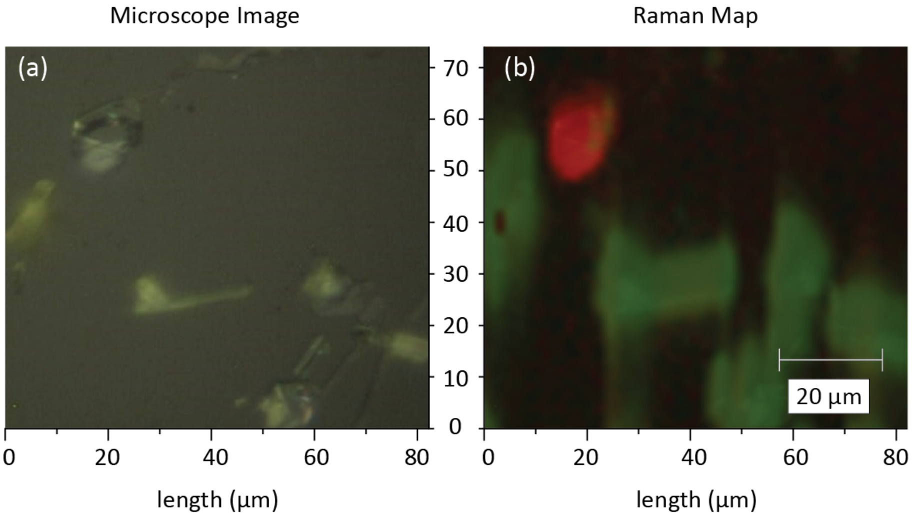

Figure 2.7. Raman Map of Crystallized LLM-105/HMX Material

(a) Optical microscope image of LLM-105/HMX material presented in Zhang and Zhao[34] and (b) Raman map of the material crystallized from the replicated LLM-105/HMX procedure with false color coding based on DCLS 1st derivative fitting to standard spectra. HMX is shown in red and LLM-105 in green.

The claimed cocrystallization of LLM-105 with CL-20 in the absence of trifluoroacetic acid gives rise to a spectrum identical to that of LLM-105 (see Figure 2.8a), indicating that the product of this crystallization is recrystallized LLM-105. This result is in accord with the findings of Zhang and Zhao[34] and likely occurs because CL-20 is soluble in the antisolvent, ethanol, and likely remained solubilized. The spectrum obtained from the LLM-105/CL-20 crystallization performed in the presence of trifluoroacetic acid (see Figure 2.8b) is missing key N-H stretches that would signify the presence of the amine groups on LLM-105. Additionally, signature LLM-105 peaks between 1450 and 1490 cm^{-1} are completely absent. The remainder of the peaks can be assigned to CL-20 with shifts between 0 and ~10 cm^{-1} relative to the standard, consistent with polymorph or solvate formation.

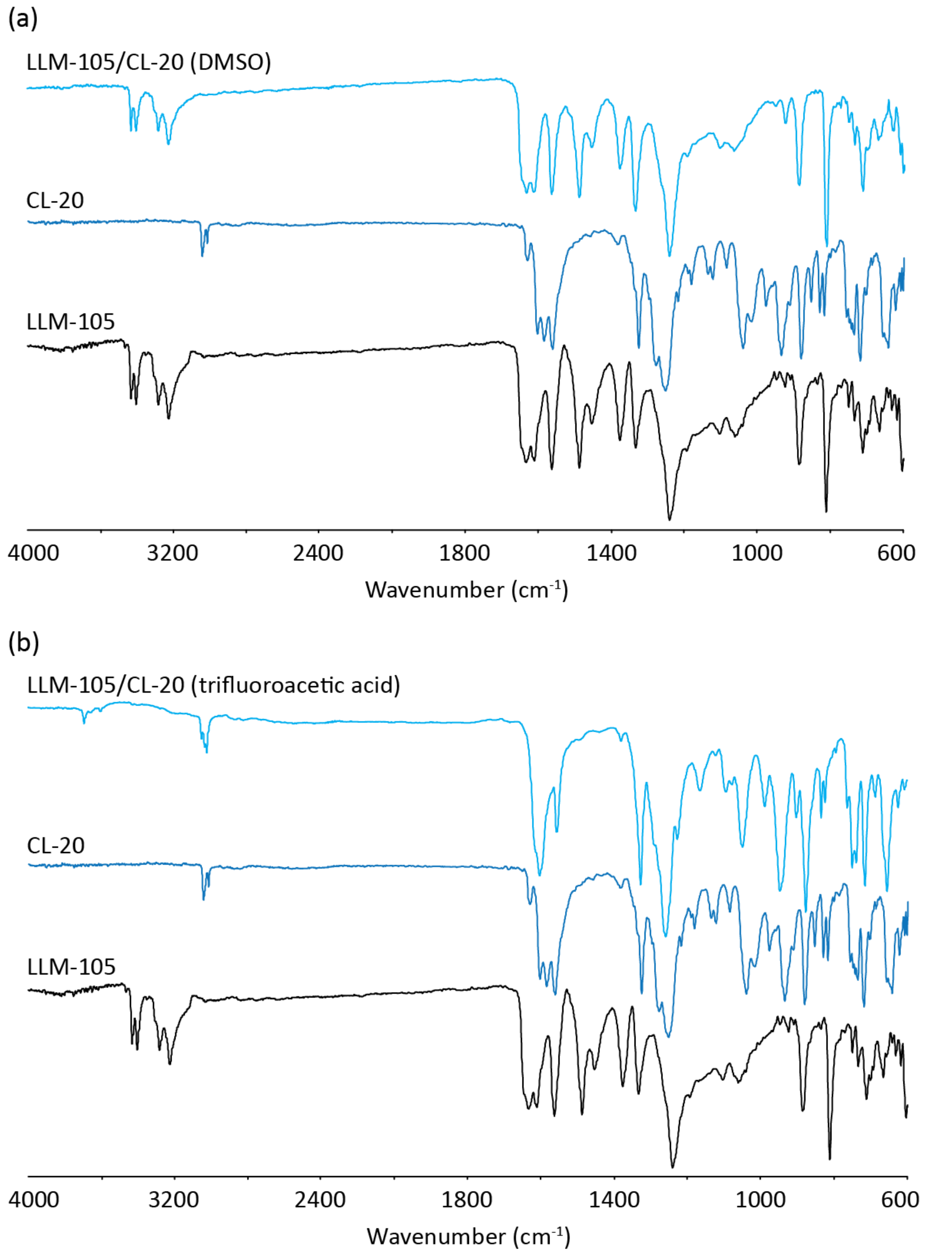

Figure 2.8. Infrared Spectra of LLM-105/CL-20

LLM-105/CL-20 material produced from DMSO (a) and trifluoroacetic acid (b) from Zhang and Zhao[34].

2.2.3 Powder X-Ray Diffraction

Powder XRD (PXRD) is one of the most common and reliable diagnostic methods by which to identify new crystalline forms or cocrystals of energetic compounds. For energetic materials that display low impact sensitivies, pure-phase samples can be ground and sieved to yield PXRD patterns with reproducible sample intensities directly relatable to the structure factors of the unit cell. However, because sample preparation is often limited by impact sensitivity (grinding is typically avoided), changes in crystal morphology, without changes in the unit cell parameters, can cause the diffractogram to differ notably in the relative peak intensities of the measured reflections. For this reason, the interpretation of relative peak intensities is unreliable and cocrystal patterns should always be compared to PXRD patterns calculated from the single-crystal structures of known polymorphs or solvates of the single-component phases. Calculated patterns include low intensity peaks that may not be observed in experimentally measured standard PXRD patterns and, conversely, low intensity peaks in the computed patterns may be more prominent in the experimental patterns due to preferential enhancement by preferred orientation. Pawley pattern decomposition can be used in cases where visual comparison against calculated patterns is inconclusive to quantitatively fit diffractograms displaying preferred orientation and overlapping peaks against the known standards.

In 1976, a cocrystal was patented between HMX and ammonium perchlorate (AP), though no structural characterization was included.[35] The PXRD data for this material was first reported in 2013 along with SEM images of the solid.[36] By analyzing the SEM image of the cocrystal, it becomes apparent that the imaged crystal grains resemble β-HMX as well as starting AP material (see Figure 2.9).

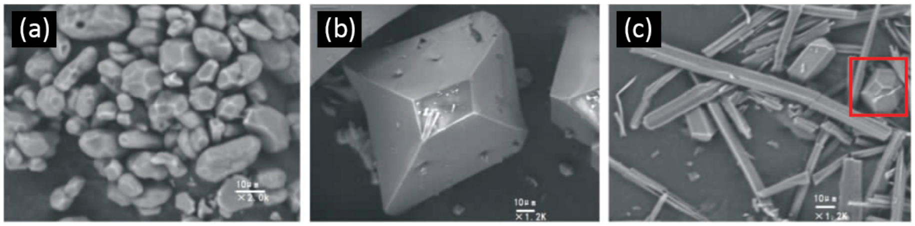

Figure 2.9. SEM Image of HMX/AP Material Adapted from Chen *et al.*[36]

In analyzing the PXRD data (Figure 2.10) the same conclusion can be drawn; the major peaks present in the cocrystal pattern can be assigned to the HMX and AP single-component powder patterns. Reflections at 16.4° and 36.5° are not present in either the reference AP or HMX patterns collected by the researchers but are accounted for in the powder pattern predicted from the β-HMX crystal structure and these reflections have been indexed as arising from the (100) and (140) Miller planes, respectively. From the morphological variation shown by SEM between the reference HMX and the high-aspect ratio material produced from the HMX/AP cocrystallization, a difference in relative peak intensity, and even dramatic loss in intensity for peaks, is expected due to a change in preferred orientation.

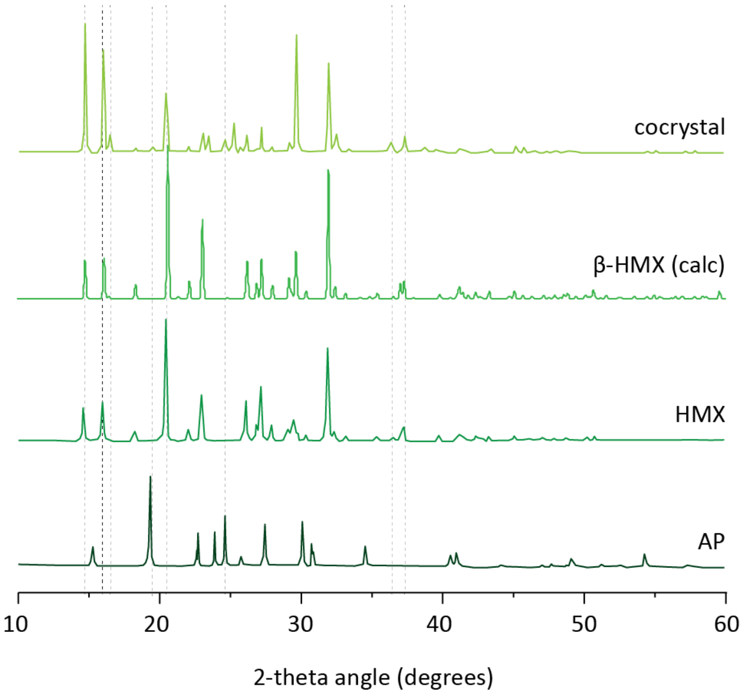

Figure 2.10. PXRD Analysis of HMX/AP Material

PXRD patterns of the claimed HMX/AP cocrystal and single-component standards adapted from Chen *et al.*[36] and calculated β-HMX from refcode OCHTET01. Vertical dashed lines are included to indicate alignment of peaks between stacked patterns.

A CL-20 and TATB cocrystal was claimed in 2015.[37] This material was prepared by dissolving both components in DMSO and precipitating the material by using water as an antisolvent. Five reflections (14.9°, 22.6°, 27.9°, 30.2°, and 39.9°) were cited as unique in spite of the fact that these peaks are present at low intensities in α-CL-20, a hydrated phase (Figure 2.11a), suggesting that the two starting components are present as physical mixtures. Major diffraction peaks in the claimed cocrystal sample also line up in peak position with those of α-CL-20 and the IR spectrum of the claimed cocrystal shows a broad O-H band between 3200 and 3600 cm^{-1} (see Figure 2.11b), providing further support for the presence of α-CL-20. Although IR peak shifting was noted, it is apparent from the IR spectrum that TATB bands are absent from the claimed cocrystal IR spectrum. We were unable to investigate the HMX/AP and CL-20/TATB materials experimentally because insufficient procedural detail was provided in the original publications.

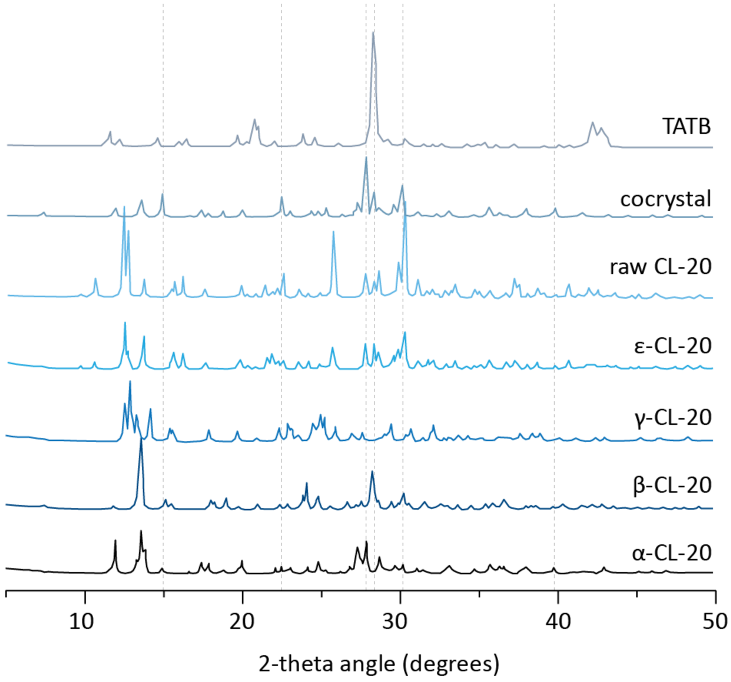

Figure 2.11. PXRD Analysis of CL-20/TATB Material

(a) Claimed CL-20/TATB cocrystal and single-component standards adapted from Xu *et al.*[37] Vertical dashed lines are included to indicate alignment of peaks between stacked patterns. (b) Infrared spectra of the claimed CL-20/TATB cocrystal and pure component standards adapted from Xu *et al*[37].

2.3 Conclusion

The cocrystallization of two energetic compounds is challenging to achieve and, in the absence of crystallographic data, presents significant characterization challenges. It is now well understood that cocrystallization will fail much more often than it will succeed and so the burden to provide clear and convincing evidence differentiating cocrystal formation from physical mixtures of polymorphs and/or solvates of the starting components is correspondingly high. The reliability and appropriate methodology for morphological, IR and Raman spectroscopic, and PXRD analyses have been discussed within the context of six physical mixtures originally published as cocrystals: HMX/TATB, RDX/LLM-105, HMX/LLM-105, CL-20/LLM-105, HMX/AP, and CL-20/TATB. Three of these samples, HMX/TATB, RDX/LLM-105, HMX/LLM-105, have been reproduced and additional characterization data supports the claims that these materials are physical mixtures. Rigorous analysis is pertinent, specifically, in the field of energetic materials development as sample heterogeneity can result in unreliable sample thermal and impact sensitivities leading to potential safety as well as performance issues.

2.4 Experimental Methods

Data were reinterpreted directly from scanning electron microscopy (SEM) images, vibrational spectra, and patterns presented in publications. Morphologies of crystals for comparison against published images were predicted from crystal structures (refcodes: OCHTET, OCHTET01, and DEDBUJ) obtained from the Cambridge Crystallographic Data Centre (CCDC) using the

Bravais-Friedel-Donnay-Harker (BFDH) method[28-30] available in the full version of CCDC Mercury 3.6 for Windows. The predicted morphology was oriented in Mercury to match crystals present in the SEM images and interfacial angles were measured from SEM images and the predicted morphologies using Adobe Illustrator CS5.1.

2.4.1 Crystallizations

HMX/TATB: Crystallization was adapted from Shen *et al.*[33] HMX (1.513 x 10^{-2} mmol, 4.48 mg) and TATB (1.782 x 10^{-3} mmol, 0.46 mg) were dissolved in 4.2 mL DMSO and heated to 45 °C to dissolve. DI water (4.2 mL) was added dropwise to the solution of TATB and HMX and stirred for 3 hours as the solution returned to room temperature. The sample was vacuum filtered and washed five times with DI water.

HMX/LLM-105: Crystallization was adapted from Zhang and Zhao.[34] HMX (2.249 x 10^{-2} mmol, 6.66 mg) and LLM-105 (2.277 x 10^{-2} mmol, 4.92 mg) were dissolved in 0.24 mL DMSO at 90 °C for three hours with stirring. Ethanol (1 mL) was added dropwise and yellow precipitate formed over two days. The precipitate was vacuum filtered.

RDX/LLM-105: Crystallization was adapted from Zhang and Zhao.[34] RDX (2.296 x 10^{-2} mmol, 5.10 mg) and LLM-105 (2.295 x 10^{-2} mmol, 4.96 mg) were dissolved in 0.16 mL DMSO at 90 °C for three hours with stirring. Ethanol (1 mL) was added drop-wise and yellow precipitate formed over two days. The precipitate was vacuum filtered.

2.4.2 Raman Spectroscopy

Raman spectra and maps were collected using a Renishaw inVia Raman Microscope equipped with a Leica microscope, 785 and 532 nm lasers, 1200 lines/mm (785 nm) and 1800 lines/mm (532 nm) gratings, 65 µm slit size, and a CCD area detector. Spectra were collected in static mode centered around 1000 cm^{-1} and 3200 cm^{-1} and analyzed using the WiRE 4.2 software package (Renishaw) for DCLS (Direct Classical Least Squares) mapping. Calibration was performed using a silicon standard.

2.4.3 Powder X-ray Diffraction

Powder patterns of γ-HMX standards were collected on a Rigaku R-Axis Spider diffractometer using Cu-Kα radiation (λ = 1.54187 Å) and operating at 40 kV and 44 mA. Samples were mounted on a CryoLoopTM and images were collected for 3 minutes with rotation of the sample about the ϕ-axis at 10°/sec, oscillating ω between 80° and 140° at 1°/sec with χ fixed at 45°. The images were integrated from 2 to 50° with a 0.02° step size using AreaMax 2.0 software (Rigaku). The data were processed using Jade 8 XRD Pattern Processing, Identification & Quantification analysis software (Materials Data, Inc.). The powder patterns were compared respective simulated powder patterns from single crystal XRD structures available from the Cambridge Crystallographic Data Centre and were found to be in good agreement with the predicted patterns. Powder patterns were collected on LLM-105 attempted cocrystallization materials on a Panalytical Empyrean using Cu-Kα radiation (λ = 1.54187 Å) and operating at 45 kV and 40 mA. The instrument is equipped with a Bragg-Brentano HD X-ray optic and an X'Celerator Scientific detector operating in continuous 1D scanning mode. Samples were prepared by pressing them onto a glass slide fitted into a sample holder to minimize height error.

The patterns were collected by scanning 2θ from 2 to 50° with a 0.02° step size and a step speed of 0.125 seconds. Background scattering was subtracted using a glass blank.

2.5 References

1. Klapötke, T. M., *Chemistry of High-Energy Materials*. 2nd ed.; De Gruyter: Berlin, 2012.
2. Williams, R. S., Safety of Explosives, Propellants, and Pyrotechnics. In NASA, Ed. Washington, DC, 2011.
3. Bond, A. D., What is a co-crystal? *CrystEngComm* **2007,** *9*, 833-834.
4. Stahly, G. P., A survey of cocrystals reported prior to 2000. *Cryst. Growth Des.* **2009,** *9*, 4212-4229.
5. Bolton, O.; Matzger, A. J., Improved stability and smart-material functionality realized in an energetic cocrystal. *Angew. Chem. Int. Ed.* **2011,** *50*, 8960-8963.
6. Millar, D. I. A.; Maynard-Casely, H. E.; Allan, D. R.; Cumming, A. S.; Lennie, A. R.; Mackay, A. J.; Oswald, I. D. H.; Tang, C. c.; Pulham, C. R., Crystal engineering of energetic materials: Co-crystals of Cl-20. *CrystEngComm* **2012,** *14*, 3742-3749.
7. Bolton, O.; Simke, L. R.; Pagoria, P. F.; Matzger, A. J., High Power Explosive with Good Sensitivity: A 2:1 Cocrystal of Cl-20:HMX. *Cryst. Growth Des.* **2012,** *12*, 4311-4314.
8. Zhang, H.; Guo, C.; Wang, X.; Xu, J.; He, X.; Liu, Y.; Liu, X.; Huang, H.; Sun, J., Five Energetic Cocrystals of BTF by Intermolecular Hydrogen Bond and π-Stacking Interactions. *Cryst. Growth Des.* **2013,** *13*, 679-687.
9. Yang, Z.; Li, H.; Zhou, X.; Zhang, C.; Huang, H.; Li, J.; Nie, F., Characterization and Properties of a Novel Energetic-Energetic Cocrystal Explosive Composed of HNIW and BTF. *Cryst. Growth Des.* **2012,** *12*, 5155-5158.
10. Landenberger, K. B.; Bolton, O.; Matzger, A. J., Two Isostructural Explosive Cocrystals with Significantly Different Thermodynamic Stabilities. *Angew. Chem. Int. Ed.* **2013,** *52*, 6468-6471.
11. Yang, Z.; Wang, Y.; Zhou, J.; Li, H.; Huang, H.; Nie, F., Preparation and Performance of a BTF/DNB Cocrystal Explosive. *Propellants, Explos. Pyrotech.* **2014,** *39*, 9-13.
12. Wang, Y.; Yang, Z.; Li, H.; Zhou, Z.; Zhang, Q.; Wang, J.; Liu, Y., A Novel Cocrystal Explosive of HNIW with Good Comprehensive Properties. *Propellants, Explos. Pyrotech.* **2014,** *39*, 590-596.
13. Wu, J.-T.; Zhang, J.-G.; Li, T.; Li, Z.-M.; Zhang, T.-L., A novel cocrystal explosive NTO/TZTN with good comprehensive properties. *RSC Adv.* **2015,** *5*, 28354-28359.
14. Bennion, J. C.; McBain, A.; Son, S. F.; Matzger, A. J., Design and Synthesis of a Series of Nitrogen-Rich Energetic Cocrystals of 5,5'-Dinitro-2*H*2*H*'-3,3'-bi-1,2,4-triazole (DNBT). *Cryst. Growth Des.* **2015,** *15*, 2545-2549.
15. Bennion, J. C.; Vogt, L.; Tuckerman, M. E.; Matzger, A. J., Isostructural Cocrystals of 1,3,5-Trinitrobenzene Assembled by Halogen Bonding. *Cryst. Growth Des.* **2016,** *16*, 4688-4693.
16. Zhang, J.; Shreeve, J. M., Time for pairing: cocrystals as advanced energetic materials. *CrystEngComm* **2016,** *18*, 6124-6133.
17. Bernstein, J., *Polymorphism in Molecular Crystals*. Oxford University Press: Oxford, U.K., 2002.

18. Cady, H. H.; Smith, L. C., Studies on the polymorphs of HMX. In Laboratory, L. A. S., Ed. Los Alamos, NM, 1962.
19. Landenberger, K. B.; Matzger, A. J., Cocrystal Engineering of a Prototype Energetic Material: Supramolecular Chemistry of 2,4,6-Trinitrotoluene. *Cryst. Growth Des.* **2010,** *10*, 5341-5347.
20. Main, P.; Cobbledick, R. E.; Small, R. W. H., Structure of the Fourth Form of 1,3,5,7-Tetranitro-1,3,5,7-tetraazacyclooctane (γ-HMX), $2C_4H_8N_8O_8.0.5H_2O$. *Acta Crystallogr.* **1985,** *C41*, 1351-1354.
21. Nielsen, A. T.; Chafin, A. P.; Christian, S. L.; Moore, D. W.; Nadler, M. P.; Nissan, R. A.; Vanderah, D. J.; Gilardi, R. D.; George, C. F.; Flippen-Anderson, J. L., Synthesis of Polyazapolycylic Caged Nitramines. *Tetrahedron* **1998,** *54*, 11793-11812.
22. Bennion, J. C.; Chowdhury, N.; Kampf, J. W.; Matzger, A. J., Hydrogen Peroxide Solvates of 2,4,6,8,10,12-Hexanitro-2,4,6,8,10,12-hexaazaisowurtzitane. *Angew. Chem. Int. Ed.* **2016,** *55*, 13118-13121.
23. Although there has been increased effort directed towards computationally modeling crystal structures and associated physical properties of novel energetic-energetic corystals, discussion of computational methods fall outside of the scope of this paper. See ref 17 (a) Nedelko, V. V.; Chukanov, N. V.; Raevskii, A. V.; Korsounskii, B. L.; Larikova, T. S.; Kolesova, O. I. Propellants, Explos., Pyrotech. **2000**, *25*, 255. (b) Wei, C.; Duan, X.; Liu, C.; Liu, Y.; Li, J. Act Chimica Sinica **2009**, *67*, 2822. (c) Wei, C.; Huang, H.; Duan, X.; Pei, C. Propellants, Explos., Pyrotech. **2011**, *36*, 416. (d) Lin, H.; Zhu, S.-G.; Zhang, L.; Peng, X.-H.; Chen, P.-Y.; Li, H.-Z. Int. J. Quantum Chem. **2013**, *113*, 1591. (e) Lin, H.; Zhu, S.-G.; Li, H.-Z.; Peng, X.-H. J. Phys. Org. Chem. **2013**, *26*, 898. (f) Li, Y.-X.; Chen, S.-S.; Ren, F.-D. J. Mol. Model. **2015**, *21*, 1. (g) Kim, S.-H.; Ko, Y.-M.; Shin, C.-H.; Kim, S.-J. J. Korean Chem. Soc. **2016**, *60*, 9. (h) Ding, X.; Gou, R.-J.; Ren, F.-D.; Liu, F.; Zhang, S.-H.; Gao, H.-F. Int. J. Quantum Chem. **2016**, *116*, 88.
24. Panunto, T. W.; Urbanczyk-Lipowska, Z.; Johnson, R.; Etter, M. C., Hydrogen-bond formation in nitroanilines: the first step in designing acentric materials. *J. Am. Chem. Soc.* **1987,** *109*, 7786-7797.
25. Etter, M. C.; Huang, K. S.; Frankenbach, G. M.; Adsmond, D. A., Materials for Nonlinear Optics Chemical Perspectives Control of Symmetry and Asymmetry in Hydrogen-Bonded Nitroaniline Materials. *ACS Symp. Ser.* **1991,** *455*, 446-456.
26. Robinson, J. M. A.; Philp, D.; Harris, K. D. M.; Kariuki, B. M., Weak interactions in crystal engineering—understanding the recognition properties of the nitro group. *New J. Chem.* **2000,** *24*, 799-806.
27. Even morphological changes, crystallite size, and recrystallization conditions can lead to changes in such properties for a single energetic component. See (a) Redner, R.; Patel, K. R.; Chung, M.; Martin, D. Production and Characterization of Nano RDX; U.S. Army, RDECOM-ARDEC Picatinny, NJ, 2006. (b) Pivkina, A.; Ulyanova, P.; Frolov, Y.; Zavyalov, S.; Schoonman, J. Propellants, Explos., Pyrotech. **2004**, *29*, 39. (c) Fathollahi, M.; Pourmortazavi, S. M.; Hosseini, S. G. J. Energ. Mater. **2007**, *26*, 52. (d) Fathollahi, M.; Mohammadi, B.; Mohammadi, J. Fuel **2013**, *104*, 95.
28. Bravais, A., Gauthier Villars: Paris, 1866.
29. Friedel, G., *Bull. Soc. Franc. Mineral.* **1907,** *30*, 326.
30. Donnay, J. D. H.; Harker, D. A., *Am. Mineral.* **1937,** *22*, 463.

31. Urbelis, J. H.; Swift, J. A., Solvent Effects on the Growth Morphology and Phase Purity of CL-20. *Cryst. Growth Des.* **2014,** *14*, 1642-1649.
32. Though the constancy of interfacial angles is a reliable principle, its application requires the faces to be visible. Different growth conditions can influence the propensity of certain faces to be expressed and more advanced morphology predictions may be required in such cases.
33. Shen, J.; Duan, X.; Luo, Q.; Zhou, Y.; Bao, Q.; Ma, Y.; Pei, C., Preparation and Characterization of a Novel Cocrystal Explosive. *Cryst. Growth Des.* **2011,** *11*, 1759-1765.
34. Zhang, S.; Zhao, H., Preparation and Characterization of LLM-105 Cocrystal Explosives. *Adv. Mater. Res.* **2014,** *900*, 251-255.
35. Levinthal, M. L. Propellant made with Cocrystal of Cyclotetramethylenetetranitramine and Ammonium Perchlorate. 1976, US4086110.
36. Chen, J.; Duan, X.; Pei, C., Preparation and characterization of HMX/AP co-crystal. *Chinese Journal of Energetic Materials* **2013,** *21*, 409-413.
37. Xu, H.; Duan, X.; Li, H.; Pei, C., A novel high-energetic and good-sensitive cocrystal composed of CL-20 and TATB by a rapid solvent/non-solvent method. *RSC Adv.* **2015,** *5*, 95764-95770.

Chapter 3 : Detonation Performance of Ten Forms of DNBT[*]

3.1 Introduction

The properties of an explosive arise primarily from chemical structure of the energetic material.[1, 2] That said, the solid form adopted by an energetic also influences practical aspects of detonation performance. Crystal polymorphism is a pervasive phenomenon exhibited by high explosives and is considered the subtlest example of this effect, whereby the density of the different polymorphs directly influences detonation velocity and leads to unpredictable changes in sensitivity.[1, 3-9] Multicomponent crystals, solvates and cocrystals, can show much larger perturbations from the performance of the parent compounds because parameters, such as oxygen balance (OB), can be altered as well.[2, 10, 11]

OB is a parameter that describes the weight percent of oxygen available to convert a material into neutral molecular species (e.g. CO_2, H_2O).[12] Despite efforts towards improving OB, the majority of energetic materials are characterized by a negative OB, signifying that there is a deficiency of oxidant relative to fuel content. Multicomponent crystallization necessarily leads to a weighted averaging of the OB values of the constituents based on the stoichiometry of the cocrystal or solvate. For example, the cocrystal formed in a 2:1 ratio between 2,4,6,8,10,12-hexanitro-2,4,6,8,10,12-hexaazoisowurtzitane (CL-20, OB = -10.95%) and octahydro-1,3,5,7-tetranitro-1,3,5,7-tetrazocine (HMX, OB = -21.61%) has an oxygen balance of -13.65%.[10] Similarly α-CL-20 and γ-HMX are hydrated forms of the parent compounds with OB values of -10.84% and -21.29%, respectively. However, hydrate formation results in an unproductive

---

[*] Published: Wiscons, R. A.; Bellas, M. K.; Bennion, J. C.; Matzger, A. J. *Cryst. Growth Des.* **2018**, *18*, 7701-7707

improvement in the OB because the waters of hydration (OB = 0%) are unreactive upon decomposition, diminishing heat release while often lowering crystallographic density.[11, 13-19] For this reason, energetic hydrates are determinedly avoided, although hydrate formation is becoming a more persistent challenge with the shift towards heterocyclic and high-nitrogen energetic compounds.

Herein we explore the ways in which polymorphism and solvate formation perturb the performance of the energetic azole 5,5'-dinitro-2*H*,2*H*'-3,3'-bi-1,2,4-triazole (DNBT, see Figure 3.1). Azoles are desirable energetic compounds because they generally have improved OB values relative to traditional aromatic energetics (i.e. 2,4,6-trinitrotoluene and 2,4,6-triamino-1,3,5-trinitrobenzene, see Figure 3.1), show lower sensitivies to heat and impact, and produce materials with high crystallographic densities.[17, 20] We have selected DNBT because it shows a high a detonation velocity and low impact sensitivity but has not yet seen significant application, in part, because it suffers from hydrate formation under traditional crystallization conditions.[17, 20] We take advantage of the diverse hydrates formed by DNBT to provide a quantitative study of the effect of hydration on energetic performance. Finally, we demonstrate that this undesirable feature can be leveraged to produce DNBT/H_2O_2 solvates with improved OB values relative to other known DNBT multicomponent solids as well as DNBT itself.

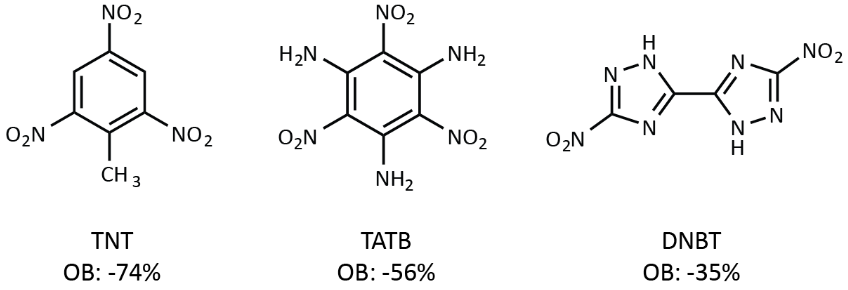

Figure 3.1. Oxygen Balances of Common Energetics and DNBT

The molecular structures and oxygen balances (OB) of the aromatic energetic compounds 2,4,6-trinitrotoluene (TNT), 2,4,6-triamino-1,3,5-trinitrobenzene (TATB), and DNBT.

3.2 Results and Discussion

Although the propensity for DNBT to form hydrates has previously been noted,[17,19] the scope and impact on performance have not been investigated. To derive hydration-dependent trends in performance, six unreported and two previously published crystal structures of DNBT are compared. The six unreported structures include one anhydrous DNBT form (β) and five stoichiometrically unique hydrates (two-thirds, mono-, sesqui-, di- (II), and tetra-), while the two reported crystal structures include an anhydrous DNBT form (α)[17] and a dihydrate (I)[13]. The space groups and symmetries for these crystal structures are provided in Table 3.1, including the tetrahydrate for which rapid desolvation precluded full data collection.

Table 3.1. Crystallographic Data for Anhydrous and Hydrated DNBT Structures

	α	β	two-thirds	monohydrate	sesquihydrate	dihydrate I	dihydrate II	tetrahydrate
Stoichiometry	-	-	2 : 3	1 : 1	1.5 : 1	2 : 1	2 : 1	4 : 1
Space Group	$P2_1/n$	$P2_1$	$P\text{-}42_1c$	$C2/c$	$P\text{-}1$	$P2_1/c$	$P2_1/n$	$Pna2_1$
a (Å)	5.0831(12)	11.6952(5)	12.84290(10)	12.0055(5)	8.7374(2)	3.9712(3)	6.7074(3)	11.4677(17)
b (Å)	6.3618(5)	6.4293(2)	12.84290(10)	13.3653(6)	9.1113(3)	8.6361(5)	5.1699(3)	8.6027(18)
c (Å)	12.3568(17)	12.1541(5)	16.4050(2)	11.9400(5)	12.7299(3)	14.7208(8)	15.3820(11)	12.896(3)
α (°)	90	90	90	90	103.188(2)	90	90	90
β (°)	94.294(19)	112.437(5)	90	100.343(4)	95.203(2)	90	92.146(6)	90
γ (°)	90	90	90	90	95.096(2)	90	90	90
Volume (Å^3)	398.468	844.709	2705.84	1884.73	976.335	504.86	533.021	1272.25
ρ_{calc} (g cm^{-3})	1.885	1.778	1.754	1.721	1.722	1.725	1.633	1.556

3.2.1 The Hydrates of DNBT

The DNBT hydrates were crystallized using a screening method in which the relative ratios between water and a solution of DNBT dissolved in dry acetonitrile were varied in a 96-well plate according to the concentrations given in Table 3.2a and the 96-well plate format given in Table 3.2b.

Table 3.2. DNBT Hydrate Screening Method

(a) Concentration of DNBT (x, y) or water (l, m, n, o, p, q) in dry acetonitrile used as stock solutions for high-throughput hydrate screening using 96-well plates.

Solution Identifier	Solution
x	0.04 M DNBT
y	0.04 M DNBT
l	55 M H_2O
m	4.1 M H_2O
n	0.4 M H_2O
o	0.6 M H_2O
p	0.4 M H_2O
q	0.3 M H_2O

(b) Layout of the 96-well plate in which the stock solutions were combined in various ratios. Values given in μL.

	1	2	3	4	5	6	7	8	9	10	11	12
A	6x,2l	6x,2m	6x,2n	6x,2o	6x,2p	6x,2q	6y,2l	6y,2m	6y,2n	6y,2o	6y,2p	6y,2q
B	6x,3l	6x,3m	6x,3n	6x,3o	6x,3p	6x,3q	6y,3l	6y,3m	6y,3n	6y,3o	6y,3p	6y,3q
C	6x,4l	6x,4m	6x,4n	6x,4o	6x,4p	6x,4q	6y,4l	6y,4m	6y,4n	6y,4o	6y,4p	6y,4q
D	4x,4l	4x,4m	4x,4n	4x,4o	4x,4p	4x,4q	4y,4l	4y,4m	4y,4n	4y,4o	4y,4p	4y,4q
E	4x,6l	4x,6m	4x,6n	4x,6o	4x,6p	4x,6q	4y,6l	4y,6m	4y,6n	4y,6o	4y,6p	4y,6q
F	3x,6l	3x,6m	3x,6n	3x,6o	3x,6p	3x,6q	3y,6l	3y,6m	3y,6n	3y,6o	3y,6p	3y,6q
G	2x,6l	2x,6m	2x,6n	2x,6o	2x,6p	2x,6q	2y,6l	2y,6m	2y,6n	2y,6o	2y,6p	2y,6q
H	8x	8l	8m	8n	8o	8p	8q	8y				

Well “A-1” can be understood to contain 6 μL of solution “x” and 2 μL of solution “l,” for example.

Crystals were grown by evaporation of the mixed solvent and the crystalline forms were initially differentiated using Raman spectroscopy (see Figure 3.2), followed by structure determination by single-crystal X-ray diffraction (SCXRD).

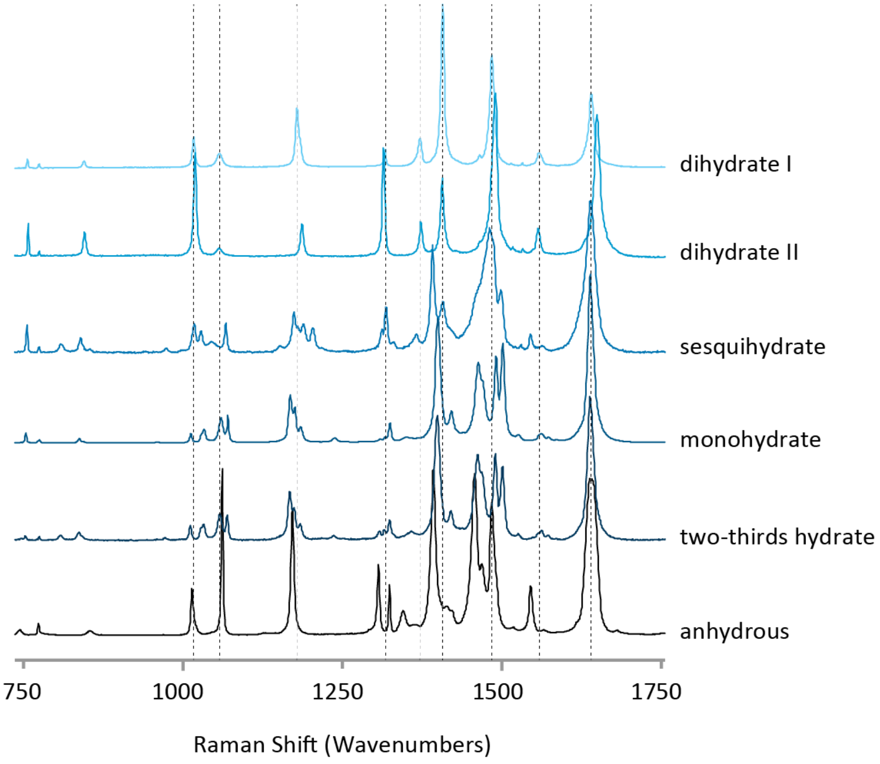

Figure 3.2. Raman Spectra of the Anhydrous and Hydrated Forms of DNBT

Crystallization using the high-throughput screening method produced primarily DNBT dihydrate I, secondarily DNBT sesquihydrate, and small quantities of the anhydrous (α and β), two-thirds, dihydrate II, and tetrahydrate forms of DNBT. DNBT monohydrate was produced via evaporation from isopropanol. The preferential formation of DNBT dihydrate I was further investigated by slurrying anhydrous DNBT in water, producing DNBT dihydrate I selectively. Similarly, the water concentration regime (0.2 – 2.0 M in acetonitrile) was investigated through a series of slurry conversion experiments, which only selectively produced DNBT dihydrate I from anhydrous DNBT when 2.0 M water in acetonitrile was used. Below this concentration of water, a physical mixture of DNBT sesquihydrate and DNBT dihydrate I was observed.

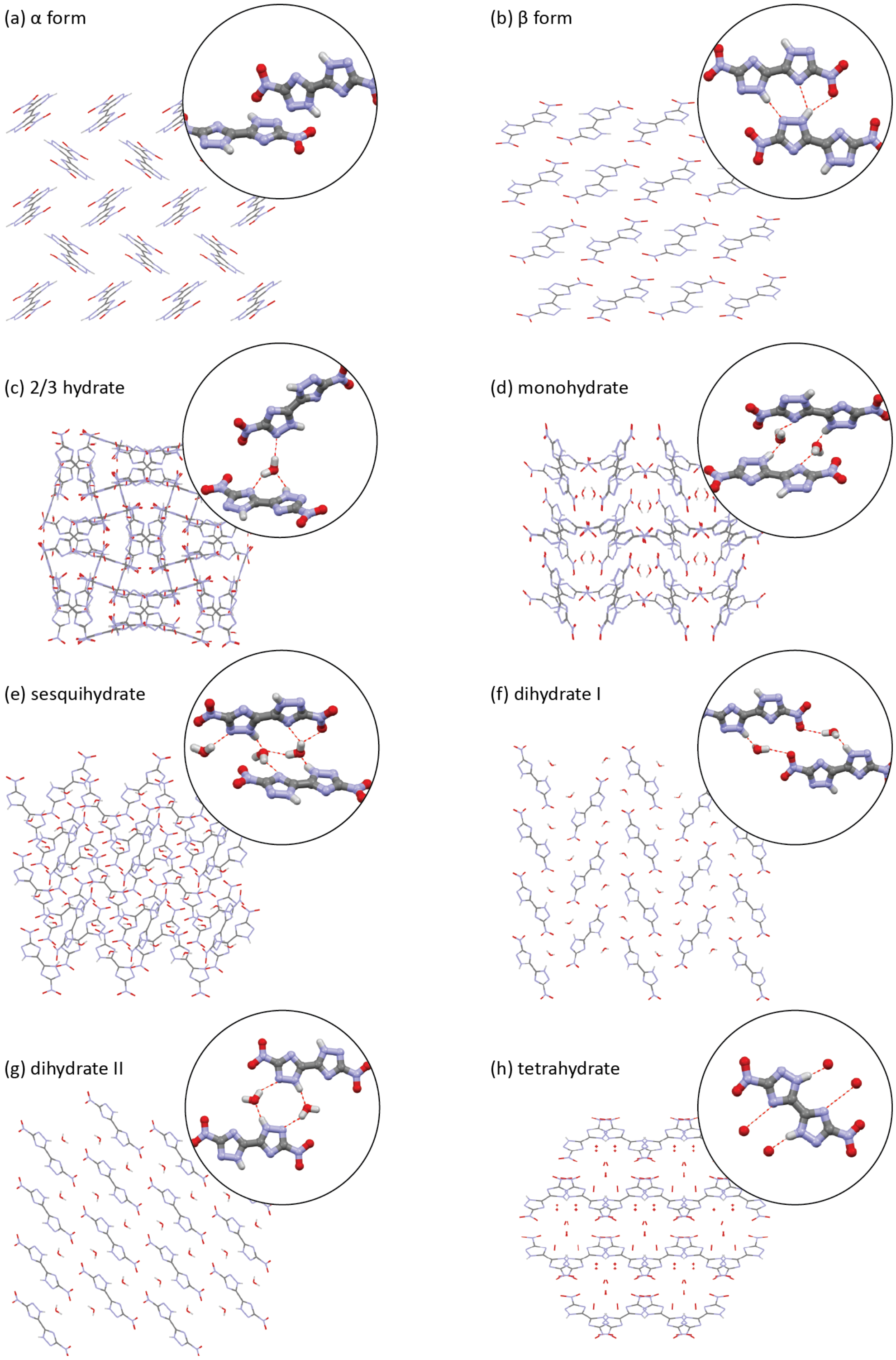

Figure 3.3. Crystal Structures of Anhydrous and Hydrated DNBT Forms

Crystal structures and hydrogen bonding interaction patterns (red dashed lines) of the anhydrous DNBT polymorphs (a, b) and DNBT hydrates (c-h). Carbon atoms are shown in gray, nitrogen atoms in blue, oxygen atoms in red, and hydrogen atoms in white. Hydrogen atoms have been omitted from the water molecules in DNBT tetrahydrate due to poor data quality.

In order to understand the diversity of DNBT hydrate crystal structures, electrostatic potential maps were calculated for isolated molecules of DNBT and water. DNBT shows one electrostatic maximum ($V_{s,max}$), which represents a region of electron deficiency, and five unique electrostatic minima ($V_{s,min}$), which represent regions that are electron rich (Figure 3.4). The DNBT electrostatic potential map highlights the deficiency of hydrogen bond donors in DNBT relative to hydrogen bond acceptors. This deficiency can be used to explain the propensity for DNBT to form hydrates, which introduce additional hydrogen bonds to electron-rich sites on DNBT. When compared to the local $V_{s,min}$ calculated for DNBT, the oxygen atom on water shows a stronger hydrogen bond acceptor potential, outcompeting all five sites on DNBT. DNBT, however, is predicted to outcompete water as a hydrogen bond donor based on the magnitude of the calculated $V_{s,max}$. Using this reasoning, it was predicted that DNBT N-H → (O)H_2 would be present more frequently than alternative hydrogen bonding interactions (e.g. water-water hydrogen bonds) in DNBT hydrate structures.

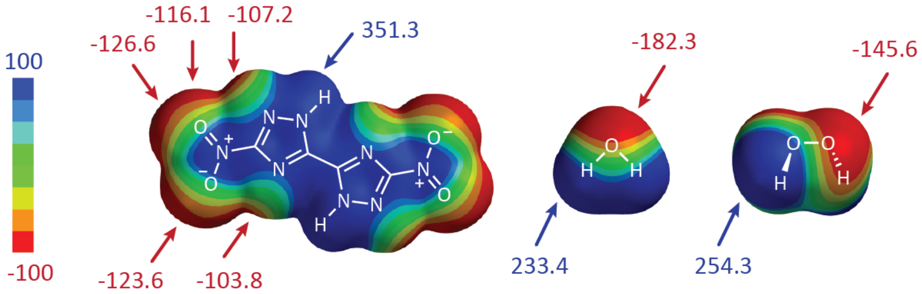

Figure 3.4. Electrostatic Potential Maps of DNBT, Water, and Hydrogen Peroxide

$V_{s,min}$ (red) and $V_{s,max}$ (blue) were calculated using B3LYP/6-311G** and labeled in kJ mol^{-1}.

This prediction was tested by comparing the type and number of hydrogen bonding interactions in the asymmetric units of the six DNBT hydrate crystal structures (see Table 3.3). It was found that when hydration is low (e.g. the two-thirds hydrate), hydrogen bonds from DNBT are donated to water and no water-water hydrogen bonding interactions are observed. With increasing waters of hydration (e.g. the sesquihydrate), the hydrogen bonds donated by DNBT are predominantly accepted by water molecules and water-water interactions are observed.

Table 3.3. Type and Number of Hydrogen Bonding Interactions in DNBT Hydrates

The number of N-H and O-H hydrogen bonds donated to water in the asymmetric unit are given in the numerator, while the total number of hydrogen bond donors are given in the denominator.

	(DNBT) N-H → O (H_2O)	(H_2O) O-H → O (H_2O)
two-thirds hydrate	2/3	0/2
monohydrate	1/2	1/2
sesquihydrate	3/4	1/6
dihydrate I	1/1	0/2
dihydrate II	1/1	0/2
tetrahydrate	2/2	2/8

As shown in Table 3.3, the increase in favorable local DNBT N-H → (O)H_2 hydrogen bonding interactions correlate with solid forms showing lower crystallographic densities (e.g. the two-thirds hydrate, ρ = 1.754 g cm^{-3}, versus the tetrahydrate, ρ = 1.556 g cm^{-3}). Crystallographic densities of the DNBT hydrates are plotted in Figure 3.5 as a function of hydration state. From this plot, a distinct trend is shown between increasing waters of hydration and lower crystallographic densities. Furthermore, this correlation suggests that crystallographic density shows very little dependence on crystal packing and instead more closely reflects the average of the densities of the constituents at the appropriate relative stoichiometries in the unit cell.

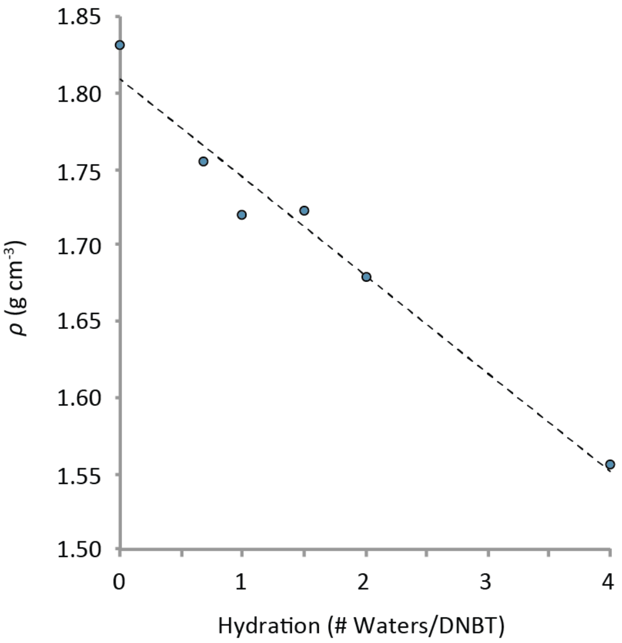

Figure 3.5. Correlation between Hydration State and Crystallographic Density

The detonation performance (velocity, pressure) of the DNBT hydrates were calculated using the heats of formation of the components (DNBT[17] and liquid water), at the appropriate stoichiometries, and room temperature crystallographic densities of the DNBT forms using Cheetah 7.0[21] (see Table 3.4 and Figure 3.6a-d). The specific impulses of DNBT and its hydrates were also calculated (Table 3.4 and Figure 3.6e,f) to investigate the effect of hydrate formation on propellant behavior. A decrease in detonation velocity, detonation pressure, and specific impulse is observed with increasing hydration state. This trend is consistent with expectations given that water dilutes the energy density of DNBT. The detonation velocity and detonation pressure show stronger correlations to crystallographic density ($R^2_V = 1.00$ and $R^2_P = 0.99$) than to hydration ($R^2_V = 0.81$ and $R^2_P = 0.85$). These correlations indicate that the primary way in which crystallographic hydrates suppress detonation performance parameters is by decreasing crystallographic density. In contrast, the specific impulse (Figure 3.6e,f) shows a stronger correlation to hydration ($R^2_I = 0.98$) than to crystallographic density ($R^2_I = 0.83$), suggesting that hydration dilutes propellant behavior by introducing molecules that contribute to the mass of the material without a concomitant increase in potential energy.

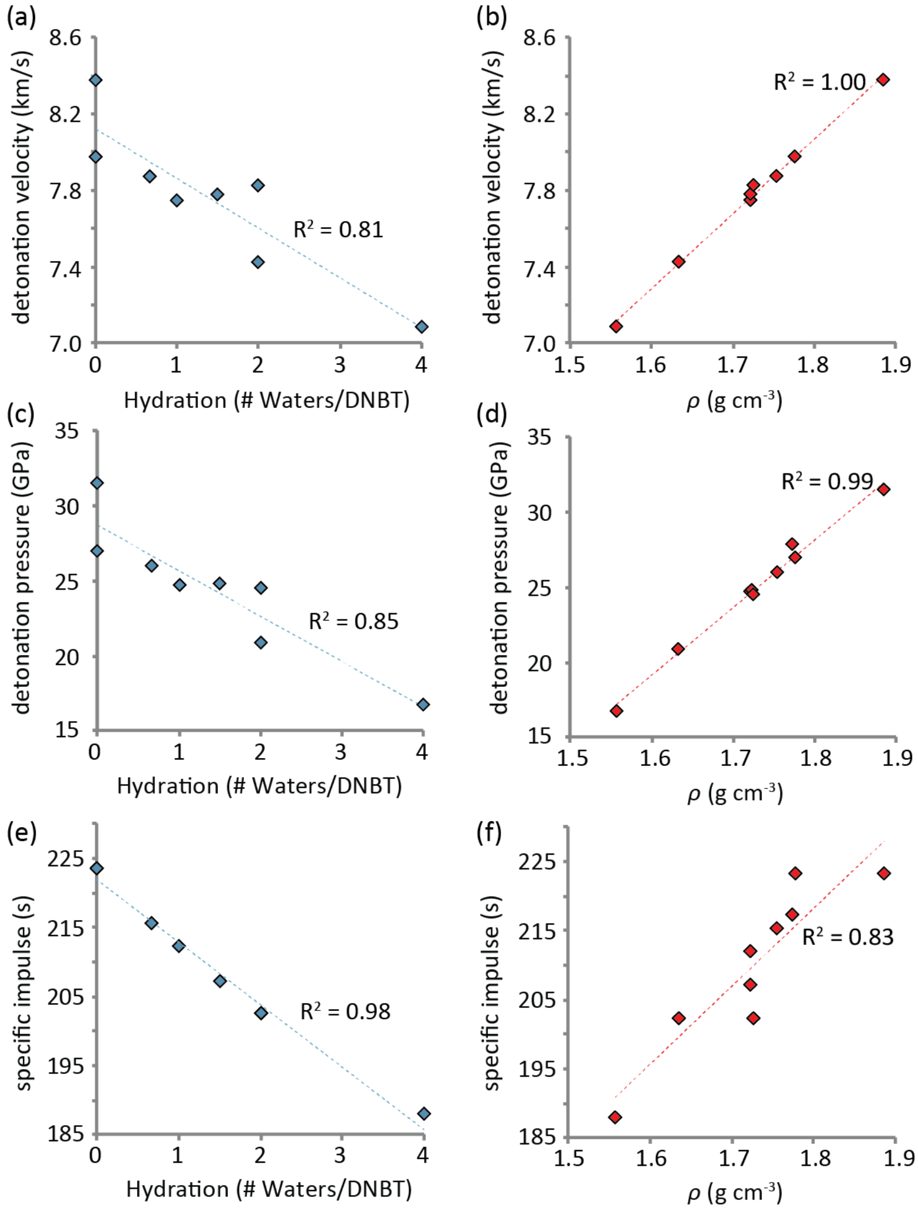

Figure 3.6. Density and Hydration-dependent Detonation Performance of DNBT

(a) Trends between detonation velocity and density and (b) detonation velocity and hydration state. (c) Trends between detonation pressure and density and (d) detonation pressure and hydration state. (e) Correlation between specific impulse and density and (f) specific impulse and hydration state.

Table 3.4. Table of Cheetah 7.0 Performance Values

	ρ_{calc} (g cm^{-3})	Detonation Velocity (km/s)	Detonation Pressure (GPa)	Specific Impulse (s)
α	1.885	8.376	31.43	223.47
β	1.778	7.973	26.94	223.47
Two-thirds hydrate	1.754	7.867	25.99	215.55
Monohydrate	1.721	7.743	24.66	212.55
Sesquihydrate	1.722	7.771	24.73	207.23
Dihydrate I	1.725	7.823	24.52	202.50
Dihydrate II	1.633	7.419	20.89	202.50
Tetrahydrate	1.556	7.086	16.74	187.93
H_2O_2 Solvate **1**	1.772	8.060	27.78	217.44

3.2.2 DNBT Hydrogen Peroxide Solvates

Given the propensity for DNBT to form hydrates, the possibility of forming hydrogen peroxide solvates with DNBT was explored as a route by which to improve the OB and to avoid the complex mixture of hydrate phases produced by DNBT. Recently, inclusion of solvent molecules with positive OB values, such as hydrogen peroxide (H_2O_2), into the crystal structures of energetic compounds to improve the overall OB of energetic materials has been demonstrated;[11] this approach serves much the same role of oxidizing counterions in energetic salts but is applicable to uncharged energetics. H_2O_2 is capable of forming strong hydrogen bonding networks, similar to water molecules, and therefore may produce crystals structurally related to energetic hydrates. In the case of α-CL-20, for example, water molecules trapped in pores of the crystal structure can be substituted with H_2O_2 to yield an isostructural solvate with an exceptional OB (-8.79%).[11] This strategy for improving OB may prove valuable with the rapidly expanding class of heterocyclic and high-nitrogen energetic compounds, although the generality of this approach has not yet been shown.

It was predicted that H_2O_2 could outcompete water to form the corresponding DNBT H_2O_2 solvate because the isolated electrostatic potential surfaces of H_2O_2 and water indicate that

H_2O_2 is a stronger hydrogen bond donor (larger $V_{s,max}$) and weaker hydrogen bond acceptor (smaller $|V_{s,min}|$) when compared to water (Figure 3.4). These findings are consistent with those of Chernyshov *et al.* who, based on interaction distances in the crystal structure of H_2O_2 dihydrate,[22] concluded that H_2O_2 is a stronger hydrogen bond donor than is water.[23]

Two H_2O_2 solvates of DNBT (**1** and **2**) were discovered by evaporation of H_2O_2 and acetonitrile. Solvate **1** was initially crystallized using ~98% H_2O_2 and was later shown to crystallize from a solution of acetonitrile and 50% v/v H_2O_2 (in water) as a physical mixture with solvate **2**. In contrast, solvate **2** is produced when lower concentrations of H_2O_2 (in water) are used. The two forms can be differentiated by their Raman spectra (see Figure 3.7), which show slight shifts in peak position/broadness between 1350-1675 cm^{-1} (see Figure 3.7a) that are assigned to differences in the symmetrical equivalence of nitro group torsion angles between the two forms (supported by SCXRD, see below). Unambiguous evidence for H_2O_2 incorporation in **1** and **2** is shown by the O-O stretch at 879 cm^{-1} and 880 cm^{-1}, respectively, differentiating the H_2O_2 solvates from the hydrates and anhydrous forms of DNBT (see Figure 3.7b). The closeness of the O-O Raman shift for **1** and **2** to that of neat H_2O_2 (879 cm^{-1})[11] suggests that the hydrogen bonding interactions between DNBT and H_2O_2 in the solvates are similar to those formed between molecules of neat H_2O_2. This observation contrasts that observed for CL-20/H_2O_2, in which the peaks corresponding to O-O stretching were shifted to lower frequencies in the solvates (866 cm^{-1} and 872 cm^{-1}) due to interaction with the nitro groups in CL-20.[11]

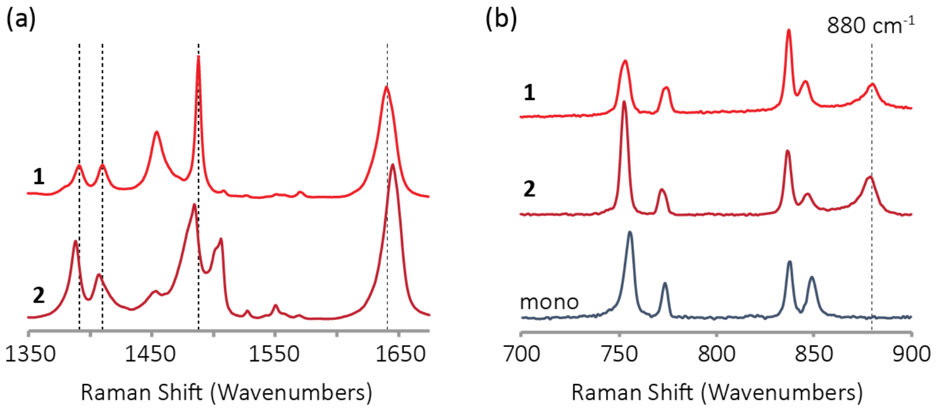

Figure 3.7. Raman Spectra of DNBT Hydrogen Peroxide solvates 1 and 2

(a) Nitro region of the Raman spectra differentiating solvates **1** and **2**; (b) O-O region of the Raman spectra of **1**, **2**, and DNBT monohydrate.

Solvate **1** was produced in high yield as the pure crystalline phase by cooling a solution of DNBT in ~98% H_2O_2 (to ensure no phase contamination from form **2**). The hydrogen peroxide content was quantified by reaction with triphenylphosphine to form triphenylphosphine oxide. From the integration ratio of the two ^{31}P NMR signals, the H_2O_2 content in solvate **1** was calculated as 0.996 ± 0.006 H_2O_2 : 2 DNBT. Results from Karl Fischer titration indicate that 0.057 water : 1 DNBT is incorporated into samples of solvate **1** prepared by the same method. Phase pure solvate **2** could not be produced in high enough quantities to verify the H_2O_2 and water contents experimentally, although this form refined to a 0.4 H_2O : 0.8 H_2O_2 : 2 DNBT ratio by SCXRD.

Solvate **1** crystallizes in the *P*-1 space group with one H_2O_2 and two DNBT molecules contained in the asymmetric unit, which is in agreement with the molar ratio determined by ^{31}P NMR. Having confirmed the relative stoichiometries between DNBT and H_2O_2 crystallographically, the OB value for the idealized DNBT H_2O_2 hemi-solvate was calculated at -29.6%, which is significantly improved relative to anhydrous DNBT, -35.4% (see Table 3.5).

Table 3.5. Table of Calculated Oxygen Balance (OB) Values

	Formula	Molecular Weight (g mol^{-1})	Oxygen Balance (%)
Anhydrous	$C_4H_2N_8O_4$	226.11	-35.38
Two-thirds Hydrate	$C_6H_5N_{12}O_7$	357.185	-33.60
Monohydrate	$C_4H_4N_8O_5$	244.13	-32.77
Sesquihydrate	$C_8H_{10}N_{16}O_{11}$	506.28	-31.60
Dihydrate	$C_4H_6N_8O_6$	262.15	-30.52
Tetrahydrate	$C_4H_{10}N_8O_4$	298.19	-26.83
H_2O_2 Solvate **1**	$C_4H_3N_8O_5$	243.115	-29.62

Using the crystallographic density for solvate **1** (ρ_{calc} 1.772 g cm^{-3}), the detonation velocity, detonation pressure, and specific impulse were calculated at 8.060 km/s, 27.78 GPa, and 217.4 s, respectively. These performance predictions suggest that solvate **1** outperforms all hydrate forms of DNBT. Solvate **1** is structurally related to DNBT monohydrate with one molecule of H_2O_2 replacing two adjacent water molecules (see Figure 3.8). Of the DNBT hydrate forms, the monohydrate shows the shortest O···O distance between adjacent water molecules, making it the most likely hydrate to show replacement of two molecules of water with one molecule of H_2O_2. Despite the monohydrate showing a short O···O distance, substitution causes solvate **1** and the monohydrate to solve into different space groups, making the substitution pseudoisomorphous.

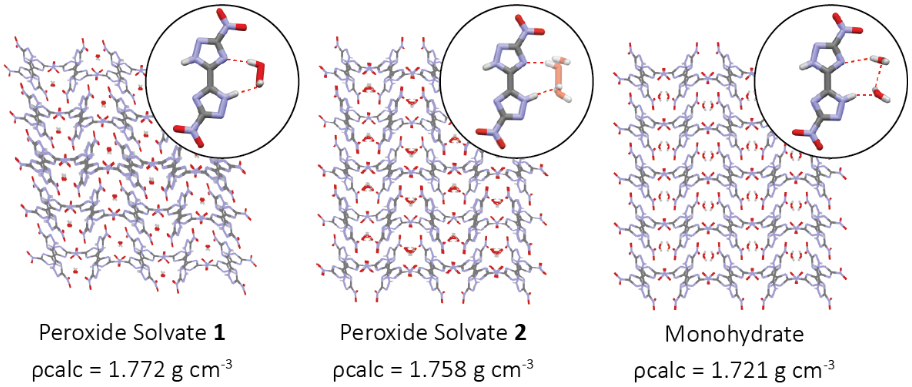

Figure 3.8. Crystal Structures of 1, 2, and DNBT Monohydrate

Crystal structures of **1**, **2**, and DNBT monohydrate highlighting the packing motif with insets focusing on the hydrogen bonding interactions between DNBT and H_2O_2 or water.

In solvate **1**, hydrogen bonds between molecules of H_2O_2 and the triazole rings of DNBT form a corrugated tape motif that extends parallel to the *c*-axis (see Figure 3.9). The tapes are segregated by chains of DNBT weakly bound through (O)NO_2 → (N)NO_2 stacking interactions that propagate along the *a*- and *b*-axes. The two chains are symmetry inequivalent due to differences in the nitro group torsion angle relative to the backbone of the DNBT molecule (22.0° for the chain along the *a*-axis and 11.2 – 28.9° for the chain showing disorder along the *b*-axis). The chains are further held in place by hydrogen bonds donated by triazole rings on DNBT molecules in the chains to triazole rings on DNBT molecules in the corrugated tapes.

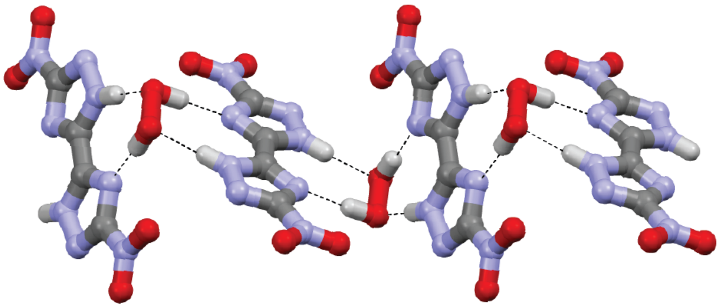

Figure 3.9. Hydrogen Bonding Interactions between DNBT and H_2O_2

Solvate **2** is isomorphous with DNBT monohydrate (see Figure 3.8), resulting in a site occupancy disorder between H_2O_2 and H_2O in the crystal structure. Solvate **2** crystallizes with fractional solvent and one DNBT per asymmetric unit and is nearly identical in structure to **1**, differing only by the two orthogonal chains of DNBT, which are symmetry equivalent in **2** (one unique nitro group torsion angle of 10.9°). This structural difference, in addition to a narrowing of the H-O-O-H torsion angle (as defined by the angles between the flanking DNBT molecules) from 79.3° in **1** to 87.9 - 92.1° in **2**, lengthens the hydrogen bonding interactions in **2** relative to solvate **1**, resulting in a slightly lower density for **2** (ρ_{calc} 1.758 g cm^{-3}) relative to solvate **1** (ρ_{calc} 1.772 g cm^{-3}).

The thermal sensitivity of **1** was characterized by differential scanning calorimetry (DSC). The thermal sensitivity of **1** was compared against bulk DNBT crystallized using the protocol of Fischer, Klapötke, and Stierstorfer,[24] which, in our hands, produced a physical mixture of DNBT dihydrate I and the 2/3 hydrate of DNBT (see Figure 3.10); this finding reaffirms the propensity of DNBT to crystallize as physical mixtures of lower-performance hydrates.

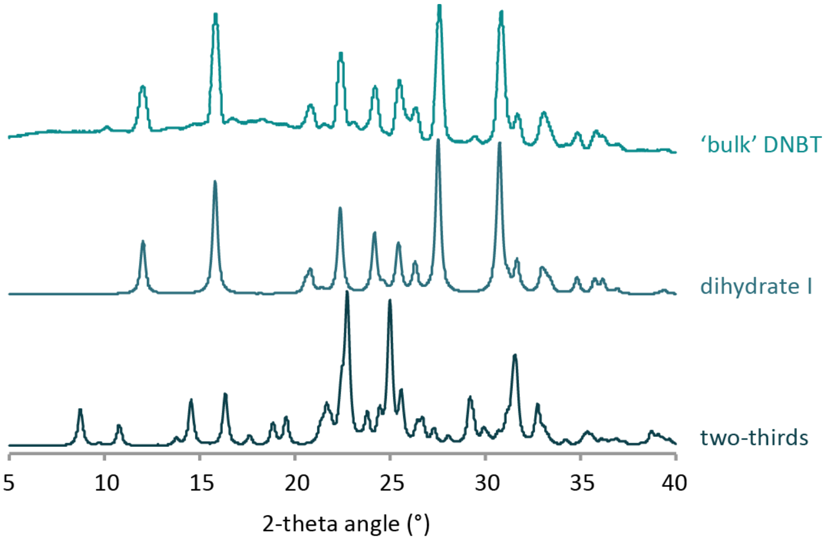

Figure 3.10. PXRD Analysis of 'Bulk' DNBT

Predicted powder X-ray diffraction patterns of calculated from the SCXRD structures of DNBT dihydrate I and DNBT two-thirds hydrate compared against the experiment pattern measured from 'bulk' DNBT crystallized following the Fischer, Klapötke, and Stierstorfer protocol.

The DSC trace of bulk DNBT shows a broad endotherm from 70 to 140 °C associated with dehydration of the various DNBT hydrates (Figure 3.11). This bulk DNBT material shows an exotherm at 247 °C attributable to thermal decomposition of DNBT. The DSC trace of solvate **1**

(Figure 3.11) shows an exotherm at 178 °C, attributed to thermal decomposition of H_2O_2.[25] The H_2O_2 decomposition event is followed by an additional exotherm at 263 °C, which is attributed to thermal decomposition of DNBT. These data suggest that dehydration of bulk DNBT and desolvation of **1** result in solid forms of DNBT with differing thermal sensitivities. In order to investigate this disparity, the monohydrate of DNBT, which is most similar in structure to solvate **1**, was selectively crystallized and characterized by DSC (Figure 3.11). The DSC trace of DNBT monohydrate also shows decreased thermal sensitivity of the dehydrated form (260 °C) relative to the bulk DNBT trace, suggesting that the increased thermal stability of desolvated **1** is not due to a reaction between DNBT and H_2O_2 but rather likely results from transformation to a more robust phase.

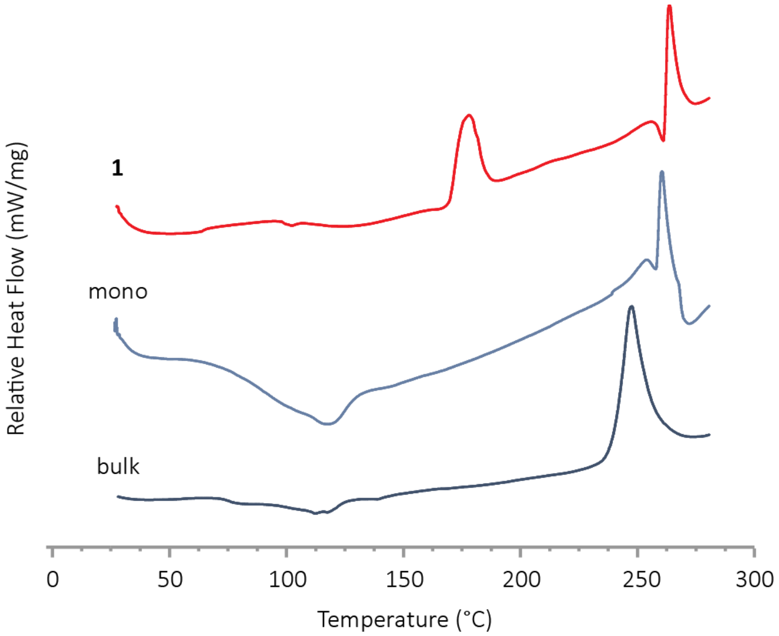

Figure 3.11. DSC Comparison between Solvate 1 and DNBT Hydrate(s)

Differential scanning calorimetry traces for ‘bulk’ DNBT, DNBT monohydrate, and DNBT solvate **1**.

3.3 Conclusion

DNBT produces a remarkable number of crystalline forms under a narrow range of crystallization conditions. The two anhydrous polymorphs and six hydrates enabled quantification of the extent to which water can erode detonation performance and specific impulse. Detonation velocity and detonation pressure are strongly correlated with crystallographic density, whereas specific impulse is strongly correlated with the hydration state. The solid form diversity expressed by DNBT has been leveraged to produce a H_2O_2 solvate, demonstrating the utility of this approach as a method to preclude hydrate formation by addressing the disparity between hydrogen bond donating and accepting groups in this system. Due to the increased hydrogen bond donor strength of H_2O_2 relative to water, this strategy of solid form control is predicted to be general for energetic compounds that readily form hydrates, such as the rapidly expanding class of heterocyclic and high-nitrogen energetics.

3.4 Experimental Methods

Caution: Although no unplanned detonations were encountered during this work, DNBT is a dangerous high explosive and hydrogen peroxide is a strong oxidizing agent. Proper safety practices and equipment were used to prevent an explosion due to friction, heat, static shock, impact, and flame. Be aware that the potential for severe injury exists if these materials are handled improperly.

5,5’-Dinitro-2H,2H’-3,3’-bi-1,2,4-triazole (DNBT) was received from Lawrence Livermore National Labs or synthesized according to Fischer *et al.*.[24] Hydrogen peroxide (98% w/w in water) was obtained from PeroxyChem LLC. Triphenylphosphine, 99% was obtained from

Acros Organics and recrystallized from methanol before use. Acetonitrile was obtained from Fisher Scientific, passed through an activated alumina column before use, and stored over 4Å molecular sieves.

3.4.1 Crystallization

Crystallization Screening Experiments using 96-well Plates

DNBT and water solutions in MeCN were made as described in Table 3.2a**.** These solutions were loaded into an Eppendorf epMotion 5070 automated liquid handling device, which dispensed the solutions into wells of a 96-well plate in the amounts specified in Table 3.2b. The solutions were then allowed to evaporate and the resultant material analyzed via optical microscopy, Raman spectroscopy, and X-ray diffraction techniques.

Water Activity Slurry Experiment

Solutions of water and MeCN were created with varying H_2O activity (1.60 – 11.3 M), accounting for the water in the MeCN as 0.3 mg/g via coulometric Karl Fisher titration. Anhydrous DNBT along with a 2.5 mm diameter glass bead was placed in each of ten 1 mL vials. To each vial was added 100 μL of the corresponding solvent mixture and the vials were sealed with screw caps and wrapped with Parafilm. The vials were placed on an orbital shaker set to 750 rpm and left for 14 days. The supernatant was removed by suction and the samples analyzed via PXRD immediately.

Crystallization of DNBT hydrates

A 4 mL vial was charged with 2.5 mg of DNBT dihydrate I. To this vial was added 500 µL of 2-propanol (11.5 mg/g H_2O content determined via coulometric Karl Fisher titration) and 6 µL H_2O. The vial was sealed and agitated on an orbital shaker, set to 110 rpm, for 48 h. The vial was then opened and the solvent allowed to evaporate under ambient. Raman spectroscopy revealed that this method produced a physical mixture of DNBT monohydrate, DNBT sesquihydrate, and DNBT dihydrate I. DNBT monohydrate produced by this method was used for crystal structure determination.

Crystallization of the DNBT-H_2O_2 Solvates

A 20 mL vial was charged with 26.80 mg anhydrous DNBT. The DNBT was subsequently dissolved in 1.1 mL dry acetonitrile with sonication. To this solution was added 300 µL hydrogen peroxide (98% w/w in H_2O). The vial was covered by a watch glass, allowing for evaporation, and left undisturbed for 48 h. Colorless block crystals of solvates **1** and **2** (differentiated by Raman spectroscopy). DNBT-H_2O_2 **1** was selectively crystallized via cooling crystallization of 26.06 mg (1.153×10^{-4} mol) anhydrous DNBT in 1.0 mL of 98% (w/w) H_2O_2. These crystal forms were subjected to crystal structure determination.

3.4.2 Single-Crystal X-Ray Structure Determination

Single-crystal X-ray diffraction data were collected using a Rigaku XtaLAB Synergy-S X-ray diffractometer configured in a kappa goniometer geometry. The diffractometer is equipped with a PhotonJet-S microfocus Cu source (λ = 1.54187 Å) set at a rough divergence of 9.5 and operated at 50 kV and 1 mA. X-ray intensities were measured at room temperature with the HyPix-6000HE detector placed 34.00 mm from the sample. The data were processed with

CrysAlisPro v38.46 (Rigaku Oxford Diffraction) and corrected for absorption. The structures were solved in OLEX2[26] using SHELXT[27] and refined using SHELXL[28]. All non-hydrogen atoms were refined anisotropically with hydrogen atoms placed in a combination of refined and idealized positions.

3.4.3 Powder X-Ray Diffraction

Powder X-ray diffraction data were collected using a Rigaku XtaLAB Synergy-S X-ray diffractometer configured in a kappa goniometer geometry. Data were collected in "Fast Phi Mode" at all positions with two-theta maximum set to 100 degrees and exposure times between 100 and 300 seconds. The diffractometer is equipped with a PhotonJet-S microfocus Cu source (λ = 1.54187 Å) set at rough divergences between 0.9 and 9.5 depending on sample type and operated at 50 kV and 1 mA. X-ray intensities were measured at room temperature with the HyPix-6000HE detector placed between 34.00 and 80.00 mm from the sample. The data were processed using a combination of Excel 2010 and Origin.

3.4.4 Raman Spectroscopy

Raman spectra were collected using a Renishaw inVia Raman Microscope equipped with a Leica microscope, a 633nm laser, 1800 lines/mm gratings, 50 μm slit size, and a CCD area detector. Spectra were collected in extended scan mode with a range of 3600 - 100 cm^{-1} and analyzed using the WiRE 3.4 software package (Renishaw). Calibration was performed using a silicon standard in static mode.

3.4.5 Karl Fischer Titration

The relative amounts of water in hydrogen peroxide solvate **1** samples, expressed as a percent (where 1 mg/g = 0.1%), were determined via coulometric Karl Fisher titration using a Mettler Toledo C20 Coulometric KF Titrator.

3.4.6 ^{31}P NMR Spectroscopy

^{31}P NMR measurements were carried out on Varian vnmrs 500 MHz spectrometer operating at room temperature, using 4 scans and a 25 second relaxation delay. A standard solution of triphenylphosphine (12.00 mg, 4.575 X 10^{-5} mol) in dry acetonitrile (5.00 mL) was prepared. Hydrogen peroxide solvate **1** (3.85 mg, 7.92 X 10^{-6} mol) was dissolved in 1.52 mL of the standard solution and allowed to shake for 30 minutes to react. The ratio of triphenylphosphine to triphenylphosphine oxide for each spectrum was calculated by integration of the peaks using MestReNova v12.0.0-20080, Mestrelab Research, 2017.

3.4.7 Differential Scanning Calorimetry

Differential scanning calorimetry (DSC) traces for each sample (~0.2 mg) were recorded on a TA Instruments Q10 DSC. All experiments were run in Tzero^{TM} hermetic aluminum DSC pans with a heating rate of either 5 °C/min or 2 °C/min, covering a temperature range of 31 °C to 400 °C. The instrument was calibrated using an indium standard. DSC traces were analyzed using TA Universal Analysis 2000, V 4.5A, build 4.5.0.5.

3.5 References

1. Klapötke, T. M., *Chemistry of High-Energy Materials*. 2 ed.; De Gruyter: 2012.
2. Kennedy, S. R.; Pulham, C. R., Co-crystallization of Energetic Materials. In *Co-crystals: Preparation, Characterization, and Applications*, Sinha, C. B. A. a. A. S., Ed. Royal Society of Chemistry: 2018; pp 231-266.
3. Bernstein, J., *Polymorphism in Molecular Crystals*. Oxford University Press: Clarendon, Oxford, 2002.
4. Miller, G. R.; Garroway, A. N., A Review of the Crystal Structures of Common Explosives Part I: RDX, HMX, TNT, PETN, Tetryl. In Laboratory, N. R., Ed. 2001; pp 1-30.
5. Badgujar, D. M.; Talawar, M. B.; Asthana, S. N.; Mahulikar, P. P., Advances in science and technology of modern energetic materials: An overview. *J. Hazard Mater.* **2008,** *151*, 289-305.
6. Xu, J.; Tian, Y.; Liu, Y.; Zhang, H.; Shu, Y.; Sun, J., Polymorphism in hexanitrohexaxazaisowurtzitane crystallized from solution. *J. Cryst. Growth* **2012,** *354*, 13-19.
7. Vrcelji, R. M.; Sherwood, J. N.; Kennedy, A. R.; Gallagher, H. G.; Gelbrich, T., Polymorphism in 2-4-6 Trinitrotoluene. *Cryst. Growth Des.* **2003,** *3*, 1027-1032.
8. C. P. Achuthan, C. P.; Jose, C. I., Studies on Octahydro-1,3,5,7-Tetranitro-1,3,5,7-Tetrazocine (HMX) Polymorphism. *Propellants, Explos. Pyrotech.* **1990,** *15*, 271-275.
9. Landenberger, K. B.; Matzger, A. J., Cocrystals of 1,3,5,7-Tetranitro-1,3,5,7-tetracyclooctane (HMX). *Cryst. Growth Des.* **2012,** *12*, 3603-3609.
10. Bolton, O.; Simke, L. R.; Pagoria, P. F.; Matzger, A. J., High Power Explosive with Good Sensitivity: A 2:1 Cocrystal of CL-20:HMX. *Cryst. Growth Des.* **2012,** *12*, 4311-4314.
11. Bennion, J. C.; Chowddhury, N.; Kampf, J. W.; Matzger, A. J., Hydrogen Peroxide Solvates of 2,4,6,8,10,12-Hexanitro-2,4,6,8,10,12-hexaazaisowurtzitane. *Angew. Chem. Int. Ed.* **2016,** *55*, 13118-13121.
12. The oxygen balance (OB) for an organic compound can be calculated using the following equation: $-1600(2a + 0.5b - d)(\mathrm{MW})^{-1}$, where a, b, c, and, d are the numbers of carbon, hydrogen, nitrogen, and oxygen atoms, respectively, in one formula unit of the material and the MW is the molecular weight for a formula unit of the material.
13. Nikitina, E. V.; Starova, G. L.; Frank-Kamenetskaya; Pevzner, M. S., *Kristallografiya* **1982,** *6*.
14. Haiges, R.; Bélanger-Chabot, G.; Kaplan, S. M.; Christe, K. O., Preparation and characterization of 3,5-dinitro-1*H*-1,2,4-triazole. *Dalton Trans.* **2015,** *44*, 7586-7594.
15. Main, P.; Cobbledick, R. E.; Small, R. W. H., Structure of the Fourth Form of 1,3,5,7-Tetranitro-1,3,5,7-tetraazacyclooctane* (γ-HMX), $2C_4H_8N_8O_8.0.5H_2O$. *Acta Cryst.* **1985,** *C41*, 1351-1354.
16. Nielsen, A. T.; Chaffin, A. P.; Christian, S. L.; Moore, D. W.; Nadler, M. P.; Nissan, R. A.; Vanderah, D. J., Synthesis of Polyazapolycyclic Caged Polynitramines. *Tetrahedron* **1998,** *54*, 11793-11812.
17. Dippold, A. A.; Klapötke, T. M., Nitrogen-Rich Bis-1,2,4-triazoles--A Comparative Study of Structural and Energetic Properties. *Chem Eur. J.* **2012,** *18*, 16742-16753.
18. Schmidt, R. D.; Lee, G. S.; Pagoria, P. F.; Mitchell, A. R.; Gilardi, R., Synthesis and Properties of a New Explosive, 4-Amino-3,5-dinitro-1H-Pyrazole (LLM-116). In Laboratory, L. L. N., Ed. Livermore, CA, 2001.

19. Gao, H.; Shreeve, J. M., Azole-Based Energetic Salts. *Chem. Rev.* **2011,** *111*, 7377-7436.
20. Bennion, J. C.; McBain, A.; Son, S. F.; Matzger, A. J., Design and Synthesis of a Series of Nitrogen-Rich Energetic Cocrystals of 5,5'-Dinitro-2*H*,2*H*'-3,3'-bi-1,2,4-triazole (DNBT). *Cryst. Growth Des.* **2015,** *15*, 2545-2549.
21. Cheetah 7.0 calculations were performed with the Sandia JCZS product library revision 32.
22. Chernyshov, I. Y.; Vener, M. V.; Prikhodchenko, P. V.; Medvedev, A. G.; Lev, O.; Churakov, A. V., Peroxosolvates: Formation Criteria, H_2O_2 Hydrogen Bonding, and Isomorphism with the Corresponding Hydrates. *Cryst. Growth Des.* **2017,** *17*, 214-220.
23. Olovsson, I.; Templeton, D. H., The Crystal Structure of Hydrogen Peroxide Dihydrate. *Acta Chem. Scand.* **1960,** *14*, 1325-1332.
24. Fischer, D.; Klapotke, T.; Stierstorfer, J. Process for preparing 3,3'-dinitro-5,5'-bis(1h-1,2,4-triazole). D.E. Patent 102015009297A1, January 26, 2017.
25. Ebelke, W. H., Hydrogen Peroxide Handbook. In Laboratory, A. F. P., Ed. Edwards Air Force Base, CA, 1967.
26. Dolomanov, O. V.; Bourhis, L. J.; Gildea, R. J.; Howard, J. A. K.; Puschmann, H., OLEX2: A complete structure solution, refinement and analysis program. *J. Appl. Cryst.* **2009,** *42*.
27. Sheldrick, G. M., SHELXT - Integrated space-group and crystal-structure determination. *Acta Cryst.* **2015,** *A71*.
28. Sheldrick, G. M., Crystal structure refinement with SHELXL. *Acta Cryst.* **2015,** *C71*, 3.

Chapter 4 : Room-Temperature Ferroelectricity in an Organic Cocrystal*

4.1 Introduction

Crystalline charge transfer (CT) complexes formed between neutral molecular components demonstrate a broad range of fractional electron transfer that predicates applications in most fields of electronics.[1-9] With benefits offered by solution processability, flexibility, reduced toxicity, and ease of tunability, synthesis, and purification, organic electronic materials are promising alternatives to traditional inorganics.[7, 10-12] Of particular interest is the application of CT cocrystals as displacive ferroelectrics in data storage.[12, 13] The exchangeable nature of the CT pair permits rapid screening of various molecular combinations relative to single-component materials; this is advantageous in the field of ferroelectric materials, which show stringent and statistically disfavored crystallographic requirements. Taking advantage of this design feature, several organic CT ferroelectrics have been reported,[4, 5, 10-12, 14] although most of materials that have been discovered to date only exhibit ferroelectricity below room temperature.

Conventional design strategies towards displacive ferroelectric cocrystals focus on tailoring the CT gap in 1D chains of alternating π-electron donor (*D*) and acceptor (*A*) molecules to achieve a transition between neutral (*DADA*…) and ionic (D^+A^- D^+A^-…) solid phases (NI transition)[15, 16] through a reversible Peierls-type lattice instability at the Curie temperature, T_C.[2-5,9-14,17-19] The Peierls distortion can manifest as a molecular deformation (Figure 4.1a) or displacement (Figure 4.1b) that polarizes the CT chain in the ionic/ferroelectric phase.[5,13] However, design strategies that leverage electronic instabilities modeled in 1D CT chains are

---

* Published: Wiscons, R. A.; Goud, N. R.; Damron, J. T.; Matzger, A. J. *Angew. Chem. Int. Ed.* **2018**, *57*, 9044-9047

limited in their ability to predict interchain interactions that may prevent structural transitions. We argue that the paucity of reported cocrystals that exhibit room temperature displacive ferroelectricity is due, in part, to design strategies that consider CT interactions as the driving force for the paraelectric-ferroelectric transition, while assuming that interchain interactions are non-participatory.

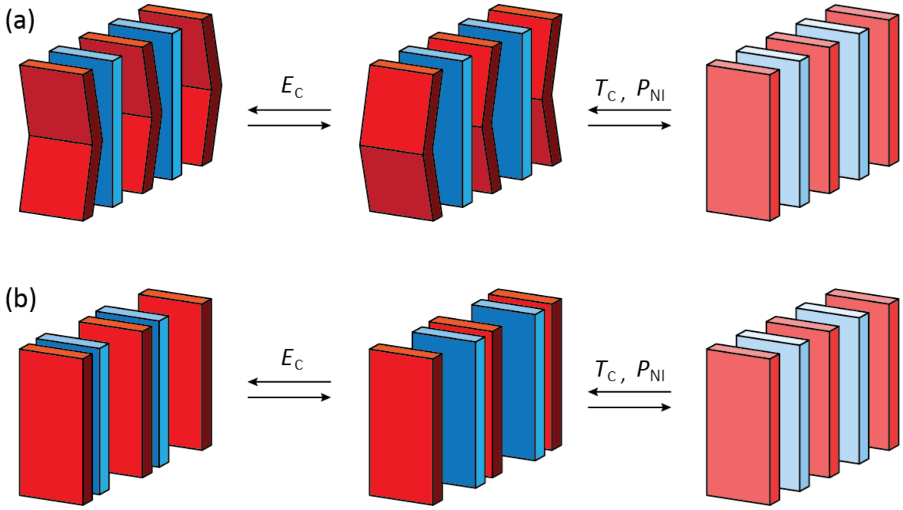

Figure 4.1. Mechanisms of Ferroelectricity in CT Cocrystals

Two mechanisms of displacive ferroelectric transitioning in CT cocrystals: (a) molecular deformation and (b) molecular displacement (adapted from Horiuchi *et al.*). The polarization direction can be switched under a coercive electric field, E_C, and the ferroelectric-paraelectric transition can be thermally induced at the T_C or the NI transition pressure, P_{NI}.

Herein, a room-temperature displacive ferroelectric CT cocrystal formed between acenaphthene, AN, and 2,3,5,6-tetrafluoro-7,7,8,8-tetracyanoquinodimethane, F_4TCNQ, (see Figure 4.2) is presented. A record high T_C of 68 °C allows room temperature ferroelectricity in AN-F_4TCNQ; the T_C corresponds to an activated by rotational motion in AN that decouples AN-F_4TCNQ dimers. Weak electronic coupling between AN and F_4TCNQ, as measured by Raman spectroscopy, supports the claim that the mechanism of the ferroelectric-paraelectric transition is primarily structural. No formal NI transition occurs at the T_C although this material displays switchable remanent polarization, prompting reevaluation of conventional redox potential-focused design strategies. AN-F_4TCNQ highlights the importance of interchain interactions and molecular dynamics in the design of CT cocrystals that undergo ferroelectric transitions and provides critical insights to improve the diversity and reliability of subsequent ferroelectric design strategies.

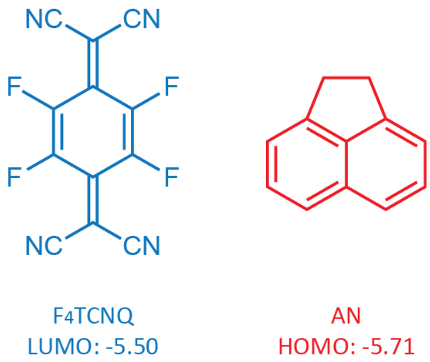

Figure 4.2. Chemical Structures of F_4TCNQ and AN

Chemical structures of F_4TCNQ (CT acceptor) and AN (CT donor) and calculated (B3LYP/6-311G**) positions of the frontier molecular orbital energies for the isolated gas-phase molecules.

4.2 Results and Discussion

AN and F_4TCNQ were selected as cocrystallization partners because they display a minimal calculated difference in position of the HOMO and LUMO energy levels for isolated gas-phase *D* and *A* molecules (see Figure 4.2). This approach is consistent with current strategies towards CT cocrystal design.[6, 8] Cocrystals of AN-F_4TCNQ were grown by solvent evaporation from an equimolar acetonitrile solution. Thermal cycling by differential scanning calorimetry (DSC, Figure 4.3) revealed a reversible endotherm upon heating at 341.1 K (68.1 °C) and an exotherm at 335.0 K (62.0 °C) upon cooling.

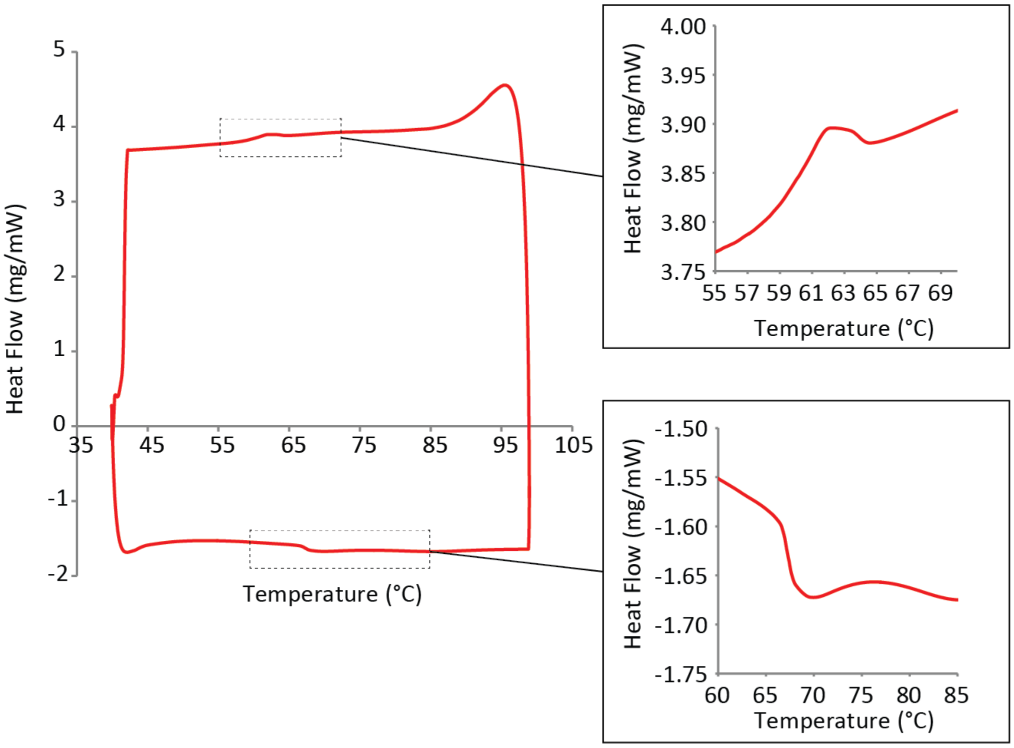

Figure 4.3. DSC Trace of the AN-F_4TCNQ Cocrystal

Typical DSC trace for AN-F_4TCNQ with heating and cooling events shown separately to magnify the endothermic and exothermic events. Exothermic heat flow is shown as upward peaks.

4.2.1 The Crystal Structure of AN-F_4TCNQ

Single-crystal XRD (SCXRD) structures were obtained at 85 K, 293 K (20 °C), and 348 K (75 °C). At both 85 K and 293 K, the cocrystal solves in the polar *Pc* space group, whereas the 348 K crystal structure becomes centrosymmetric ($P2_1/c$). AN-F_4TCNQ adopts a mixed-stack motif parallel to the *a*-axis (Figure 4.4a). Interplanar spacings reveal that the molecules are dimerized (D^+A^- D^+A^-…) in the two low temperature structures with alternating long and short π-stacking distances (3.415 Å and 3.369 Å at 293 K measured *D* centroid to *A* plane), while the high-temperature crystal structure is differentiated by a decoupling of the *DA* dimers, evenly spacing the *D* and *A* molecules (3.461 Å), and a 180° rotational disorder of AN (Figure 4.4b).

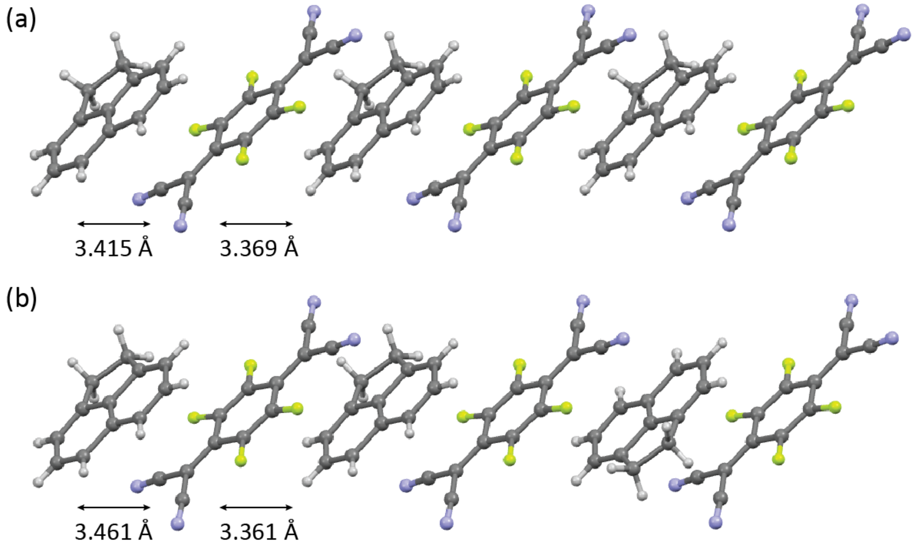

Figure 4.4. π-Stacking Interactions in AN-F_4TCNQ

1D chains of alternating AN and F_4TCNQ molecules along the *a*-axis from the (a) room temperature crystal structure and (b) high-temperature crystal structure.

Despite the AN rotational disorder, 3D crystallinity is maintained in the $P2_1/c$ phase with close interchain contacts formed between C-**F** and **C**≡N on neighboring F_4TCNQ molecules (Figure 4.5a,b). These contacts are present in the *Pc* (at 293 K) and $P2_1/c$ phases at distances between 3.05 and 3.07 Å., Furthermore, the interchain contacts are strengthened through C≡N···H-C interactions[20] (Figure 4.5c,d) that are present in all three crystal structures at an interaction distance of 2.46 Å at 293 K (normalized hydrogen positions).

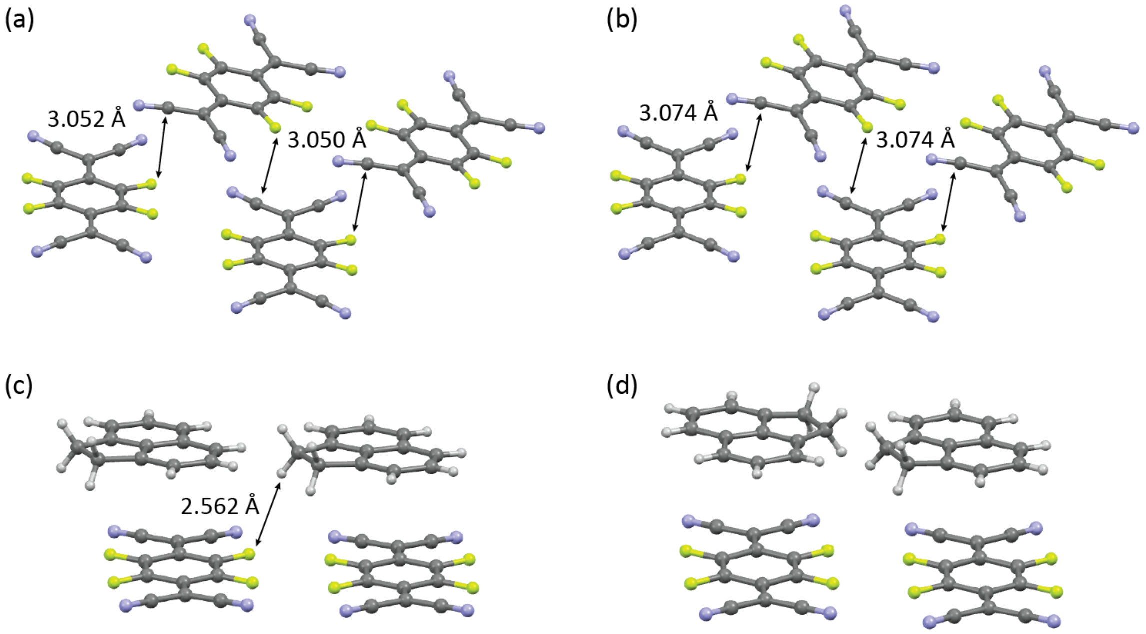

Figure 4.5. C-F···C≡N and C≡N···H-C Interactions in AN-F_4TCNQ

Chains of C-F···C≡N interactions formed between neighboring F_4TCNQ molecules in the (a) room temperature and (b) high-temperature crystal structures. View highlighting the C≡N···H-C interactions in the (c) room temperature and (d) high-temperature crystal structures.

4.2.2 Room Temperature Polarization Hysteresis

Given that the phase change in AN-F_4TCNQ is accompanied by a reversible symmetry change (noncentrosymmetric to centrosymmetric), the room-temperature ferroelectricity was investigated by measuring polarization hysteresis parallel to the CT stacking direction (*a*-axis) on single crystals. Bravais, Friedel, Donnay, and Harker (BFDH) morphology predictions produced by Mercury 3.7 (Cambridge Crystallographic Data Centre) was used to guide the placement of silver electrode contacts on the (100) and (-100) faces (see Figure 4.6).

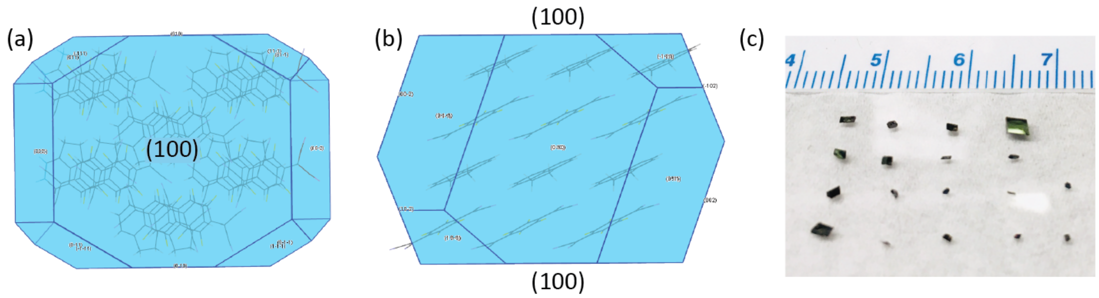

Figure 4.6. The Morphology of the AN-F_4TCNQ Cocrystal

(a,b) BFDH predicted morphologies for the AN-F_4TCNQ cocrystal structure and (c) image of the cocrystals grown by acetonitrile evaporation with graduations in units of millimeters.

Polarization hysteresis loops measured at room temperature show dielectric leakage that becomes more dramatic upon scanning to lower frequencies. Positive-up-negative-down (PUND) pulse measurements reveal that two components (dielectric and ferroelectric) contribute to the overall polarization intensity and, at a pulse width optimized for the ferroelectric component, the dielectric component contributes to 95% of the overall intensity and the ferroelectric component the other 5% (see Figure 4.7a). The dielectric component is likely associated with rotation of AN under an applied electric field due to its dipole moment, which is consistent with the increased motion of AN observed in the crystal structure of the high-temperature $P2_1/c$ phase. Remanent polarization hysteresis loops were measured using a double triangular waveform voltage to remove the effects of non-hysteresis character (see Figure 4.7b). Room temperature ferroelectricity in AN-F_4TCNQ was confirmed and the remanent polarization (Pr) was measured up to 0.08 ± 0.01 nC/cm^2. By comparison to the model displacive ferroelectric formed between tetrathiafulvalene (TTF) and *p*-chloranil (CA), the Pr of AN-F_4TCNQ is small; however, AN-F_4TCNQ represents remarkable progress for displacive ferroelectric cocrystals as it displays ferroelectric behavior above room temperature, while TTF-CA is only ferroelectric below 81 K.

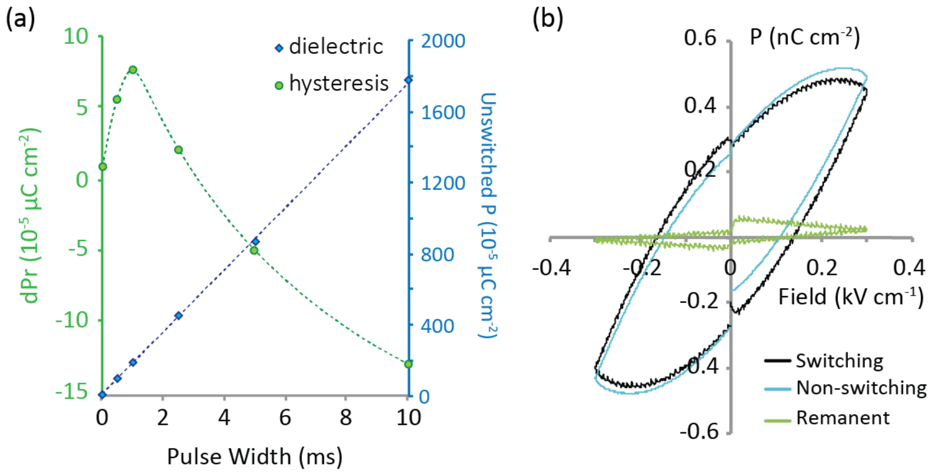

Figure 4.7. Electrical Characterization of the AN-F_4TCNQ Cocrystal

(a) Pulse width-dependent dielectric and ferroelectric contributions to the total polarization AN-F_4TCNQ. (b) Remanent polarization hysteresis plot for AN-F_4TCNQ.

4.2.3 The Degree of Charge-Transfer in AN-F_4TCNQ

Electronic coupling between AN and F_4TCNQ was further characterized by calculating the ionicity (ρ) of the cocrystal during the ferroelectric-paraelectric transition. Ionicity values were calculated from Raman spectra[8, 21-24] obtained between 30 °C and 80 °C, revealing a minor shift in ionicity between 65 and 70 °C associated with the transition (see Table 4.1 and Figure 4.8). The ρ of the ionic phase was calculated at 0.3 e, which decreases to 0.2 e upon transitioning to the $P2_1/c$ phase. The $\Delta\rho$ for this material is 0.1 e (about one fourth that of TTF-CA), implicating that a *true* NI transition[22] is not crossed.

Table 4.1. Table of Raman Peak Values and Salculated Ionicities

Temperature (°C)	*AN-F_4TCNQ (cm^{-1})*	*F_4TCNQ (cm^{-1})*	*[K][F_4TCNQ] (cm^{-1})*	*Ionicity (e)*
23	2223.23	2225.65	2217.66	0.30
30	2223.23	2225.65	2217.66	0.30
35	2222.82	2225.65	2217.66	0.35
40	2222.82	2225.65	2217.66	0.35
45	2223.03	2225.65	2217.66	0.33

50	2222.82	2225.65	2217.66	0.35
55	2223.03	2225.65	2217.66	0.33
60	2222.82	2225.65	2217.66	0.35
65	2222.82	2224.96	2217.66	0.30
70	2223.40	2224.96	2217.66	0.21
75	2223.40	2224.96	2217.66	0.21

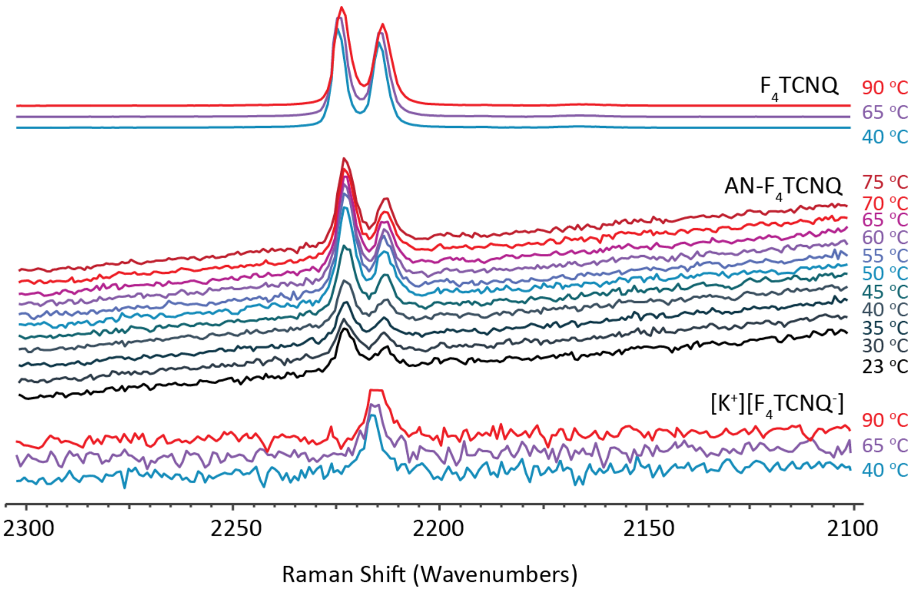

Figure 4.8. VT-Raman Ppectroscopy for AN-F_4TCNQ

Variable-temperature Raman spectra for AN-F_4TCNQ collected in static scan mode between 2100 – 2300 cm^{-1} at temperatures ranging from 23 – 75 °C.

4.2.4 Investigating the Mechanism of AN-F_4TCNQ Ferroelectricity

By assuming a double-well potential model for a ferroelectric transition,[25] the T_C can be used to estimate the energy difference between the ferroelectric and paraelectric states. Participation of non-CT interactions altered during the transition can be probed by comparing the T_C of non-deuterated and perdeuterated analogues of ferroelectric materials. For example, TTF-CA exhibits a T_C 2-5 K lower than d_4TTF-CA,[5, 26] which was attributed to lengthening, destabilization, and symmetrization of interchain C-H···O hydrogen bonds upon transitioning to the paraelectric (neutral) phase.[27]

Investigation into the ferroelectric-paraelectric transition mechanism for AN-F_4TCNQ began with synthesis of d_{10}AN-F_4TCNQ. The DSC trace revealed a reversible endotherm at 69.2 °C upon heating and an exotherm at 62.0 °C upon cooling (see Figure 4.9). The 1.1 °C increase in T_C upon deuteration is in the opposite direction of what would be expected for a change in redox potential due to the reduced hyperconjugative stabilization afforded by deuterium. This observation indicates that non-CT interactions contribute to the ferroelectric-paraelectric transition mechanism (*vide infra*).

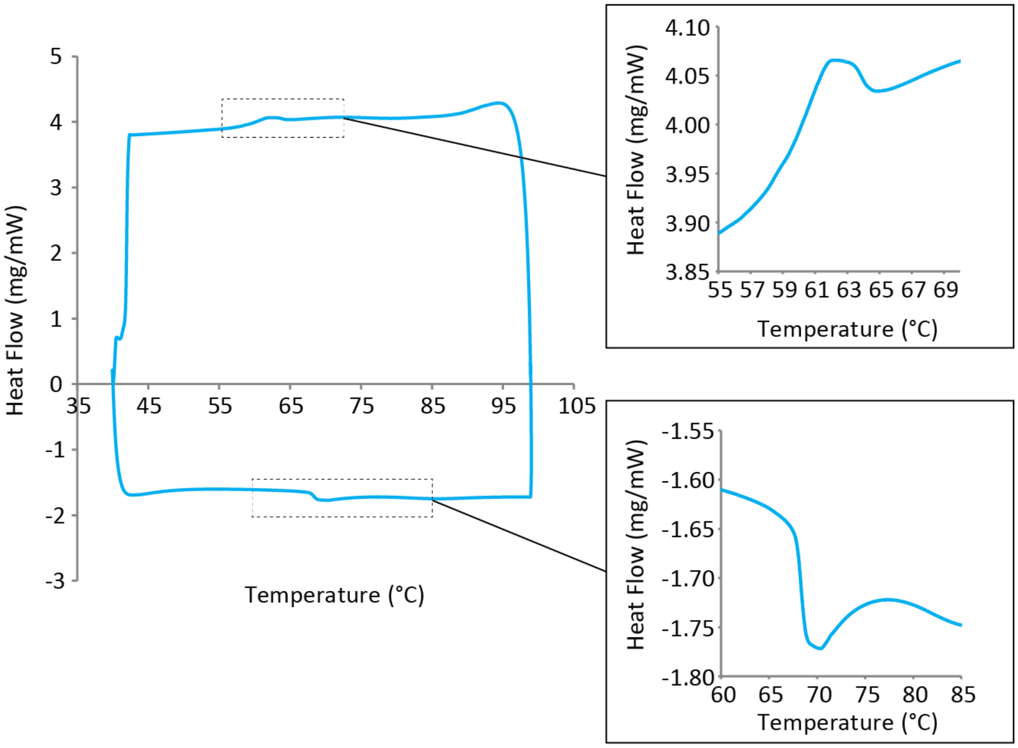

Figure 4.9. DSC Trace for d_{10}AN-F_4TCNQ

Typical cyclic DSC trace for d_{10}AN-F_4TCNQ with heating and cooling events shown separately to magnify the endothermic and exothermic events. Exothermic heat flow is shown as upwards peaks.

Examples of flip-flop and plastic ferroelectricity in CT metal-organic systems and antiferroelectric-paraelectric transitions in organic crystals have suggested the possibility of forming ferroelectrics in which structural transitions are controlled by activated vibrational and/or rotational modes. Such a mechanism would be consistent with the AN motion identified by SCXRD and dielectric leakage observed during polarization measurements. Evidence of dynamic molecular rotation was collected by solid-state ^{1}H magic-angle-spinning nuclear magnetic resonance (MAS-NMR) spectroscopy between 30 and 80 °C. Above 60 °C, the aromatic and non-aromatic proton environments in AN can be differentiated in the 1D ^{1}H spectra (Figure 4.10a); however, with a decrease in temperature, the methylene signal shifts downfield, appearing as a shoulder on the aromatic peak, while the aromatic signal shows progressive broadening upon cooling. The sharpening upon heating from 30 to 60 °C suggests that the transition is preceded by continuous structural changes and confirms that the AN rotational disorder observed by SCXRD is dynamic. The ^{1}H T_1 relaxation data collected between 30 and 80 °C is most suitably fit with a bicomponent T_1 curve. Both components show a decrease in relaxation time upon heating to 60 °C, which is likely a product of two effects: a decrease in CT and interruption of $C{\equiv}N\cdots H\text{-}C$ interactions due to rotational motion. At temperatures beyond 60 °C, an increase in the T_1 is measured, caused by a freeing of AN motion, pushing the dynamics past the T_1 minimum and lengthening the T_1 time. At and above the T_C, this effect becomes more dramatic (Figure 4.10b).

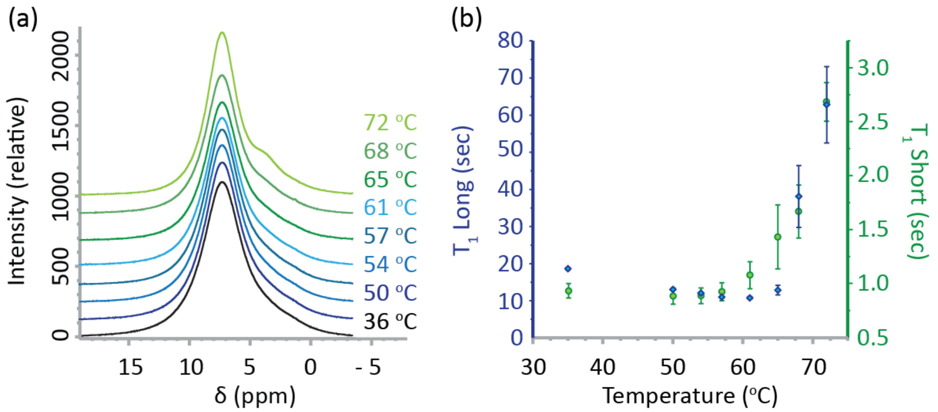

Figure 4.10. NMR Spectra and Relaxation Times for AN-F_4TCNQ

(a) 1D MAS-NMR ^{1}H spectra collected between 30 and 80 °C. (b) T_1 relaxation time for the long (blue) and short (green) components as a function of temperature.

The MAS-NMR studies prompted a targeted investigation of the C≡N···H-C interaction during the ferroelectric-paraelectric transition. Classical C≡N···H-O H-bonds show -Δ*H*° between 2-5 kcal mol^{-1} [28, 29] (likely lower in AN-F_4TCNQ due to the weaker donation), too low of an energetic barrier to independently prevent AN rotational motion at room temperature. The barrier to rotation is likely a convolution of the C≡N···H-C interaction and lattice reorganization enthalpies to accommodate AN rotation. The relative significances of these effects to the structural phase transition were studied by powder XRD (PXRD) and confirmed by SCXRD (see Figure 4.11 and Table 4.2). The 2θ shift in the reflections associated with the (010) and (002) interplanar spacings were monitored between 20 °C and 80 °C as these planes describe crystallographic expansions/contractions due to C≡N···H-C interactions and rotation-induced lattice deformation, respectively (see Figure 4.11a). As shown in Figure 4.11c, the reflection corresponding to the (010) plane does not significantly shift during the transition, indicating that destabilization and elongation of the C≡N···H-C interaction is not a dominant contributor to the structural transition observed by XRD. Contrastingly, the {002} interplanar spacings dramatically expand ~5 °C before the T_C. Activation of AN rotation is consistent with the preferential interplanar expansion between the {002} planes, which would account for additional enthalpic contributions to the barrier preventing ferroelectric-paraelectric transitioning at room temperature.

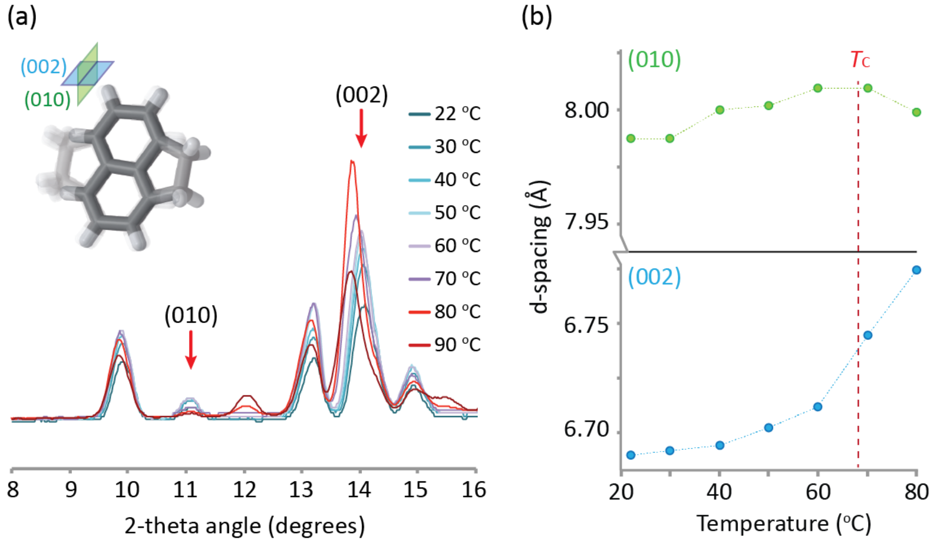

Figure 4.11. VT-PXRD Analysis of AN-F_4TCNQ

(a) Orientation of AN relative to the (002) and (010) Miller planes and VT-PXRD patterns of AN-F_4TCNQ taken between 22 and 80 °C. (b) The d-spacing expansion between the (010) and (002) Miller planes with increasing temperature.

Table 4.2. Unit Cell Parameters for AN-F_4TCNQ Collected by VT-SCXRD

Temp (°C)	*a* (Å)	*b* (Å)	*c* (Å)	(002) (Å)	β (°)	V (Å^3)
22(1)	9.462(4)	7.987(4)	13.368(6)	6.684(6)	109.46(4)	952.5(7)
30(1)	9.470(5)	7.986(5)	13.374(7)	6.687(7)	109.40(4)	954.3(7)
40(1)	9.476(4)	8.001(4)	13.381(4)	6.691(4)	109.31(4)	957.5(7)
50(1)	9.479(4)	8.001(6)	13.404(5)	6.702(5)	109.21(4)	960.0(9)
60(1)	9.482(5)	8.011(3)	13.451(5)	6.708(5)	109.13(4)	962.8(7)
70(1)	9.482(5)	8.013(5)	13.486(7)	6.743(7)	108.86(5)	969.6(9)
80(1)	9.494(5)	7.999(4)	13.550(7)	6.775(7)	108.55(4)	976.4(8)

4.3 Conclusion

It has been shown that AN-F_4TCNQ undergoes a space group change from *Pc* to $P2_1/c$ at 68 °C associated with a decrease in ionicity, consistent with a ferroelectric-paraelectric phase transition, despite weak electronic coupling between AN and F_4TCNQ. Activation of AN rotational motion was found to accompany the phase transition as shown by MAS-NMR and PXRD. Reversible remanent polarization of AN-F_4TCNQ was measured, confirming that this material is ferroelectric at room temperature although the mechanism of transition is primarily structural. Given these findings, we suggest inclusion of interchain interactions and molecular dynamics that facilitate displacement events responsible for polarization switching in future design of ferroelectric CT cocrystals. Shifting from electronically-driven to structure-driven mechanisms allows a greater diversity of materials that undergo lattice-facilitated ferroelectric-paraelectric transitions to be accessed that may not be predicted by a 1D Peierls distortion model.

4.4 Experimental Methods

4.4.1 Calculations

AN and F_4TCNQ were selected as cocrystallization partners based on gas phase calculations of the HOMO and LUMO energy levels, respectively (B3LYP/6-31G**). Using this method the HOMO-LUMO energy gap was calculated to be 0.23 eV (the HOMO-LUMO energy gap for TTF-CA is calculated at 0.24 eV, using the same method).

4.4.2 Cocrystallization

Acenaphthene (Acros Organics) and d_{10}-acenaphthene (Sigma-Aldrich) were used as received, whereas F_4TCNQ (Ossila) was purified by zone sublimation to remove colored impurities before use. Single-crystals of AN-F_4TCNQ and d_{10}AN-F_4TCNQ were produced by slow evaporation from a 7.2 mM 1:1 stoichiometric ratio in acetonitrile (dried over molecular sieves) on polypropylene substrates. Single crystals were harvested and dried under vacuum before further characterization.

4.4.3 Single-Crystal Structure Determination

Single-crystal X-ray diffraction data for AN-F_4TCNQ was collected using a Rigaku AFC10K Saturn 944+ CCD-based X-ray diffractometer equipped with a low temperature device and Micromax-007HF Cu-target microfocus rotating anode (λ = 1.54187 Å) operated at 1.2 kW power (40 kV, 30 mA). X-ray intensities were measured at 85(1), 293(1), and 348(1) K with the detector placed 42.00 mm from the crystal. The data were processed with CrystalClear 2.0 (Rigaku)[30] and corrected for absorption. The structures were solved and refined with the Bruker SHELXTL (version 2008/4)[31] software package using direct methods. All non-hydrogen atoms were refined anisotropically with hydrogen atoms placed in a combination of refined and idealized positions. SCXRD data for d_{10}AN-F_4TCNQ was collected using a Rigaku XtaLAB Synergy-S X-ray diffractometer equipped with a low temperature device and a PhotonJet-S microfocus Cu source (λ = 1.54187 Å) operated at 50 kV and 1 mA. X-ray intensities were measured at 295(1) with the HyPix-6000HE detector placed 34.00 mm from the sample. The data were processed with CrysAlisPro v38.46 (Rigaku Oxford Diffraction) and corrected for absorption. The structures were solved in OLEX2[32] using SHELXT[33] and refined using

SHELXL[34]. All non-hydrogen atoms were refined anisotropically with hydrogen atoms placed in a combination of refined and idealized positions.

4.4.4 Powder X-ray diffraction

Variable-temperature powder XRD patterns were measured on a Rigaku R-Axis Spider diffractometer using Cu-Kα radiation (λ = 1.54187 Å) and operating at 40 kV and 44 mA. Samples were mounted on a CryoLoop™ and images were collected for 3 minutes with rotation of the sample about the ϕ-axis at 10°/sec, oscillating ω between 80° and 140° at 1°/sec with χ fixed at 45°. The sample collection temperature was set to temperatures between 295(1) and 348(1) K in 5 K increments via an Oxford Cryostream Plus Controller. The images were integrated from 2 to 50° with a 0.02° step size using AreaMax 2.0 software (Rigaku). The data were processed using Jade 8 XRD Pattern Processing, Identification & Quantification analysis software (Materials Data, Inc.).[35]

4.4.5 Variable-Temperature Raman Spectroscopy

Variable-temperature Raman spectra were collected using a Renishaw inVia Raman Microscope equipped with a Leica microscope, 785 nm laser, 1200 lines/mm grating, 65 μm slit, and a RenCam CCD detector. Calibration was performed using a silicon standard in static mode. Spectra were collected in static mode with the spectral window centered about 2200 cm^{-1} and analyzed using the WiRE 3.4 software package (Renishaw). The sample collection temperature was controlled by a Linkam Scientific TMS 94 hot stage attachment through the WiRE 3.4 collection software.

4.4.6 Polarization Hysteresis Measurements

Electrical measurements were taken on single crystals contacted with silver paint. BFDH morphology prediction was produced by Mercury 3.7 offered by the CCDC and used to guide the placement of the electrode contacts on the (100) and (-100) faces. The *P-E* hysteresis loops were collected at room temperature on a ferroelectric testing probe station (Radiant Technologies Inc. Ferroelectric Test System) operated using Vision Data Acquisition Software (Radiant Technologies Inc.) using an alternating triangular double-wave field (preset-delay-measurement). PUND tests were also performed on single crystals using the Radiant Technologies Inc. Ferroelectric Testing System. The data provided in this manuscript were collected from two representative single crystals. Despite guidance from morphology predictions, contact placement was imperfect for several samples due to the blocky morphology of the crystal, and these samples showed unreliable and unsymmetrical polarization loops with no remanent behavior. It was concluded that, although sample measurements were reliable for well-placed electrodes, the *P-E* measurements are very specific to sample orientation.

4.4.7 Solid-state Magic-Angle-Spinning Nuclear Magnetic Resonance Spectroscopy

All ^{1}H NMR data was collected on a Bruker Avance III spectrometer at 400 MHz ^{1}H Larmor frequency using a Bruker 2.5mm probe under 20 kHz Magic Angle Spinning frequency. The probe temperature was calibrated using KBr[36] and the CS referenced to adamantane. The ^{1}H T_1 relaxation times were measured by saturation recovery with a 'Magic Sandwich Echo' before detection for background suppression and refocusing of some portion of the homonuclear dipolar coupling. The experiments were collected with 8 scans and a recycle delay of 5 s. The 1D spectra were taken from the final time point in the T_1 sequence at any given temperature. The saturation recovery experiments were assessed with a bicomponent fit, which modeled the data more appropriately than using a single component. The bimodal behavior of the curves are more pronounced at higher temperatures which can be seen in Figure 4.10b.

4.5 References

1. Soos, Z. G., Theory of Pi-Molecular Charge-Transfer Crystals. *Annu. Rev. Phys. Chem.* **1974,** *25*, 121-153.
2. Torrance, J. B.; Vazquez, J. E.; Mayerle, J. J.; Lee, V. Y., Discovery of a Neutral-to-Ionic Phase Transition in Organic Materials. *Phys. Rev. Lett.* **1981,** *46*, 253-257.
3. Torrance, J. B.; Girlando, A.; Mayerle, J. J.; Crowley, J. I.; Lee, V. Y.; Batail, P., Anomalous Nature of Neutral-to-Ionic Phase Transition in Tetrathiafulvalene-Chloranil. *Phys. Rev. Lett.* **1981,** *47*, 1747-1750.
4. Horiuchi, S.; Okimoto, Y.; Kuami, R.; Tokura, Y., Ferroelectric Valence Transition and Phase Diagram of a Series of Charge-Transfer Complexes of 4,4'-Dimethyltetrathiafulvalene and Tetrahalo-p-benzoquinones. *J. Am. Chem. Soc.* **2001,** *123*, 665-670.
5. Horiuchi, S.; Kumai, R.; Okimoto, Y.; Tokura, Y., Chemical approach to neutral-ionic valence instability, quantum phase transition, and relaxor ferroelectricity in organic charge-transfer complexes. *Chem. Phys.* **2006,** *325*, 78-91.
6. Shokaryev, I.; Buurma, A. J. C.; Jurchescu, O. D.; Uijttewaal, M. A.; de Wijs, G. A.; Palstra, T. T. M.; de Groot, R. A., Electronic Band Structure of Tetracene-TCNQ and Perylene-TCNQ Compounds. *J. Phys. Chem. A* **2008,** *112*, 2497-2502.
7. Goetz, K. P.; Vermeulen, D.; Payne, M. E.; Kloc, C.; McNeil, L. E.; Jurchescu, O. D., Charge-transfer complexes: new perspectives on an old class of compounds. *J. Mater. Chem. C* **2014,** *2*, 3065-3076.
8. Goud, N. R.; Matzger, A. J., Impact of Hydrogen and Halogen Bonding Interactions on the Packing and Ionicity of Charge-Transfer Cocrystals. *Cryst. Growth Des.* **2017,** *17*, 328-336.
9. Horiuchi, S.; Okimoto, Y.; Kumai, R.; Tokura, Y., Quantum Phase Transition in Organic Charge-Transfer Complexes. *Science* **2003,** *299*, 229-232.
10. Tayi, A. S.; Kaeser, A.; Matsumo, M.; Aida, T.; Stupp, S. I., Supramolecular ferroelectrics. *Nat. Chem.* **2015,** *7*, 281-294.
11. Horiuchi, S.; Ishii, F.; Kumai, R.; Okimoto, Y.; Tachibana, H.; Nagaosa, N.; Tokura, Y., Ferroelectricity near room temperature in co-crystals of nonpolar organic molecules. *Nat. Mater.* **2005,** *4*, 163-166.
12. Chen, S.; Xiao, C. Z., Design of Ferroelectric Organic Molecular Crystals with Ultrahigh Polarization. *J. Am. Chem. Soc.* **2014,** *136*, 6428-6436.
13. Horiuchi, S.; Tokura, Y., Organic ferroelectrics. *Nature* **2008,** *7*, 357-366.
14. Tayi, A. S.; Shveyd, A. K.; Sue, A. C.-H.; Szarko, J. M.; Rolczynski, B. S.; Cao, D.; Kennedy, T. J.; Sarjeant, A. A.; Stern, C. L.; Paxton, W. F.; Wu, W.; Dey, S. K.; Fahrenbach, A. C.; Guest, J. R.; Mohseni, H.; Chen, L. X.; Wang, K. L.; Stoddart, J. F.; Stupp, S. I., Room-temperature ferroelectricity in supramolecular networks of charge-transfer complexes. *Nature* **2012,** *488*, 485-489.

15. McConnell, H. M.; Hoffman, B. M.; Metzger, R. M., Charge Transfer in Molecular Crystals. *Proc. Natl. Acad. Sci.* **1965,** *53*, 46-50.
16. Prout, C. K.; Wright, J. D., Observations on the Crystal Structure of Electron Donor-Acceptor Complexes. *Angew. Chem. Int. Ed.* **1968,** *7*, 659-667.
17. Horiuchi, S.; Kobayashi, K.; Kuami, R.; Minami, N.; Kagawa, F.; Tokura, Y., Quantum ferroelectricity in charge-transfer complex crystals. *Nat. Commun.* **2015,** *6*, 1-7.
18. Hubbard, J.; Torrance, J. B., Model of the Neutral-Ionic Phase Transformation. *Phys. Rev. Lett.* **1981,** *47*, 1750-1754.
19. Kagawa, F.; Horiuchi, S.; Tokunaga, M.; Fujioka, J.; Tokura, Y., Ferroelectricity in a one-dimensional organic quatum magnet. *Nat. Phys.* **2010,** *6*, 169-172.
20. Taylor, R.; Kennard, O., Crystallographic Evidence for the Existence of C-H···O, C-H···N, and C-H···Cl Hydrogen Bonds. *J. Am. Chem. Soc.* **1982,** *104*, 5063-5070.
21. Salmerón-Valverde, A.; Robles-Martínez, J. G.; García-Serrano, J.; Gómez, R.; Ridaura, R. M.; Quintana, M.; Zehe, A., A Study of the Degree of Charge Transfer in TTF Molecular Complexes with Nitro-Carboxylated Fluorene Derivatives. *Mol. Eng.* **1999,** *8*, 419-426.
22. Castagnetti, N.; Kociok-Köhn, G.; Da Como, E.; Girlando, A., Temperature-induced valence instability in the charge-transfer crystal TMB-TCNQ. *Phys. Rev. B* **2017,** *95*, 0241011-7.
23. Masino, M.; Girlando, A.; Brillante, A., Intermediate regime in pressure-induced neutral-ionic transition in tetrathiafulvalene-chloranil. *Phys. Rev. B* **2007,** *76*, 0641141-7.
24. Dengl, A.; Beyer, R.; Peterseim, T.; Ivek, T.; Untereiner, G.; Dressel, M., Evolution of ferroelectricity in tetrathiafulvalene-p-chloranil as a function of pressure and temperature. *J. Chem. Phys.* **2014,** *140*, 2445111-6.
25. Hill, N., A, Why Are There so Few Magnetic Ferroelectrics. *J. Phys. Chem. B* **2000,** *104*, 6694-6709.
26. Horiuchi, S.; Kumai, R.; Okimoto, Y.; Tokura, Y., Design of quantum neutral-ionic phase transition in organic charge-transfer complexes. *Synth. Met.* **2003,** *133-134*, 615-618.
27. Batail, P.; LaPlaca, S. J.; Mayerle, J. J.; Torrance, J. B., Structural Characterization of the Neutral-Ionic Phase Transition in Tetrathiafulvalene-Chloranil: Evidence for C-H···O Hydrogen Bonding. *J. Am. Chem. Soc.***1981,** *103*, 951-953.
28. Le Questel, J.-Y.; Berthelot, M.; Laurence, C., Hydrogen-bond acceptor properties of nitriles: a combined crystallographic and *ab initio* theoretical investigation. *J. Phys. Org. Chem.* **2000,** *13*, 347-358.
29. Domagala, M.; Grabowski, S. J., C-H···N and C-H···S Hydrogen Bonds-Influence of Hybridization on Their Strength. *J. Phys. Chem. A* **2005,** *109*, 5683-5688.
30. CrystalClear Expert 2.0 r12, Rigaku Americas and Rigaku Corporation (2011), Rigaku Americas, 9009, TX, USA 77381-5209, Rigaku Tokyo, 196-8666, Japan.
31. G. M. Sheldrick, SHELXTL, v. 2008/4; Bruker Analytical X-ray, Madison, WI, 2008.
32. Dolomanov, O. V.; Bourhis, L. J.; Gildea, R. J.; Howard, J. A. K.; Puschmann, H., OLEX2: A complete structure solution, refinement and analysis program. *J. Appl. Cryst.* **2009,** *42*, 339-341.
33. Sheldrick, G. M., SHELXT - Integrated space-group and crystal-structure determination. *Acta Cryst.* **2015,** *A71*, 3-8.
34. Sheldrick, G. M., Crystal structure refinement with SHELXL. *Acta Cryst.* **2015,** *C71*, 3-8.
35. Jade Plus 8.2 ed.; Materials Data, Inc. 1995-2007.

36. Thurber, K. R.; Tycko, R., Measurement of sample temperatures under magic-angle spinning from the chemical shift and spin-lattice relaxation rate of 79Br in KBr powder. *J. Magn. Reson.* **2009,** *196*, 84-87.

Chapter 5 : Quaternary CT Solid Solutions: Tunability through Stoichiometry[*]

5.1 Introduction

Organic semiconductors are attractive alternatives to conventional inorganic materials for device fabrication in transistors,[1-4] light-emitting diodes,[5, 6] and photovoltaics[7-9].[10-12] This trend towards discovering organic analogues for inorganics is motivated by potential for improved cost effectiveness,[7,8,10,12] air and moisture stability, decreased toxicity, compatibility with flexible substrates,[7,8,10,12] and solution processability[1,5,7,8,10]. In the case of conjugated polymers, solution processability enables the formation of binary and ternary polymer blends, which affords additional control over the light absorption profile and charge carrier transport.[7,8] Unfortunately, polymer blends suffer from phase separation leading to degraded device performance.[13] Crystalline small molecule-based semiconductors, such as rubrene,[10,12,14-16] pentacene,[10,12,16-18] and tetrathiafulvalene derivatives show spectacular performance,[19] although their electrical characteristics can rarely be tuned through blending because the crystallization process often, but not always,[20] excludes dopants.[21] Charge-transfer (CT) cocrystals based on donor-acceptor (*DA*) pairs address issues of crystallinity, broad visible light absorption, and electronic tunability; however, CT materials express an incredibly diverse range of properties that are strongly dependent on crystal packing,[11,22,23] making electronic performance difficult to predict or control.

Substitutional doping to produce solid solutions is a method by which fine control over electronic properties in inorganic materials is routinely achieved. Solid solutions are defined as multicomponent crystalline systems in which the concentrations of two or more components

---

[*] Published: Wiscons, R. A.; Coropceanu, V.; Matzger, A. J. *Chem. Mater.* DOI: 10.1021/acs.chemmater.9b00502

occupying the same lattice position can be continuously varied between two compositional limits (see Figure 5.1a). Solid solutions are challenging to discover in molecular materials because functional groups responsible for modifying the electronic properties of a molecule tend to exhibit unique interaction modes in the solid state.[24] As a result of this interaction selectivity, introduction of additional components often results in a physical mixture of multiple solid phases, or the emergence of a new packing motif upon stoichiometric inclusion of the desired compound. However, the likelihood of forming solid solutions is improved when the strongest intermolecular interactions present in the lattice remain conserved. Because charge-transfer interactions between donor and acceptor molecules can be maintained across compositional variation, CT crystals are uniquely well suited for the inclusion of additional molecular components (Figure 5.1b,c).

(a) Substitutional Alloy (Solid Solution)

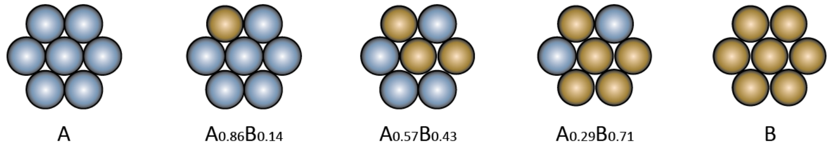

(b) Ternary Charge-Transfer Solid Solution

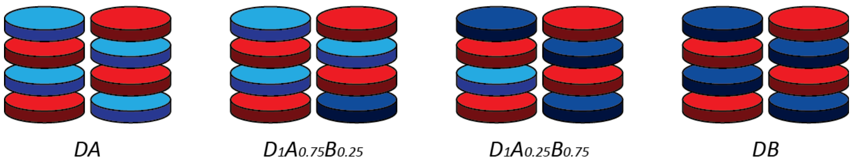

(c) Quaternary Charge-Transfer Solid Solution

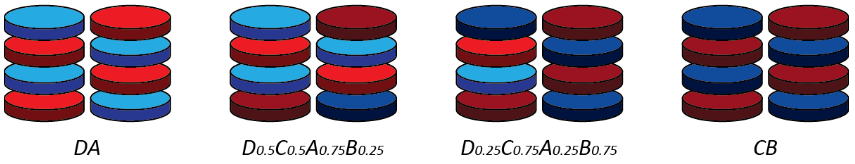

Figure 5.1. Substitutional Alloys and Solid Solutions

(a) Diagram of a substitutional alloy formed between two close-packed metals, (b) a ternary charge-transfer solid solution between donor (*D*) and acceptors (*A* or *B*) formed by varying the relative concentrations of molecules *A* and *B*, and (c) a quaternary charge-transfer solid solution between donor (*D* or *C*) and acceptors (*A* or *B*).

Herein we present the structural and electronic characterization of the CT complex that forms between 2,3-dichloro-5,6-dicyanobenzoquinone, DDQ, and 4,6-dimethyldibenzothiophene, DMDBT (see Figure 5.2). These compounds were selected as CT partners because they were predicted to yield a low-band gap material based on the difference in energy between the solution-phase electrochemical reduction/oxidation potentials, shown in Figure. We have found that 2,3-dibromo-5,6-dicyanobenzoquinone, DBQ, and 4,6-dimethyldibenzoselenophene, DMDBS, can be substituted into the DMDBT-DDQ cocrystal, forming the $\mathrm{DMDBT}_X\mathrm{DMDBS}_{(1-X)}\mathrm{DDQ}_Y\mathrm{DBQ}_{(1-Y)}$ quaternary CT solid solution. This solid solution displays composition-dependent ionicities and optical band gaps, indicating that the electronic behavior of the material can be modified through solid solution formation. This system demonstrates that small molecule CT electronics can be optimized using strategies that are traditionally implemented for inorganics to yield materials with improved performance relative to their respective end members.

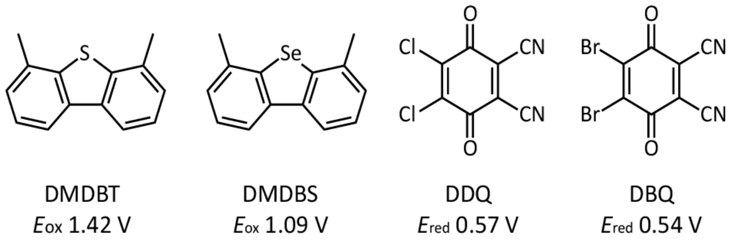

Figure 5.2. Molecular Structures of *D* and *A* Species

Molecular structures and oxidation potentials (versus SCE) for 4,6-dimethyldibenzothiophene (DMDBT) and 4,6-dimethyldibenzoselenophene (DMDBS); molecular structures and reduction potentials[25] (versus SCE) for 2,3-dichloro-5,6-dicyanobenzoquinone (DDQ) and 2,3-dibromo-5,6-dicyanobenzoquinone (DBQ).

5.2 Results and Discussion

5.2.1 Crystal Structures of the Cocrystal Phases

Cocrystals of DMDBT-DDQ, DMDBT-DBQ, DMDBS-DDQ, and DMDBS-DBQ were grown by solvent evaporation from acetonitrile solutions. The resultant crystals are deep maroon and prismatic in habit. The crystal structures of DMDBT-DDQ, DMDBT-DBQ, and DMDBS-DBQ were elucidated by single-crystal X-ray diffraction (SCXRD), revealing all three as isostructural, solving in the polar *Cmc*2$_1$ space group (see Table 5.1). DMDBS-DDQ is in the *P*-1 space group and shows a unique packing motif compared to the other cocrystal structures (see Table 5.1).

Table 5.1. Crystallographic Data for the CT Cocrystals

	DMDBT-DDQ	DMDBT-DBQ	DMDBS-DBQ	DMDBS-DDQ
Space Group	*Cmc*2$_1$	*Cmc*2$_1$	*Cmc*2$_1$	*P*-1
a (Å)	6.57483(12)	6.60920(10)	6.64274(17)	6.6291(5)
b (Å)	18.3640(3)	18.3407(2)	18.4437(5)	9.7060(7)
c (Å)	16.5153(2)	16.82770(10)	16.9726(4)	16.5873(7)
α (°)	90	90	90	77.051(5)
β (°)	90	90	90	88.795(4)
γ (°)	90	90	90	72.485(6)
V (Å^3)	1994.06	2039.81	2079.43	990.661

The isostructural materials crystallize in a 1:1 stoichiometry between donor and acceptor molecules and form mixed CT stacks that are free of Peierls distortions parallel to the *a*-axis, (Figure 5.3). In these three crystal structures, n→σ-hole halogen bonds, donated by the halogen atoms on the π-electron acceptors to the chalcogen atoms and nitrile groups on the nearest in-plane neighbors, form close interactions perpendicular to the π-stacking direction (Figure 5.4).

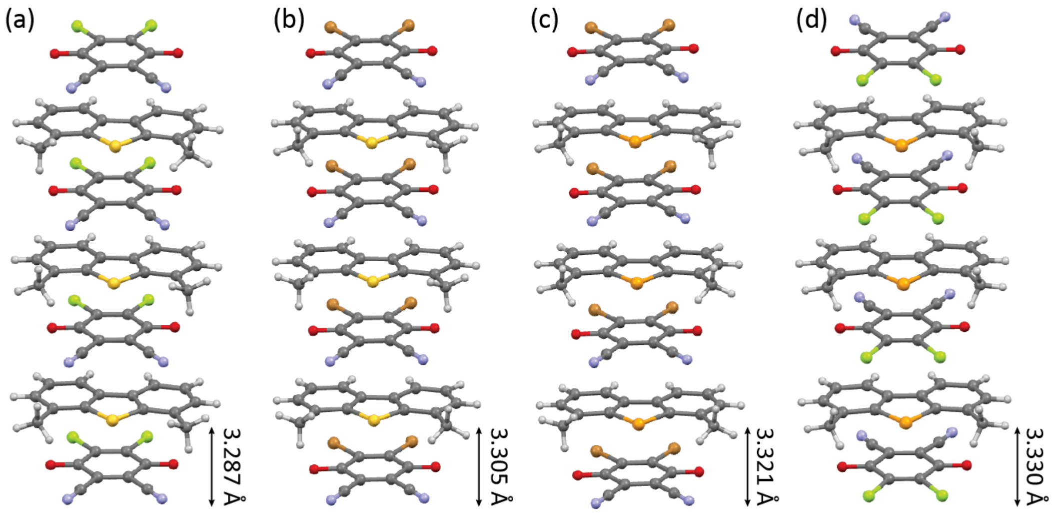

Figure 5.3. π-stacking Interactions in the CT Cocrystals

View along the *a*-axis of (a) DMDBT-DDQ, (b) DMDBT-DBQ, (c) DMDBS-DBQ, and (d) DMDBS-DDQ, highlighting the π-stacking direction of the cocrystal structures.

Remarkably, closer halogen bonding interactions are present in DMDBT-DBQ than DMDBT-DDQ, which implies that halogen bonding plays a significant role in the crystal packing motif of these structures, especially when the difference in atomic radii between Cl (1.75 Å)[26] and Br (1.85 Å)[26] is considered. Shorter halogen bonding interactions arise in DMDBT-DBQ because the σ-hole is more pronounced in Br than Cl due to greater atomic polarizability.

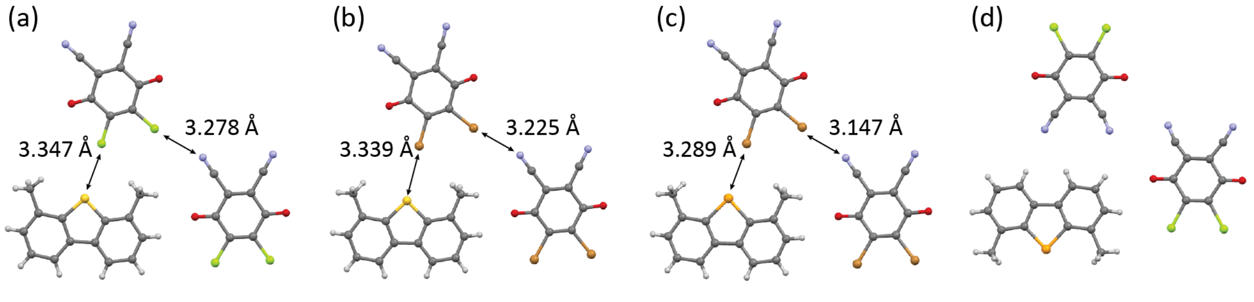

Figure 5.4. Halogen Bonding Interactions in the CT Cocrystals

Halogen bonding interactions present in (a) DMDBT-DDQ, (b) DMDBT-DBQ, (c) DMDBS-DBQ, and (d) DMDBS-DDQ.

The atomic polarizability of the halogen atoms in DDQ and DBQ can be visualized using electrostatic potential maps of DDQ and DBQ and quantified by identifying the potential energy maxima, $V_{s,max}$, on these surfaces (Figure 5.5), which show a region of greater electron deficiency on DBQ relative to DDQ and resulting in more favorable interaction with the lone pairs on the sulfur atom and nitrile groups.

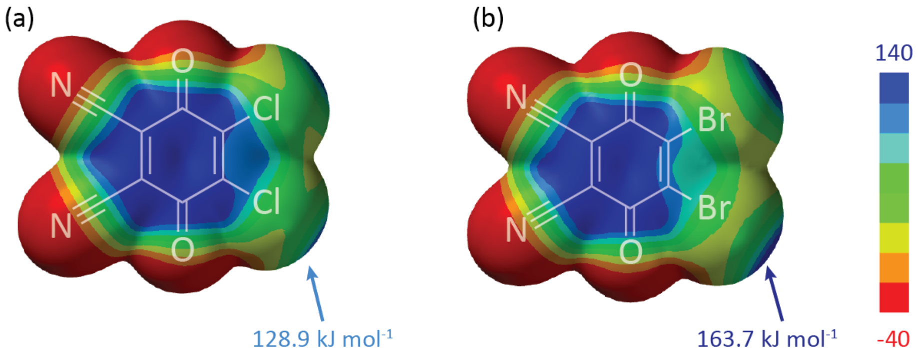

Figure 5.5. Electrostatic Potential Maps

Electrostatic potential maps calculated using B3LYP/6-311G**[27,28] for (a) DDQ and (b) DBQ with a common scale for the color bands shown on the right in kJ mol^{-1} and the $V_{s,max}$ values given in blue text.

5.2.2 Electronic Coupling in the Isomorphous Cocrystals

It has been demonstrated that strong donor-acceptor interactions in cocrystals facilitate efficient charge carrier transport along the donor-acceptor stacks.[12,29] Using density functional theory, effective electron and hole transfer integrals, t_{eff}(electron) and t_{eff}(hole) along the *DA* stacks were calculated from crystal structures of DMDBT-DDQ, DMDBT-DBQ, and DMDBS-DBQ. The t_{eff} values represent the strength of electronic coupling between two closest acceptor (donor) molecules along the -A-D-A-D- stacks resulting from the mixing of their frontier orbitals with the orbitals of the "bridging" donor (acceptor) molecule.[12] All three materials are found to have large t_{eff}(electron) values at 96 meV (DMDBT-DDQ), 101 meV (DMDBT-DBQ), and 89 meV (DMDBS-DBQ) and all three structures show small t_{eff}(hole) values, indicating that all three systems may show very good electron transport properties. For the sake of comparison, the largest t_{eff} for electrons and holes in pentacene are around 85 meV.[18] The results obtained for the effective hole and electron transfer integrals are supported by the crystal band structure calculations showing that the width of the conduction band in all three cocrystals is significantly larger than the width of the valence band (see Figure 5.6). To explore whether the *DA* electronic interactions could be more finely controlled, the possibility of forming ternary solid solution between the isomorphous phases was investigated.

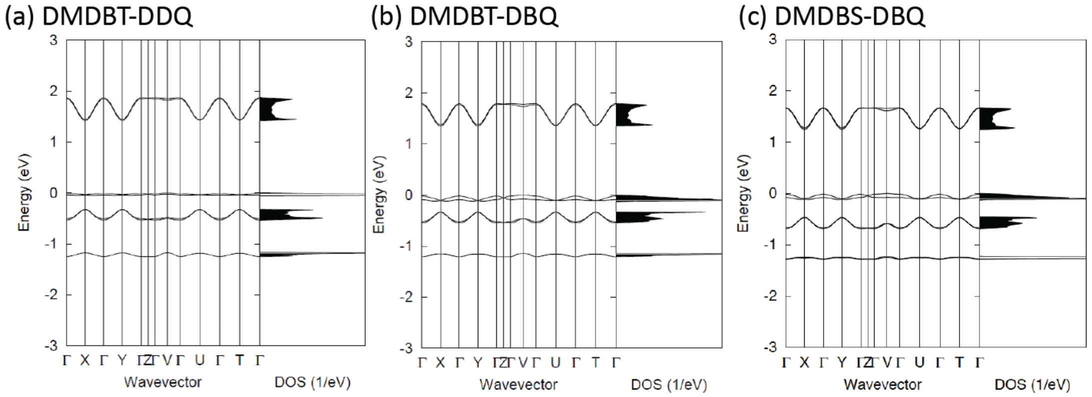
(a) DMDBT-DDQ (b) DMDBT-DBQ (c) DMDBS-DBQ

Figure 5.6. Electronic Structure Diagrams

Band structure (left) and density of states (right) diagrams for (a) DMDBT-DDQ, (b) DMDBT-DBQ, and (c) DMDBS-DBQ.

5.2.3 Crystallization and characterization of CT solid solutions

Single crystals of the ternary solid solutions DMDBT$_1$DDQ$_Y$DBQ$_{(1-Y)}$ and DMDBT$_X$DMDBS$_{(1-X)}$DBQ$_1$ were grown from acetonitrile solutions and scanning electron microscopy energy dispersive X-ray spectroscopy (SEM-EDS) was used to determine the Cl/Br and S/Se atomic ratios across single crystals (see Figure 5.7). The S/Se ratios were calibrated using the Br signal intensity from DMDBT-DBQ because the Kα Se and Br EDS signals overlap.

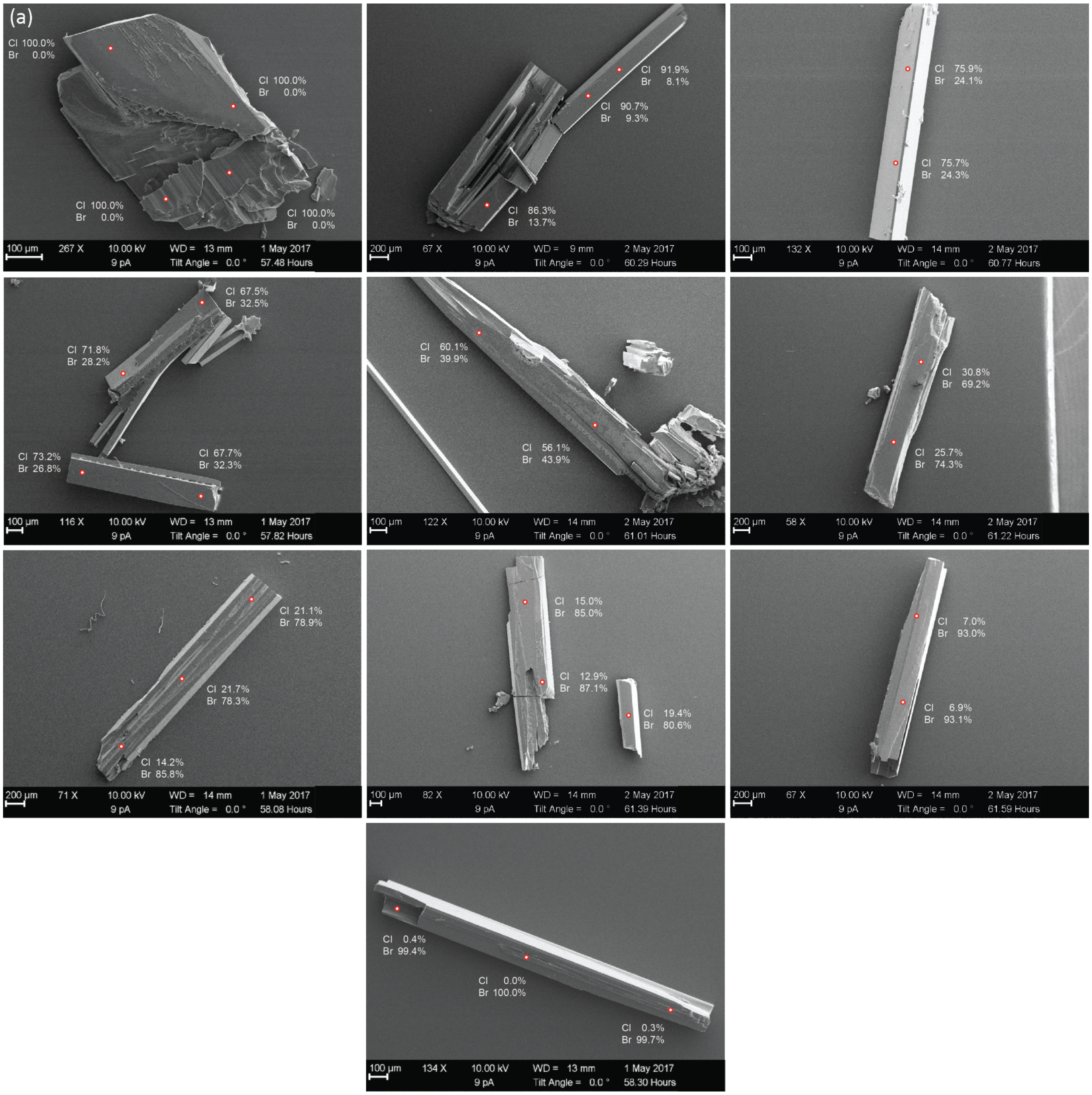
(a)
Cl 100.0%
Br 0.0%
Cl 100.0%
Br 0.0%
Cl 100.0%
Br 0.0%
Cl 100.0%
Br 0.0%
100 µm 267 X 10.00 kV WD = 13 mm 1 May 2017
9 pA Tilt Angle = 0.0 ° 57.48 Hours
Cl 91.9%
Br 8.1%
Cl 90.7%
Br 9.3%
Cl 86.3%
Br 13.7%
200 µm 67 X 10.00 kV WD = 9 mm 2 May 2017
9 pA Tilt Angle = 0.0 ° 60.29 Hours
Cl 75.9%
Br 24.1%
Cl 75.7%
Br 24.3%
100 µm 132 X 10.00 kV WD = 14 mm 2 May 2017
9 pA Tilt Angle = 0.0 ° 60.77 Hours
Cl 67.5%
Br 32.5%
Cl 71.8%
Br 28.2%
Cl 73.2%
Br 26.8%
Cl 67.7%
Br 32.3%
100 µm 116 X 10.00 kV WD = 13 mm 1 May 2017
9 pA Tilt Angle = 0.0 ° 57.82 Hours
Cl 60.1%
Br 39.9%
Cl 56.1%
Br 43.9%
100 µm 122 X 10.00 kV WD = 14 mm 2 May 2017
9 pA Tilt Angle = 0.0 ° 61.01 Hours
Cl 30.8%
Br 69.2%
Cl 25.7%
Br 74.3%
200 µm 58 X 10.00 kV WD = 14 mm 2 May 2017
9 pA Tilt Angle = 0.0 ° 61.22 Hours
Cl 21.1%
Br 78.9%
Cl 21.7%
Br 78.3%
Cl 14.2%
Br 85.8%
200 µm 71 X 10.00 kV WD = 14 mm 1 May 2017
9 pA Tilt Angle = 0.0 ° 58.08 Hours
Cl 15.0%
Br 85.0%
Cl 12.9%
Br 87.1%
Cl 19.4%
Br 80.6%
100 µm 82 X 10.00 kV WD = 14 mm 2 May 2017
9 pA Tilt Angle = 0.0 ° 61.39 Hours
Cl 7.0%
Br 93.0%
Cl 6.9%
Br 93.1%
200 µm 67 X 10.00 kV WD = 14 mm 2 May 2017
9 pA Tilt Angle = 0.0 ° 61.59 Hours
Cl 0.4%
Br 99.4%
Cl 0.0%
Br 100.0%
Cl 0.3%
Br 99.7%
100 µm 134 X 10.00 kV WD = 13 mm 1 May 2017
9 pA Tilt Angle = 0.0 ° 58.30 Hours

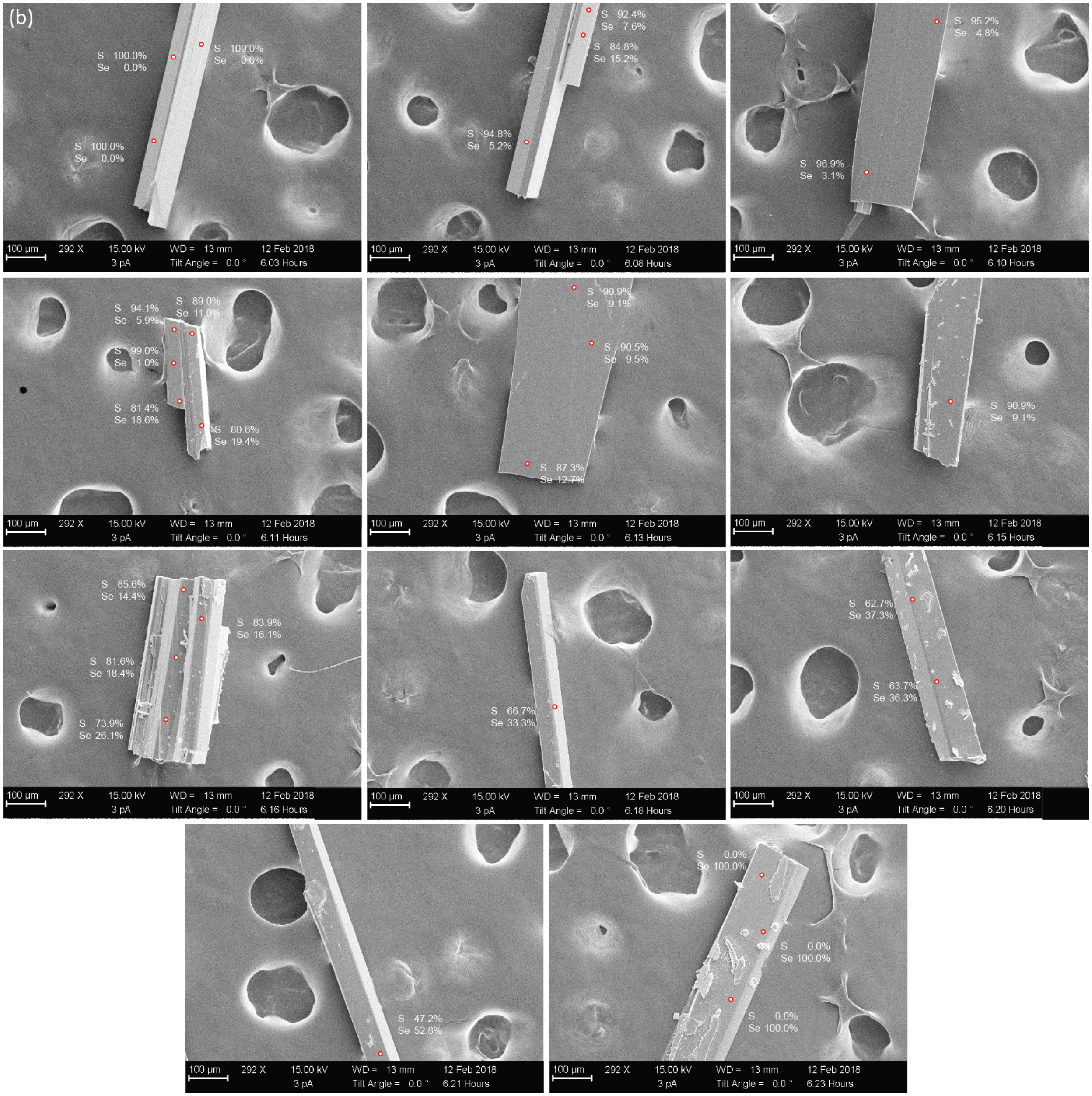

Figure 5.7. Elemental Characterization Data for Ternary Solid Solutions

(a) SEM secondary electron (SE) images of ternary DMDBT$_1$DDQ$_Y$DBQ$_{(1-Y)}$ single crystals. Energy dispersive spectra were collected from the points shown as white and red dots with the Cl and Br atomic ratios given for each point. (b) SEM SE images of ternary DMDBT$_X$DMDBS$_{(1-X)}$DBQ$_1$ single crystals. Energy dispersive spectra were collected from the points shown as white and red dots with the calibrated S and Se atomic ratios given for each point.

Figure 5.8a summarizes the EDS measurements, highlighting the continuous changes in the DDQ/DBQ molar ratio that can be achieved when crystallized with DMDBT. Additionally, changes in composition are linearly dependent on the feed ratio when crystallized by evaporation. $DMDBT_1DDQ_YDBQ_{(1-Y)}$, however, excludes DMDBS at low DMDBT/DMDBS feed ratios, as shown in Figure 5.8b. This exclusion is likely due to lattice strain caused by the increase in size of DMDBS relative to DMDBT, which disfavors the inclusion of DMDBS.

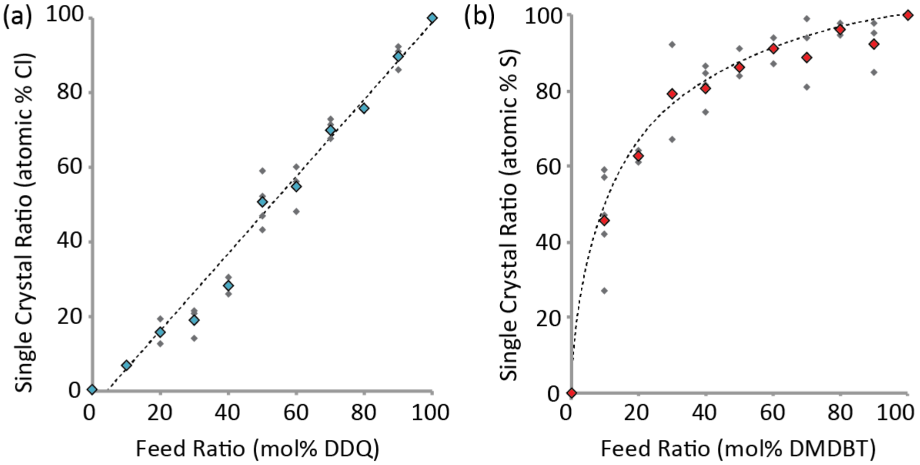

Figure 5.8. Feed Ratio and Composition

(a) Relationship between the DDQ feed ratio (relative to DBQ) and atomic % Cl measured from single crystals of $DMDBT_1DDQ_YDBQ_{(1-Y)}$ by SEM-EDS; (b) relationship between the DMDBT feed ratio (relative to DMDBS) and atomic % S measured from single crystals of $DMDBT_XDMDBS_{(1-X)}DBQ_1$ by SEM-EDS.

Single crystals of $DMDBT_1DDQ_YDBQ_{(1-Y)}$ were indexed by SCXRD, revealing a linear volumetric increase with increasing DBQ content. Unit cell indexing was repeated for the $DMDBT_XDMDBS_{(1-X)}DBQ_1$ solid solution, showing a similar linear relationship between composition and cell volume (see Figure 5.9 and Table 5.2). These correlations provide a method by which to calculate the DDQ/DBQ ratio of a sample when crystallized with DMDBT or the DMDBT/DMDBS ratio with DBQ in the absence of elemental information.

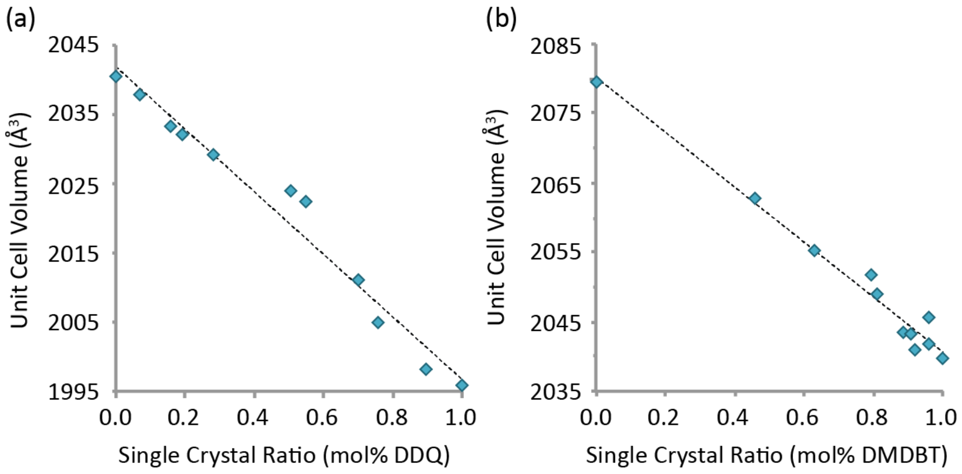

Figure 5.9. Composition and Unit Cell Volume

Cell volumes (determined by single crystal X-ray diffraction) plotted against the average (a) DDQ/DBQ and (b) DMDBT/DMDBS single crystal ratio determined by SEM-EDS.

Table 5.2. Composition and Unit Cell Parameters

mol% DDQ	*a* (Å)	*b* (Å)	*c* (Å)	Vol (Å^3)
100.0%	6.5775	18.3720	15.5159	1995.8
89.6%	6.5881	18.3326	16.5455	1998.3
75.8%	6.5713	18.4055	16.5779	2005.1
70.1%	6.6003	18.3301	16.6231	2011.1
54.8%	6.6032	18.3706	16.6720	2022.4
50.7%	6.6196	18.3041	16.7052	2024.1
28.3%	6.6181	18.3113	16.7450	2029.3
19.0%	6.6189	18.3333	16.7463	2032.1
15.8%	6.6190	18.3313	16.7592	2033.5
7.0%	6.6270	18.3093	16.7949	2037.8
0.0%	6.6106	18.3390	16.8316	2040.5
mol% DMDBT				
100%	6.6092	18.3407	16.8277	2039.8
96%	6.6115	18.34456	16.83467	2041.8
89%	6.6123	18.3498	16.8418	2043.5
81%	6.61734	18.3662	16.8595	2049.0
79%	6.6230	18.3661	16.8663	2051.6
63%	6.62445	18.3804	16.8785	2055.1
46%	6.63194	18.4005	16.90572	2063.0
0%	6.64274	18.4437	16.9726	2079.4

The crystallization of quaternary cocrystals was also explored, despite the non-isostructurality of the DMDBS-DDQ phase relative to the ternary solid solutions. Because multiple chemical compositions of the solid solution can exhibit the same cell volume, indexing single crystals by XRD could not be used to calculate the Cl/Br and S/Se ratios. Raman microscopy was instead used to determine the compositional ratios in single crystals of the quaternary DMDBT$_{X}$DMDBS$_{(1-X)}$DDQ$_{Y}$DBQ$_{(1-Y)}$ solid solution (see Figure 5.10). Using this method, the compositions of single crystals were determined, confirming that a quaternary solid solution was successfully produced even when the binary cocrystals are not all isostructural.

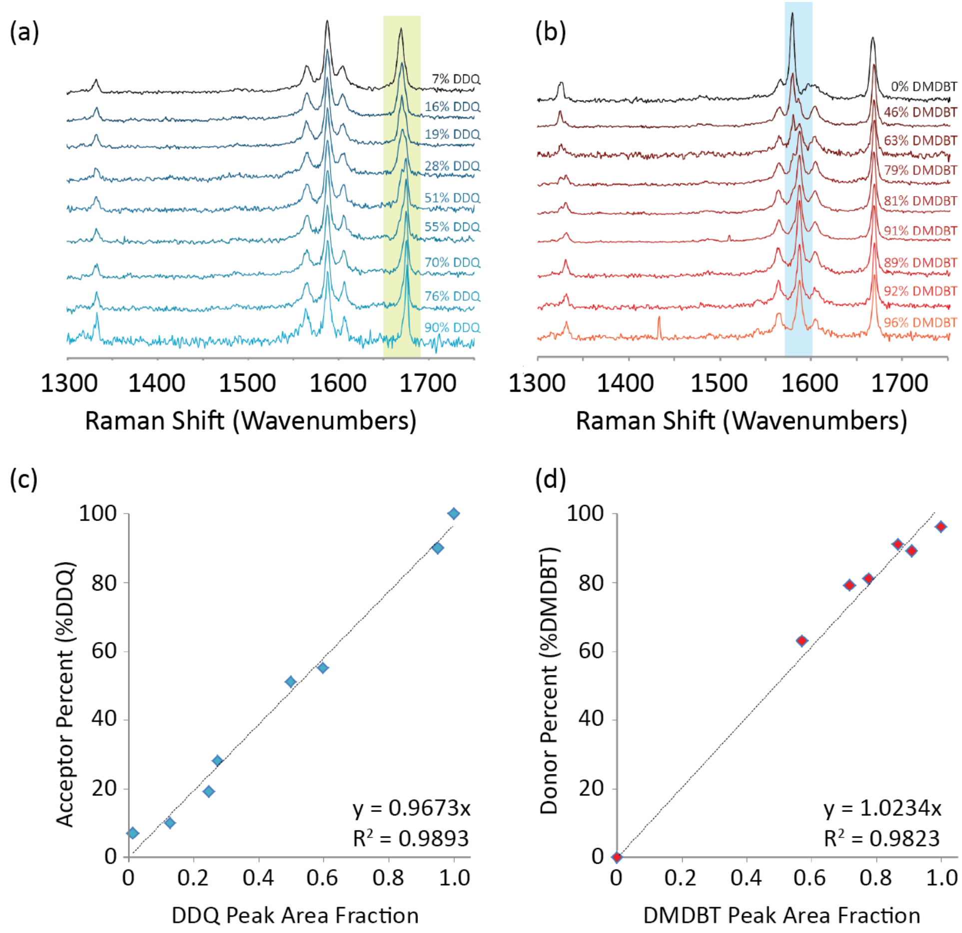

Figure 5.10. Raman Spectra for Ternary Solid Solutions

(a) Ternary DMDBT$_1$DDQ$_Y$DBQ$_{(1-Y)}$ solid solution Raman spectra used for calibration of the DDQ/DBQ ratio. The relative peak intensities for two components fitted in the highlighted region were analyzed. (b) Ternary DMDBT$_X$DMDBS$_{(1-X)}$DBQ$_1$ solid solution Raman spectra used for calibration of the DMDBT/DMDBS ratio. The relative peak intensities for the two components fitted in the highlighted region were analyzed. Relative (c) DDQ/DBQ and (d) DMDBT/DMDBS peak area calibration curves.

Figure 5.11 summarizes compositions measured from the quaternary crystals, mapping out a stability field for the solid solution phase and showing that quaternary crystals that are simultaneously enriched in both DDQ and DMDBS could not be produced. This region of solid solution instability is expected due to the co-precipitation of the DMDBS-DDQ cocrystal. Figure 5.11 also shows the cell volumes for each of the indexed solid solution compositions.

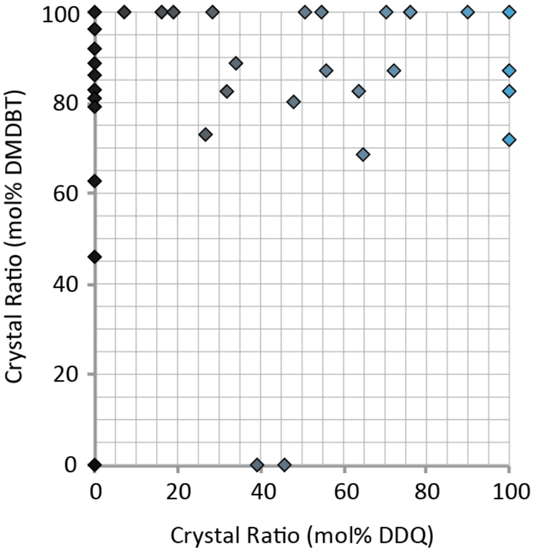

Figure 5.11. Quaternary Solid Solution Stability Field

Measured compositions from single crystals of quaternary $\mathrm{DMDBT}_X\mathrm{DMDBS}_{(1\text{-}X)}\mathrm{DDQ}_Y\mathrm{DBQ}_{(1\text{-}Y)}$ measured by Raman spectroscopy, referred to as the solid solution stability field.

5.2.4 Ionicity in CT Solid Solutions

The ionicity, or degree of charge transfer (ρ), is a parameter that describes the amount of electron density transferred between donor and acceptor molecules in CT complexes.[11, 22, 27] This value is related to the electronic properties associated with a CT system, such as dielectricity, semiconductivity, and conductivity.[11] In CT complexes containing DDQ, infrared (IR) spectroscopy has been used to measure the vibrational frequency of nitrile groups (Figure 5.12a,b)[22, 30] compared to those of neutral, DD(B)Q, and radical anion, DD(B)Q$^-$, standards using the following equation:[31]

$$\rho_v = 2(v_0 - v_{\mathrm{CT}}) / v_0(1 - v_1^2 / v_0^2)^{-1}$$

in which ρ_v is the degree of CT measured from vibrational spectra and v_0, v_{CT}, and v_1 are the symmetrical -CN stretching frequencies in the neutral standard, CT sample, and radical anion standard, respectively. Using this method, the degree of charge transferred to DD(B)Q was calculated across the DMDBT$_1$DDQ$_Y$DBQ$_{(1-Y)}$ and DMDBT$_X$DMDBS$_{(1-X)}$DBQ$_1$ ternary solid solutions. The DMDBT$_1$DDQ$_Y$DBQ$_{(1-Y)}$ ternary solid solution is characterized by a continuous decrease in ρ_v value from 0.19(2) e for DMDBT-DBQ to 0.005(4) e for DMDBT-DDQ (see Figure 5.12c), while the decrease in ρ_v value from DMDBT-DBQ to DMDBS-DBQ, 0.08(2) e, is less well defined due to uncertainty in the DMDBT/DMDBS molar ratios.

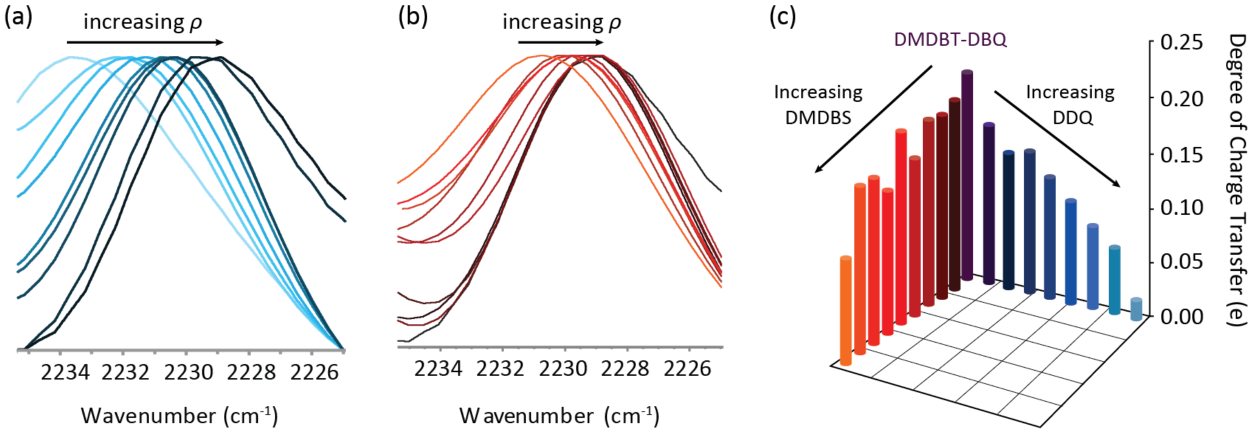

Figure 5.12. IR Spectra and Degree of CT

(a) IR spectra of the asymmetric nitrile stretch for DMDBT-DDQ (light blue), DMDBT-DBQ (black), and ternary solid solution DMDBT$_1$DDQ$_Y$DBQ$_{(1-Y)}$ samples (intermediate colors). (b) IR spectra of the asymmetric nitrile stretch for DMDBT-DBQ (orange), DMDBS-DBQ (black), and ternary solid solution DMDBT$_X$DMDBS$_{(1-X)}$DBQ$_1$ samples (intermediate colors). (c) 3D bar graph showing the dependent of ρ_v on composition with the DMDBT-DBQ cocrystal (purple) showing the largest ρ_v value.

Given that the stretching frequency of the -CN functionality is unreliable[22, 32] due to halogen bonding interactions, ρ values for the three isostructural cocrystals were also calculated from the geometries of the acceptors measured from the single-crystal X-ray structures (ρ_α). We have implemented the method proposed by Kistenmacher *et al.*,[33] originally designed for 2,2,3,3-tetracyanoquinodimethane (TCNQ), and have adapted it for DDQ and DBQ:

$$\rho_\alpha = (\alpha_{\mathrm{CT}} - \alpha_0) / (\alpha_1 - \alpha_0)$$

wherein $\alpha = a / (b + c)$, the ratio of the average C=C to C-C bond lengths as defined in Figure 5.13. Using this method, the ρ_α values for DMDBT-DDQ, DMDBT-DBQ, and DMDBS-DBQ were calculated at 0.11(1), 0.50(1), and 0.30(1) e, respectively (see Figure 5.13), yielding the same relative ranking in ρ_α as ρ_v between the three cocrystals, suggesting that a range of electronic properties, namely dielectricity and semiconductivity, can be achieved through compositional variation. The ionicities derived from geometric measurements from the crystal structures likely yields more accurate results because the measured bonds are not directly interacting through hydrogen or halogen bonds. That said, it was noted that the ranking in the relative ionicities of the binary cocrystals does not follow what would be predicted by conventional models of charge-transfer, which correlate ρ of the *DA* complex with the difference in oxidation and reduction potentials of the *D* and *A* molecules.[22,34] Work is ongoing to further investigate the ranking in ionicity exhibited by these cocrystals.

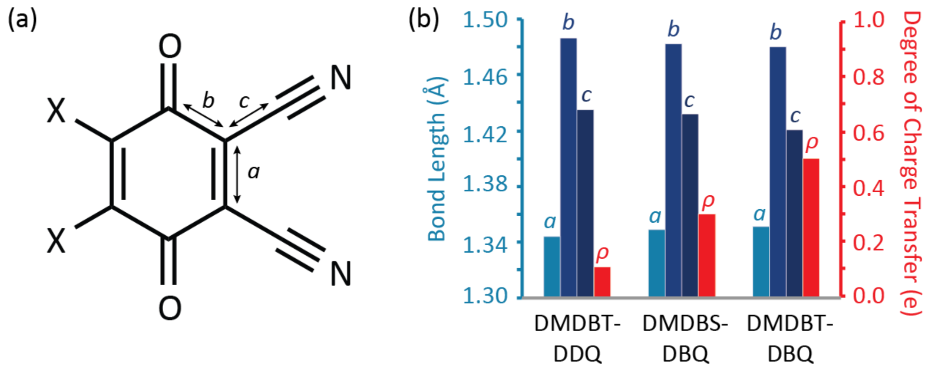

Figure 5.13. Geometric Determination of CT

(a) Structural definition of parameters a, b, and c for measurement of ρ_α. (b) Graphs of a, b, c, and ρ_α measured from the crystal structures of DMDBT-DDQ (0.11 e), DMDBS-DBQ (0.30 e), and DMDBT-DBQ (0.50 e).

5.2.5 The Optical Band Gap in CT Solid Solutions

The broad range of ρ values measured from the DMDBT$_1$DDQ$_Y$DBQ$_{(1-Y)}$ solid solution, motivated determination of the optical band gaps (E_{opt}) for this compositional range. Diffuse reflectance spectra of the ternary DMDBT$_1$DDQ$_Y$DBQ$_{(1-Y)}$ solid solution were collected for various DDQ/DBQ ratios (see Figure 5.14) and, from these spectra, E_{opt} was calculated. DMDBT-DDQ was found to have the lowest E_{opt}, at 1.26(1) eV, while compositions between DMDBT$_1$DDQ$_{0.9}$DBQ$_{0.1}$ and DMDBT-DBQ were measured at 1.38(1) eV. The trend in E_{opt} is consistent with that of the measured ρ values; increases in the degree of charge transfer lead to a lowering in energy of the valence band and a raising in energy of the conduction band, widening the optical band gap. These results indicate that the ternary solid solution should outperform both binary end members DMDBT-DDQ and DMDBT-DBQ at high DDQ:DBQ ratios as a semiconductor by balancing the effects of increasing ρ and decreasing E_{opt}.

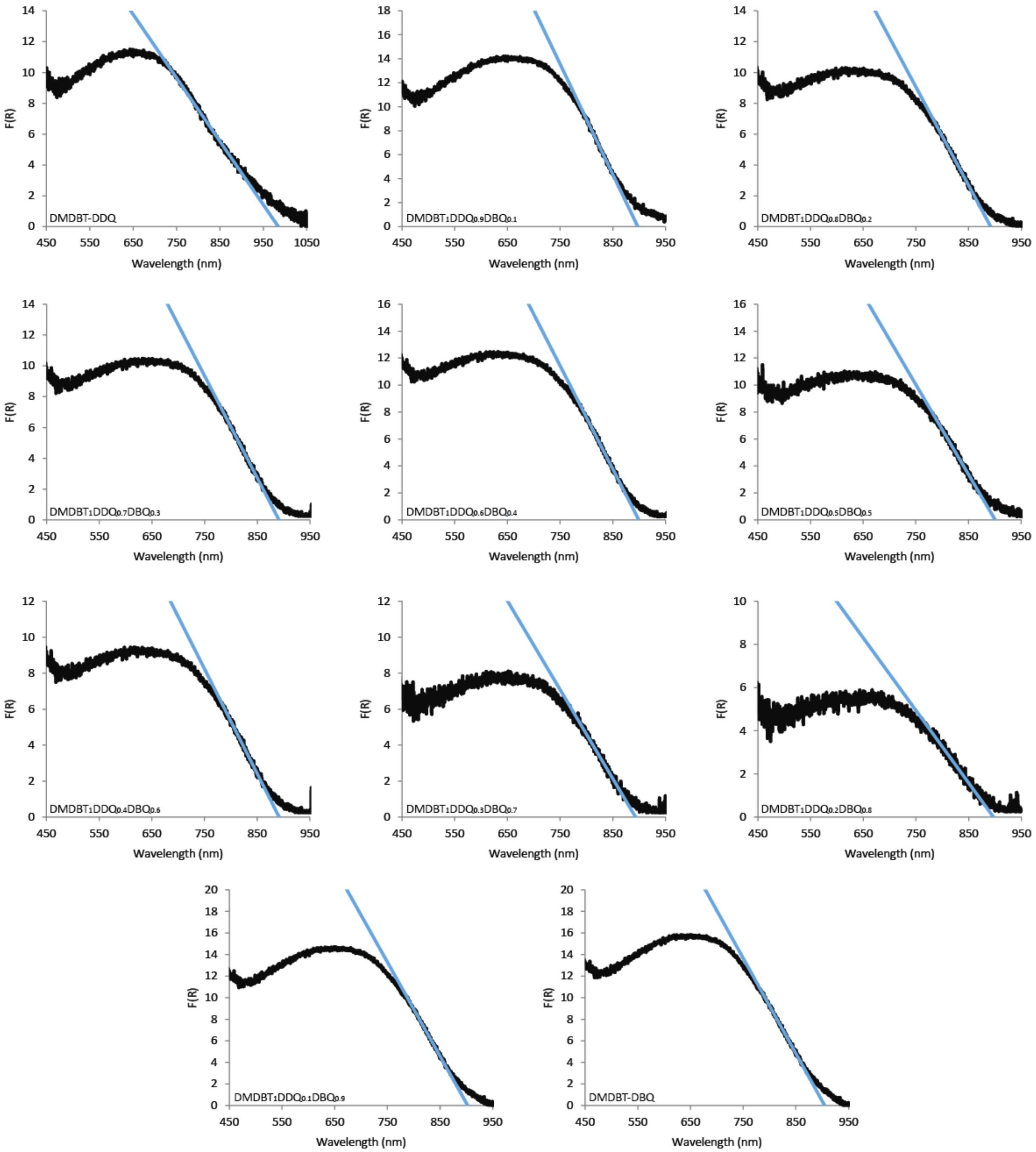

Figure 5.14. Diffuse Reflectance Spectra for DMDBT$_1$DDQ$_Y$DBQ$_{(1-Y)}$

Diffuse reflectance spectra of the ternary DMDBT$_1$DDQ$_Y$DBQ$_{(1-Y)}$ solid solutions.

5.2.6 Compositional Zoning in CT Solid Solutions

Having demonstrated that CT solid solution formation can be used to tune both the ρ and E_{opt}, we turned our attention to the possibility of using the isostructural relationship among these electronically distinct phases to synthesize single crystals containing defined domains of predicted dielectric or semiconductive character. Preparing single crystals with domains of variable electronic character introduces an approach to reduce contact resistance between organic semiconductors and inorganic electrodes in field effect transistors. An analogous approach, in which F_4TCNQ is deposited onto small molecule semiconductors, has been shown to reduce contact resistance between p-type semiconductors and inorganic contacts.[35,36] By producing single crystals with well-defined domains of enhanced conductivity, the electronic contact is predicted to further improve. This concept was explored using the $DMDBT_1DDQ_YDBQ_{(1-Y)}$ system by controlling the DDQ/DBQ feed ratio during different stages of crystallization to produce core-shell structures within single crystals. SEM-EDS mapping was used to visualize the domains enriched in DDQ and/or DBQ by measuring the Cl/Br relative atomic percentages. DMDBT-DBQ crystals were grown by evaporation to produce large single crystals. These crystals were then placed in a solution of DMDBT and DDQ and cooled overnight to produce a shell of DMDBT-DBQ. This process was repeated to produce DMDBT-DDQ-enriched cores with DMDBT-DBQ enriched-shells. Figures 5.15a and 5.15b show secondary electron (SE) images and EDS compositional maps of the cut faces of these two materials, revealing the core-shell structure of the single crystals.

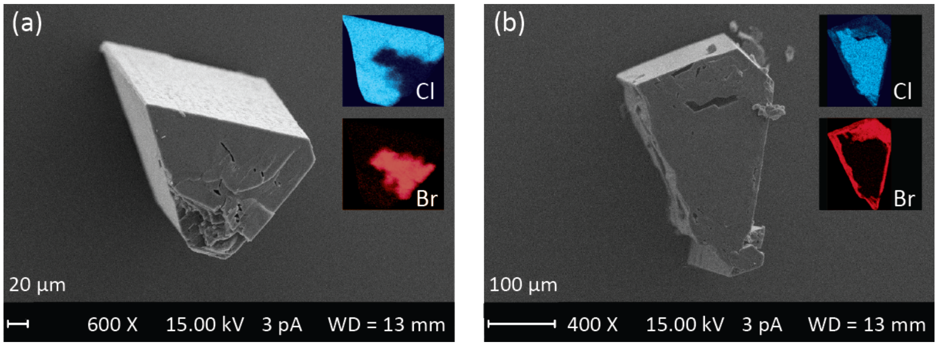

Figure 5.15. SEM SE and EDS Map Images for Zoned Crystals

(a) SEM image (grey scale) of the cut face of the DMDBT-DBQ core and DMDBT-DDQ shell crystal with EDS maps of Cl (blue) and Br (red) enriched regions shown in the upper right of the SEM image; (b) SEM image of the cut face of the DMDBT-DDQ core and DMDBT-DBQ shell crystal with EDS maps of the Cl and Br enriched regions shown in the upper right of the SEM image.

5.3 Conclusion

Substitutional doping and solid solution formation offer the opportunity to tune the electronic performance of materials without the unpredictability associated with changes in crystal packing. We have shown that this method is not restricted to inorganics but can be extended to organic CT cocrystals that show isomorphous crystal packing, such as those formed between DMDBT, DMDBS, DDQ, and DBQ, to achieve improved performance relative to the end member cocrystals. The potential for this approach to yield optimized materials is exemplified by the $\mathrm{DMDBT_1DDQ_{\mathit{Y}}DBQ_{(1-\mathit{Y})}}$ solid solution, which is predicted to outperform the binary end members as a semiconductor because a balance between increased ρ and lowered E_{opt} can be achieved through intermediate DDQ/DBQ molar ratios. Additionally, we have shown that the isomorphous relationship between the DMDBT-DDQ and DMDBT-DBQ cocrystals can be exploited to construct single crystals containing core-shell domains enriched in either DMDBT-DDQ or DMDBT-DBQ; such compositional architectures complement existing approaches for reducing contact resistance between organic semiconductors and inorganic contacts.

5.4 Experimental Methods

All reagents were used as received from manufacturers without additional purification. 2,3-dicyano-1,4-hydroquinone (98%), *N*-bromosuccinimide (98%), *o*-iodotoluene (98%), CuI (98%), K_3PO_4 (97%), $Pd^{II}(tfa)_2$ (97%), pivalic acid (99%), and 4,6-dimethyldibenzothiophene (95%) were obtained from Acros Organics. *tert*-Butanol, HNO_3 (certified ACS Plus), and anhydrous K_2CO_3 (certified ACS) were obtained from Fisher Scientific. PEG_{500} was obtained from Hoechst AG, AgOAc (99%) was obtained from Alfa Products, and 2,3-dichloro-5,6-dicyanobenzoquinone (98%) was obtained from Sigma Aldrich.

5.4.1 Synthesis of 2,3-dibromo-5,6-dicyano-1,4-benzoquinone (DBQ)

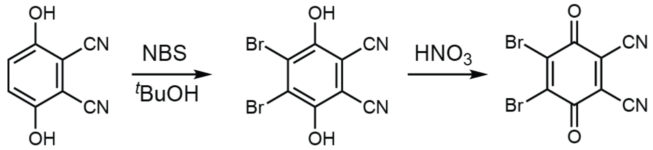

Synthesis of 2,3-dibromo-5,6-dicyano-1,4-benzoquinone (DBQ) was adapted from the literature.[37] The precursor, 2,3-dibromo-5,6-dicyano-1,4-hydroquinone, was synthesized by reacting 2,3-dicyanohydroquinone (750.5mg, 4.687 mmol) with *N*-bromosuccinimide (3390. mg, 19.04 mmol) in 5 mL *tert*-butanol at 40 °C for 3 hours, during which time a bright red suspension formed. The reaction solution was quenched with 0.5M $NaHSO_3$, precipitating the product as a light-yellow solid (706.4 mg, 2.222 mmol, 47% yield). The 2,3-dibromo-5,6-dicyano-1,4-hydroquinone (706.4 mg, 2.222 mmol) was heated to reflux in 7 mL concentrated HNO_3 for 2.5 hours. The product was precipitated by adding 20 mL of ice water and isolated by vacuum filtration (465.2 mg, 1.473 mmol, 66% yield).

5.4.2 Synthesis of 4,6-dimethyldibenzoselenophene (DMDBS)

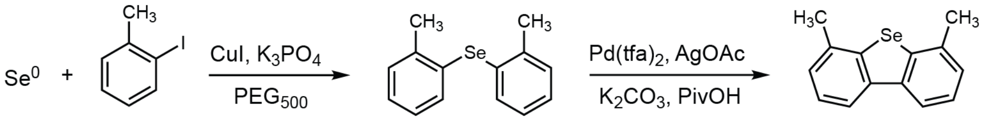

The synthesis of 4,6-dimethyldibenzoselenophene (DMDBS) proceeds smoothly through the intramolecular oxidative coupling of the di(*o*-methylphenyl) selane intermediate adapted from the literature[38]. The selane intermediate was synthesized by reacting Se^0 powder (312.5 mg, 3.958 mmol) with *o*-iodotoluene (1734. mg, 7.955 mmol) in N_2-sparged PEG_{500} (8 mL) in the presence of CuI (83.75 mg, 0.4397 mmol) and tribasic K_3PO_4 (3984. mg, 18.77 mmol) in a sealed pressure vessel. The vessel was heated to 90 °C for one hour immediately followed by 24 hours at 110 °C. The crude product was extracted into petroleum ether and dried over anhydrous $MgSO_4$. The selane intermediate (colorless) was purified by column chromatography on silica gel using a 0-2.5 (v/v)% DCM:hexanes solvent gradient (301.3 mg, 1.153 mmol, 29%). ^{1}H NMR data are consistent with literature[39] and the structure confirmed by single-crystal X-ray diffraction. The intramolecular oxidative coupling of the selane intermediate (301.3 mg, 1.153 mmol) was catalyzed by $Pd(tfa)_2$ (40.29 mg, 0.120 mmol) in the presence of AgOAc (773.1 mg, 4.632 mmol), K_2CO_3 (160.1 mg, 1.159 mmol) and pivalic acid (2185. mg, 21.40 mmol) in a 20 mL vial with a Teflon-lined screw cap. After all reactants were added, the reaction mixture was heated to 90 °C open to atmosphere for five minutes then sealed and heated to 120 °C for 16 hours. The reaction contents were suspended in DCM and filtered through a Celite pad. The DCM solution was then washed with $NaHCO_3$ and brine and dried over anhydrous $MgSO_4$. DMDBS was purified by column chromatography on silica gel using a 0-5% (v/v) DCM:hexanes solvent gradient (105.1 mg, 0.4056 mmol, 35%). ^{1}H NMR (400 MHz, acetone-d_6) δ 8.11 (d, 2H), 7.45 (t, 2H), 7.31 (d, 2H), 2.79 (s, 6H).

5.4.3 Crystallization

Single crystals of variable DDQ/DBQ molar ratios were prepared by mixing DDQ, DBQ, and DMDBT stock solutions. The DDQ stock was prepared by dissolving DDQ (5.62 mg, 2.476×10^{-2} mmol) in 2.75 mL acetonitrile. The DBQ stock was prepared by dissolving DBQ (7.85 mg, 2.492×10^{-2} mmol) in 2.75 mL acetonitrile. The DMDBT stock was prepared by dissolving DMDBT (10.53 mg, 4.960×10^{-2} mmol) in 2.20 mL acetonitrile. Between 0-500 μL of the DDQ and/or DBQ stock solutions were transferred to polypropylene Eppendorf tubes and the solution of acceptors mixed by sonication followed by addition of 200 μL of the DMDBT stock solution. This protocol was also used to produce single crystals of variable DMDBT/DMDBS content with DBQ and to form the quaternary solid solution single crystals upon evaporation.

5.4.4 Single-Crystal X-Ray Diffraction

Single-crystal X-ray diffraction data were collected using a Rigaku XtaLAB Synergy-S X-ray diffractometer configured in a kappa goniometer geometry. The diffractometer is equipped with a low temperature device and a PhotonJet-S microfocus Cu source (λ = 1.54187 Å) and operated at 50 kV and 1 mA. X-ray intensities were measured at 100 K or room temperature with the HyPix-6000HE detector placed 32.01 mm from the sample. The data were processed with CrysAlisPro v38.46 (Rigaku Oxford Diffraction) and corrected for absorption. The structures were solved in OLEX2[40] using SHELXT[41] and refined using SHELXL[42]. All non-hydrogen atoms were refined anisotropically with hydrogen atoms placed at idealized positions. Single crystals were mounted on a 150 μm MiTeGen MicroMount using mineral oil. Room temperature (298 K) cell parameters for single crystals of $\mathrm{DMDBT}_{X}\mathrm{DMDBS}_{(1-X)}\mathrm{DBQ}_{1}$ and $\mathrm{DMDBT}_{X}\mathrm{DMDBS}_{(1-X)}\mathrm{DDQ}_{Y}\mathrm{DBQ}_{(1-Y)}$ were collected on the Synergy-S, while cell parameters for

DMDBT$_{1}$DDQ$_{Y}$DBQ$_{(1-Y)}$ were collected on a Rigaku R-Axis Spider diffractometer using Cu-Kα radiation (λ = 1.54187 Å) and operating at 40 kV and 44 mA. Images were collected from 20 to 197.5° at a 2.5° width and a 12.5° ω step size and each image was exposed for 30 seconds. The χ- and ϕ-axes were held fixed at 0.0°. The images were indexed using Rigaku CrystalClear-SM Expert 2.0 r15 software.

5.4.5 Scanning Electron Microscopy

The samples were gold-coated in preparation for secondary electron (SE) imaging and elemental analysis by energy dispersive spectroscopy (EDS). Scanning electron microscope SE (SEM-SE) images were collected using a Zeiss LEO 1455VP microscope fitted with an Oxford x-act silicon drift EDS detector (SDD) operated through SmartSEM (Zeiss). Images were taken at accelerating voltages between 10-15 kV and a probe current of 3.0 pA. EDS spectra and elemental maps were collected at a probe current of 24.5 nA, optimizing for detector dead time, operated through AZtecEnergy Software (Oxford).

5.4.6 Raman Microscopy

Raman spectra were collected using a Renishaw inVia Raman Microscope equipped with a Leica microscope, 633 nm laser, 1800 lines/mm grating, 50 µm slit and a RenCam CCD detector. Spectra were collected in static mode centered about 1500 cm^{-1} and analyzed using the WiRE 3.4 software package (Renishaw) and OriginPro 8.6. Calibration was performed using a silicon standard in static mode.

5.4.7 Infrared Spectroscopy

Infrared spectra were recorded on a Thermo Nicolet Avatar 360 FT-IR instrument in ATR mode using a germanium window (SpectraTech). The sample cabinet was purged with N_2 to minimize background from atmospheric absorption. The reflectance was scanned over a range of 800-3800 cm^{-1}. The spectra were collected and the default Ge ATR correction applied in EZ OMNIC 2.11 (Thermo Fisher Scientific) and analyzed in ACD/Spectrus Processor 2014.

5.4.8 Diffuse Reflectance Visible Spectroscopy

Diffuse reflectance spectra were collected on using an Ocean Optics 45º DR-Probe with an integrated tungsten light source connected to a Maya2000 Pro spectrometer. Spectra were controlled using Ocean View v1.6.7 with an 8 ms integration time and 100 scan averaging. Samples were ground and diluted with $BaSO_4$, which was also used as the 100% reflectance standard.

5.4.9 Calculations

The effective couplings between donor molecules and acceptor molecules along the stacking direction were obtained using the energy-splitting approach by considering the energy levels of D-A-D or A-D-A triads.[43] These calculations were performed with the B3LYP functional and the 6-31G(d,p) basis set, using the Gaussian 09 package.[44] The electronic band-structure calculations of DMDBT-DDQ, DMDBT-DBQ and DMDBS-DBQ were performed at the experimental crystal geometry using the B3LYP functional and the 6-31G basis set. The Brillouin zone was sampled using an 8 x 4 x 4 Monkhorst−Pack k-point mesh for all cocrystals. These calculations were carried out using the CRYSTAL14 package.[45,46]

5.5 References

1. Burroughes, J. H.; Jones, C. A.; Friend, R. H., New semiconductor device physics in polymer diodes and transistors. *Nature* **1988,** *335*, 137-141.
2. Tsutsumi, J. y.; Matsuoka, S.; Inoue, S.; Minemawari, H.; Yamada, T.; Hasegawa, T., *N*-type field-effect transistors based on layered crystalline donor-acceptor semiconductors with dialkylated benzothienobenzothiophenes as electron donors. *J. Mater. Chem. C* **2015,** *3*, 1976-1981.
3. Higashino, T.; Dogishi, M.; Kadoya, T.; Sato, R.; Kawamoto, T.; Mori, T., Air-stable n-channel organic field-effect transistors based on charge-transfer complexes including dimethoxybenzothienobenzothiophene and tetracyanoquinodimethane derivatives. *J. Mater. Chem. C* **2016,** *4*, 5981-5987.
4. Sato, R.; Dogishi, M.; Higashino, T.; Kadoya, T.; Kawamoto, T.; Mori, T., Charge-Transfer Complexes of Benzothienobenzothiophene with Tetracyanoquinodimethane and the n-Channel Organic Field Effect Transistors. *J. Phys. Chem. C* **2017,** *121*, 6561-6568.
5. Burroughes, J. H.; Bradley, D. D. C.; Brown, A. R.; Marks, R. N.; Mackay, K.; Friend, R. H.; Burns, P. L.; Holmes, A. B., Light-emitting diodes based on conjugated polymers. *Nature* **1990,** *347*, 539-541.
6. Greenham, N. C.; Moratti, S. C.; Bradley, D. D. C.; Friend, R. H.; Holmes, A. B., Efficient light-emitting diodes based on polymers with high electron densities. *Nature* **1993,** *365*, 628-630.
7. Su, Y.-W.; Lan, S.-C.; Wei, K.-H., Organic phtovoltaics. *Mater. Today* **2012,** *15*, 554-562.
8. Kaur, N.; Singh, M.; Pathak, D.; Wagner, T.; Nunzi, J. M., Organic materials for photovoltaic application: Review and mechanism. *Synth. Met.* **2014,** *190*, 20-26.
9. Hu, P.; Li, H.; Li, Y.; Jiang, H.; Kloc, C., Single-crystal growth, structures, charge transfer and transport properties of anthracene-F_4TCNQ and tetracene-F_4TCNQ charge-transfer compounds. *CrystEngComm* **2017,** *19*, 618-624.
10. Anthony, J. E., The Larger Acenes: Versatile Organic Semiconductors. *Angew. Chem. Int. Ed.* **2008,** *47*, 452-483.
11. Goetz, K. P.; Derek; Vermeulen; Payne, M. E.; Kloc, C.; McNeil, L. E.; Jurchescu, O. D., Charge-transfer complexes: new perspectives on an old class of compounds. *J. Mater. Chem. C* **2014,** *2*.
12. Zhu, L.; Yi, Y.; Li, Y.; Kim, E.-G.; Coropceanu, V.; Brédas, J.-L., Prediction of Remarkable Ambipolar Charge-Transport Characteristics in Organic Mixed-Stack Charge-Transfer Crystals. *J. Am. Chem. Soc.* **2012,** *134*, 2340-2347.
13. Lutz, J. P.; Hannigan, M. D.; McNeil, A. J., Polymers synthesized via catalyst-transfer polymerization and their applications. *Coord. Chem. Rev.* **2018,** *376*, 225-247.
14. McGarry, K. A.; Xie, W.; Sutton, C.; Risko, C.; Wu, Y.; Young, V. G.; Brédas, J.-L.; Frisbie, C. D.; Douglas, C. J., Rubrene-Based Single-Crystal Organic Semiconductors: Synthesis, Electronic Structure, and Charge-Transport Properties. *Chem. Mater.* **2013,** *25*, 2254-2263.
15. Podzorov, V.; Menard, E.; Borissov, A.; Kiryukhin, V.; Rogers, J. A.; Gershenson, M. E., Intrinsic Charge Transport on the Surface of Organic Semiconductors. *Phys. Rev. Lett.* **2004,** *93*, 0866021-0866024.
16. Zhu, L.; Yi, Y.; Fonari, A.; Corbin, N. S.; Coropceanu, V.; Brédas, J.-L., Electronic Properties of Mixed-Stack Organic Charge-Transfer Crystals. *J. Phys. Chem. C* **2014,** *118*, 14150-14156.

17. Kitamura, M.; Arakawa, Y., Pentacene-based organic field-effect transistors. *J. Phys. Condens. Matter* **2008,** *20*, 1-16.
18. Sánchez-Carrera, R. S.; Paramonov, P.; Day, G. M.; Coropceanu, V.; Brédas, J.-L., Interaction of Charge Carriers with Lattice Vibrations in Oligoacene Crystals from Naphthalene to Pentacene. *J. Am. Chem. Soc.* **2010,** *132*, 14437-14446.
19. Rovira, C., Bis(ethylenethio)tetrathiafulvalene (BET-TTF) and Related Dissymmetrical Electron Donors: From the Molecule to Functional Molecular Materials and Devices (OFETs). *Chem. Rev.* **2004,** *104*, 5289-5317.
20. Zhen, Y.; Tanaka, H.; Harano, K.; Okada, S.; Matsuo, Y.; Nakamura, E., Organic Solid Solution Composed of Two Structurally Similar Porphyrins for Organic Solar Cells. *J. Am. Chem. Soc.* **2015,** *137*, 2247-2252.
21. Nanova, D.; Beck, S.; Milan; Alt; Glaser, T.; Pucci, A.; Schulteiß, K.; Dieterle, L.; Schröder, R. R.; Pflaum, J.; Kowalsky, W.; Kroeger, M., Phase separation in ternary charge-transfer-complexes. *Appl. Phys. A* **2013,** *112*, 1019-1025.
22. Kampar, E.; Neilands, O., Degree of Charge Transfer in Donor-Acceptor Systems of the π-π Type. *Uspsekhi Khimii* **1986,** *55*, 637-651.
23. Castagnetti, N.; Masino, M.; Rizzoli, C.; Girlando, A.; Rovira, C., Mixed stack charge transfer crystals: Crossing the neutral-ionic borderline by chemical substitution. *Phys. Rev. Mater.* **2018,** *2*, 0246021-0246029.
24. Sada, K.; Inoue, K.; Tanaka, T.; Epergyes, A.; Tanaka, A.; Tohnai, N.; Matsumoto, A.; Miyata, M., Multicomponent Organic Alloys Based on Organic Layered Crystals. *Angew. Chem.* **2005,** *117*, 7221-7224.
25. Jalilov, A. S.; Lu, J.; Kochi, J. K., Charge-transfer complex cormations of tetracyanoquinone (cyanil) and aromatic electron donors. *J. Phys. Org. Chem.* **2016,** *29*, 35-41.
26. Bondi, A., van der Waals Volumes and Radii. *J. Phys. Chem.* **1964,** *68*, 441-451.
27. Goud, N. R.; Matzger, A. J., Impact of Hydrogen and Halogen Bonding Interactions on the Packing and Ionicity of Charge-Transfer Cocrystals. *Cryst. Growth Des.* **2017,** *17*, 328-336.
28. SPARTAN '16, Wavefunction, Inc., Irvine, CA, USA, 2013.
29. Goetz, K. P.; Tsutsumi, J. y.; Pookpanratana, S.; Chen, J.; Corbin, N. S.; Behera, R. K.; Coropceanu, V.; Richter, C. A.; Hacker, C. A.; Hasegawa, T.; Jurchescu, O. D., Polymorphism in the 1:1 Charge-Transfer Complex DBTTF-TCNQ and Its Effects on Optical and Electronic Properties. *Adv. Electron. Mater.* **2016,** *2*, 16002031-160020310.
30. Miller, J. S.; Krusic, P. J.; Dixon, D. A.; Reiff, W. M.; Zhang, J. H.; Anderson, E. C.; Epstein, A. J., Radical Ion Salts of 2,3-Dichloro-5,6-dicyanobenzoquinone and Metallocenes. A Reexamination of Their Magnetic and Spectroscopic Properties. *J. Am. Chem. Soc.* **1986,** *108*, 4459-4466.
31. Salmerón-Valverde, A.; Robles-Martínez, J. G.; García-Serrano, J.; Gómez, R.; Ridaura, R. M.; Quintana, M.; Zehe, A., A Study of the Degree of Charge Transfer in TTF Molecular Complexes with Nitro-Carboxylated Fluorene Derivatives. *Molec. Eng.* **1999,** *8*, 419-426.
32. Meneghetti, M.; Pecile, C., Charge-transfer organic crystals: Molecular vibrations and spectroscopic effects of electron-molecular vibration coupling of the strong electron acceptor TCNQF$_4$. *J. Chem. Phys.* **1986,** *84*, 4149-4162.
33. Kistenmacher, T. J.; Emge, T. J.; Bloch, A. N.; Cowan, D. O., Structure of the Red, Semiconducting Form of 4,4',5,5'-Tetramethyl-$\Delta^{2,2'}$-bi-1,3-diselenole-7,7,8,8-tetracyano-p-quinodimethane, TMTSF-TCNQ. *Acta Crystallogr.* **1982,** *B38*, 1193-1199.

34. Torrance, J. B.; Vazquez, J. E.; Mayerle, J. J.; Lee, V. Y., Discovery of a Neutral-to-Ionic Phase Transition in Organic Materials. *Phys. Rev. Lett.* **1981,** *46*, 253-257.
35. Abe, Y.; Hasegawa, T.; Takahashi, Y.; Yamada, T.; Tokura, Y., Control of threshold voltage in pentacene thin films using carrier doping at the charge-transfer interface with organic acceptors. *Appl. Phys. Lett.* **2005,** *87*, 1535061-1535063.
36. Vanoni, C.; Tsujino, S.; Jung, T. A., Reduction of the contact resistance by doping in pentacene few monolayers thin film transistors and self-assembled nanocrystals. *Appl. Phys. Lett.* **2007,** *90*, 1931191-1931193.
37. Wallenfels, K.; Bachmann, G.; Hofmann, D.; Kern, R., Cyansubstituierte chinone—II : 2,3-, 2,5- 2,6-dicyanchinone und tetracyanbenzochinon. *Tetrahedron* **1965,** *21*, 2239-2256.
38. Che, R.; Wu, Z.; Li, Z.; Xiang, H.; Zhou, X., Synthesis of Dibenzothiophenes by Pd-Catalyzed Dual C-H Activation from Diaryl Sulfides. *Chem. Eur. J.* **2014,** *20*, 7258-7261.
39. Taniguchi, N., Copper-catalyzed chalcogenation of aryl iodides via reduction of chalcogen elements by aluminum or magnesium. *Tetrahedron* **2012,** *68*, 10510-10515.
40. Dolomanov, O. V.; Bourhis, L. J.; Gildea, R. J.; Howard, J. K.; Puschmann, H., OLEX2: a complete structure solution, refinement and analysis program. *J. Appl. Cryst.* **2009,** *42*, 339-341.
41. Sheldrick, G. M., SHELXT - Integrated space-group and crystal-structure determination. *Acta. Cryst.* **2015,** *A71*, 3-8.
42. Sheldrick, G. M., Crystal structure refinement with SHELXL. *Acta Cryst.* **2015,** *C71*, 3.
43. Zhu, L. Y.; Yi, Y. P.; Li, Y.; Kim, E. G.; Coropceanu, V.; Bredas, J. L., Prediction of Remarkable Ambipolar Charge-Transport Characteristics in Organic Mixed-Stack Charge-Transfer Crystals. J Am Chem Soc 2012, 134 (4), 2340-2347.
44. Frisch, M. J.; Trucks, G. W.; Schlegel, H. B.; Scuseria, G. E.; Robb, M. A.; Cheeseman, J. R.; Scalmani, G.; Barone, V.; Mennucci, B.; Petersson, G. A.; Nakatsuji, H.; Caricato, M.; Li, X.; Hratchian, H. P.; Izmaylov, A. F.; Bloino, J.; Zheng, G.; Sonnenberg, J. L.; Hada, M.; Ehara, M.; Toyota, K.; Fukuda, R.; Hasegawa, J.; Ishida, M.; Nakajima, T.; Honda, Y.; Kitao, O.; Nakai, H.; Vreven, T.; Montgomery Jr., J. A.; Peralta, J. E.; Ogliaro, F. o.; Bearpark, M. J.; Heyd, J.; Brothers, E. N.; Kudin, K. N.; Staroverov, V. N.; Kobayashi, R.; Normand, J.; Raghavachari, K.; Rendell, A. P.; Burant, J. C.; Iyengar, S. S.; Tomasi, J.; Cossi, M.; Rega, N.; Millam, N. J.; Klene, M.; Knox, J. E.; Cross, J. B.; Bakken, V.; Adamo, C.; Jaramillo, J.; Gomperts, R.; Stratmann, R. E.; Yazyev, O.; Austin, A. J.; Cammi, R.; Pomelli, C.; Ochterski, J. W.; Martin, R. L.; Morokuma, K.; Zakrzewski, V. G.; Voth, G. A.; Salvador, P.; Dannenberg, J. J.; Dapprich, S.; Daniels, A. D.; Farkas, O.; Foresman, J. B.; Ortiz, J. V.; Cioslowski, J.; Fox, D. J. Gaussian 09, Gaussian, Inc.: Wallingford, CT, USA, 2009.
45. Dovesi, R.; Orlando, R.; Erba, A.; Zicovich-Wilson, C. M.; Civalleri, B.; Casassa, S.; Maschio, L.; Ferrabone, M.; De La Pierre, M.; D'Arco, P.; Noël, Y.; Causà, M.; Rérat, M.; Kirtman, B., CRYSTAL14: A program for the ab initio investigation of crystalline solids. Int. J. Quantum Chem. 2014, 114 (19), 1287-1317.
46. Dovesi, R.; V. R. Saunders; C. Roetti; R. Orlando; C. M. Zicovich-Wilson; F. Pascale; B. Civalleri; K. Doll; N. M. Harrison; I. J. Bush; P. D’Arco; M. Llunell; M. Causà; Noël, Y. CRYSTAL14 User's Manual, University of Torino, Torino, 2014.

Chapter 6 : Room-Temperature Ferroelectricity in Charge-Transfer Solid Solutions[*]

6.1 Introduction

The degree of charge transferred between π-electron donor (D) and acceptor (A) species in molecular cocrystals yields materials with diverse electronic properties.[1-9] In particular, charge-transfer (CT) cocrystals that display ferroelectric behavior have attracted much interest as promising alternatives to traditional inorganic materials in the areas of data storage and sensing[10-12] because they have the potential to offer solution processability,[13-15] cost effectiveness, and compatibility with flexible substrates.[16-18] However, ferroelectric CT cocrystals are rare due, in part, to the statistically disfavored noncentrosymmetry requirements necessary for ferroelectricity.[19] Additionally, most CT ferroelectrics that have been discovered thus far require cryogenic working temperature ranges,[11, 20] restricting the practical application of these materials.

Ferroelectric CT cocrystals operate through the deformation or displacement of D and/or A molecules in the solid-state under an applied electric field (E_C),[5, 21] leading to a shift in the net polarization of the solid that is retained when the electric field is removed. The molecular displacements that give rise to the polarization shift become disordered above the Curie temperature (T_C), resulting in reversible loss of ferroelectric behavior (see Figure 6.1).[20, 21] It has been observed that traversing the T_C is associated with a change in the degree of CT (ρ) of the DA complex between ionic ($\rho > 0.5$ electron, $D^+A^- D^+A^-$…) in the ferroelectric phase and neutral ($\rho < 0.5$ electron, $D\ A\ D\ A$…) in the paraelectric phase.[4, 11, 20, 22] This observation has led to the

---

[*] Unpublished work

development of cocrystal design strategies towards CT ferroelectrics that rely on identifying complementary *D* and *A* species predicted to show intermediate ρ values[23, 24] using solution-phase electrochemical potentials or computational methods to approximate the ionization potential of *D* and the electron affinity of *A*. When *D* and *A* are energy matched such that the radical ion pair D^+A^- is present in the ferroelectric phase, this design strategy predicts that the electronic instability of the D^+A^- dimer will drive structural transitions;[9, 11, 21] however, this approach has failed to produce ferroelectric materials with T_C values at temperatures relevant to practical application (>298 K).

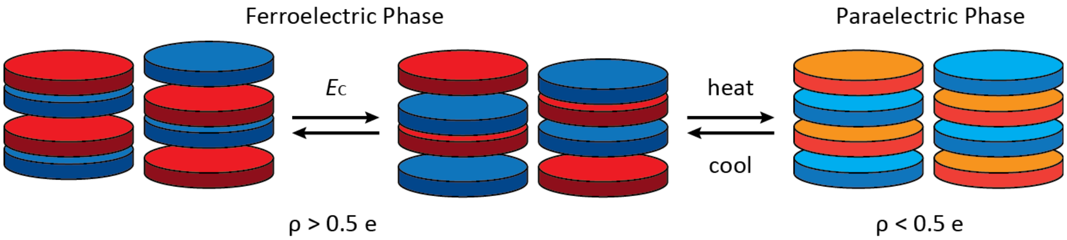

Figure 6.1. Mechanism of Polarization Switching in CT Cocrystals

Diagram summarizing the mechanism of ferroelectric switching by CT cocrystals in which red discs represent *D*, blue discs represent *A*, and a lightening or darkening of the disc color represent decreases or increases in the degree of CT (ρ), respectively.

Recently, it has been shown that thermally-activated vibrations and/or rotations of molecules within a CT cocrystal are sufficient to induce above-room temperature structural transitions between ferroelectric and paraelectric phases, even in the absence of transitions between ionic and neutral electronic states. [25] Though this CT material demonstrates ferroelectric behavior at room temperature, the polarization magnitudes measured from these materials are small compared to those of low-temperature CT ferroelectrics.[20, 25] Additionally, it has been found that CT cocrystals that show temperature-dependent neutral-ionic transitions do not necessarily show temperature-dependent structural transitions.[26, 27] Collectively, these findings indicate that instability of the $D^{+}A^{-}$ dimer may not be a significant driver of the molecular displacements necessary for ferroelectricity in these systems and that the conventional design strategy towards ferroelectric CT cocrystals should be revisited.

Herein we present a route by which to improve the ferroelectric performance of the room temperature ferroelectric CT cocrystal formed by acenaphthene (AN) and 2,3,5,6-tetrafluoro-7,7,8,8-tetracyanoquinodimethane (F_4TCNQ) through substitutional solid solution formation with the π-electron donors dihydronaphtho[1,8-*bc*]furan (DNF) and dihydronaphtho[1,8-*bc*]thiophene (DNT). Molecular solid solutions (alloys) are crystalline materials that can adopt continuously variable stoichiometries between compositional limits without dramatic changes in crystal packing (see Figure 6.2).[28-30] Molecular solid solutions have been shown to alter the electronic behavior of molecular crystals as well as the degree of CT (ρ) in isostructural CT materials.[31] Maintaining the crystal packing of a known ferroelectric host phase by utilizing the solid solution approach is desirable because improvements in the ferroelectric behavior can be achieved without screening for CT conformer combinations that produce polar crystal symmetries. By introducing new charge states into the ferroelectric CT host material AN-F_4TCNQ, the effect of altering the degree of CT on the neutral-ionic transition and the impact on room-temperature remanent polarization, P_r, can be investigated. Furthermore, controllably introducing ionic charge states into the ferroelectric host can clarify the role that the neutral-ionic transition may have on both the T_C and P_r with the goal of refining approaches towards the design of CT ferroelectrics.

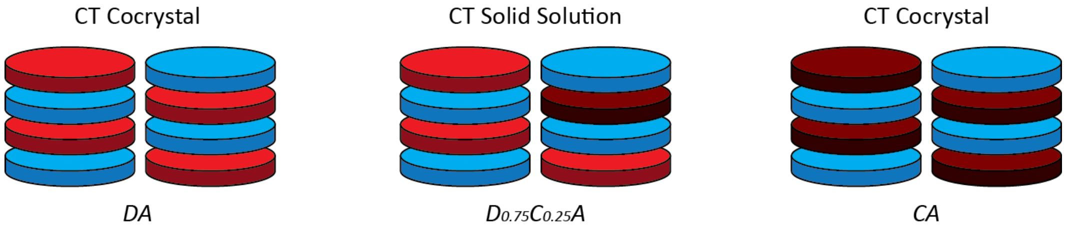

Figure 6.2. Diagram of a Ternary CT Solid Solution

Diagram of a solid solution between CT cocrystal *DA* and *CA* in which molecules *D*, *C*, and *A* are represented by red, maroon, and blue discs, respectively.

6.2 Results and Discussion

The crystallographic features relevant to the ferroelectric behavior of AN-F_4TCNQ are briefly summarized here and described in detail in the original report.[25] The cocrystal adopts the polar *Pc* space group at room temperature with a mixed stacking motif in which AN and F_4TCNQ molecules are dimerized along the π-stacking direction such that the polarization vector is aligned parallel to the *a*-axis. When heated to 68 °C, the cocrystal undergoes a phase transition associated with thermally-induced flip-flop disordering of AN molecules. The disorder in AN above the transition temperature breaks the dimerization pattern along the π-stacking direction, causing symmetrization of the unit cell ($P2_1/c$) and reversible loss of ferroelectric behavior.[25] Remanent polarization hysteresis was measured for this cocrystal, confirming its ferroelectric behavior at room temperature; however, the P_r magnitude is small compared to those of high-performing cryogenic ferroelectric CT cocrystals.[25] The low P_r was attributed to a small degree of CT and minimal change in the degree of CT upon transitioning between ferroelectric and paraelectric phases.[25]

6.2.1 Dopant Selection

DNF and DNT (see Figure 6.3) were selected as dopant species for the AN-F_4TCNQ host material due to the similarity in molecular structure between DNF, DNT, and AN as well as the position of the calculated HOMO energy levels (DNF = -5.57 eV and DNT = 5.51 eV) relative to the position of the LUMO of F_4TCNQ (-5.50 eV). The minimal difference in energy between the HOMO positions of dopant molecules and the LUMO of F_4TCNQ suggests that the DNF-F_4TCNQ and DNT-F_4TCNQ pairs would form ionic D^+A^- complexes.[8, 25] Although the electronic properties of DNF and DNT are calculated to be similar, the two dopants are distinguished by the differences in molecular volume compared to that of AN, which may have significant consequences on the solubility of the dopants in the ferroelectric structural phase and the crystal structure of the solid solution.[32] The molecular volumes of DNF, DNT, and AN were calculated from the volume enclosed by an isodensity surface calculated (B3LYP/6-311G(d,p)) for the equilibrium geometries and it was found that DNF is 94% of the volume of AN and DNT is 104% the volume of AN, suggesting that both dopants are likely to substitutionally replace AN without causing significant changes in crystal packing.[33]

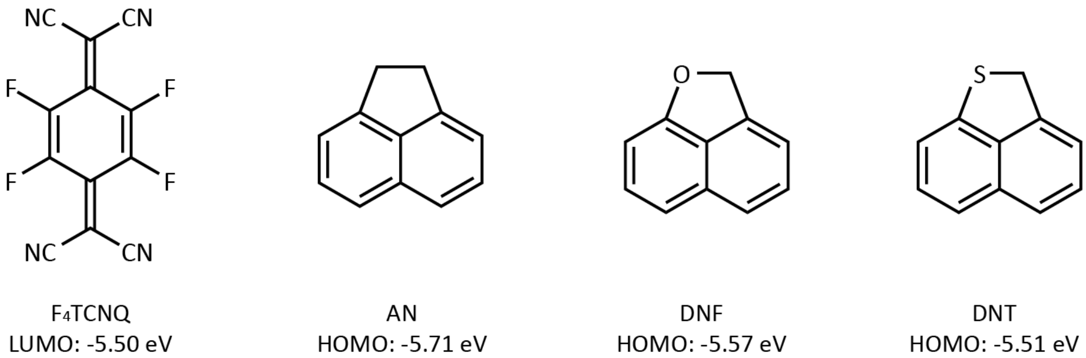

F_4TCNQ
LUMO: -5.50 eV

AN
HOMO: -5.71 eV

DNF
HOMO: -5.57 eV

DNT
HOMO: -5.51 eV

Figure 6.3. Molecular Structures for F_4TCNQ, AN, DNF, and DNT

6.2.2 The DNF-F_4TCNQ and DNT-F_4TCNQ Cocrystals

In addition to molecular structure similarity, isostructurality between cocrystal phases can also be predictive of solid solution formation because the probability of preserving favorable local interactions in the solid solution phase between two isostructural materials is high relative to solid solutions formed between non-isostructural materials.[30, 32] Single crystals of the DNF-F_4TCNQ and DNT-F_4TCNQ cocrystals were prepared from acetonitrile solutions and the structure determined by single-crystal X-ray diffraction (SCXRD). At room temperature, DNF-F_4TCNQ crystallizes in the centrosymmetric $P2_1/c$ space group with half of a molecule of DNF and half of a molecule of F_4TCNQ in the asymmetric unit, confirming a 1:1 stoichiometric ratio between the two components (see Figure 6.4). DNF-F_4TCNQ adopts a mixed stacking motif and shows disorder of the DNF molecule over two positions related by inversion, similar to the paraelectric phase of AN-F_4TCNQ (see Figure 6.4). The crystal packing similarity of the DNF-F_4TCNQ cocrystal relative to AN-F_4TCNQ was evaluated by calculating the similarity in simulated powder XRD patterns between these two materials using the Materials Module available through Mercury CSD 3.7. Using this approach, it was found that the crystal structure of the DNF-F_4TCNQ cocrystal is 92.7% similar to that of AN-F_4TCNQ at room temperature), indicating a strong likelihood that DNF would substitutionally replace AN in a solid solution phase between DNF, AN, and F_4TCNQ.

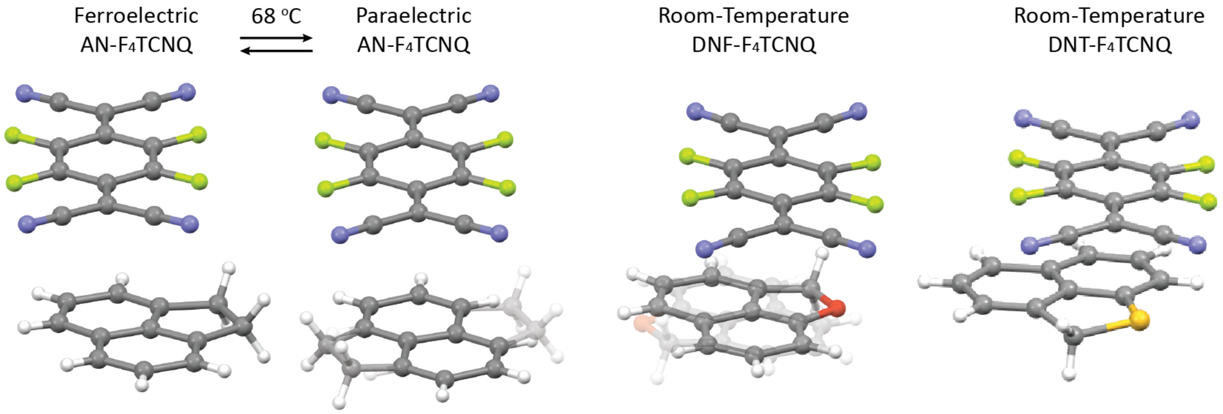

Figure 6.4. The Cocrystal Structures of AN-F_4TCNQ, DNF-F_4TCNQ, and DNT-F_4TCNQ

Experimental crystal structures of the ferroelectric and paraelectric phases of the AN-F_4TCNQ cocrystal compared to a similar view of the DNF-F_4TCNQ cocrystal structure to highlight structural similarity.

The cocrystal formed between DNT and F_4TCNQ crystallizes in the polar $P2_1$ space group at room temperature with one molecule of DNT and one molecule of F_4TCNQ in the asymmetric unit, confirming the 1:1 stoichiometry between the donor and acceptor (see Figure 6.4). The DNT-F_4TCNQ cocrystal is isostructural to the DNF-F_4TCNQ, cocrystal, although it lacks a center of symmetry. The cocrystal adopts a mixed stacking motif with alternating short and long π-stacking distances between the donor (mean centroid) and acceptor (mean plane) of 3.389 Å and 3.422 Å. Although they fall into different space groups, DNT-F_4TCNQ resembles the ferroelectric phase of AN-F_4TCNQ, which also shows dimerization of *D* and *A* along the CT direction with alternating short and long π-stacking distances of 3.369 Å and 3.461 Å. The DNT molecule is disordered over two positions related by reflection such that the thioether bridge orientation is unspecific. Using the Materials Module in Mercury, the predicted PXRD similarity index for DNT-F_4TCNQ compared to AN-F_4TCNQ was calculated as 90.1%, suggesting that DNT is likely less soluble than DNF in the solid solution phase although still likely to substitutionally replace AN in a solid solution.

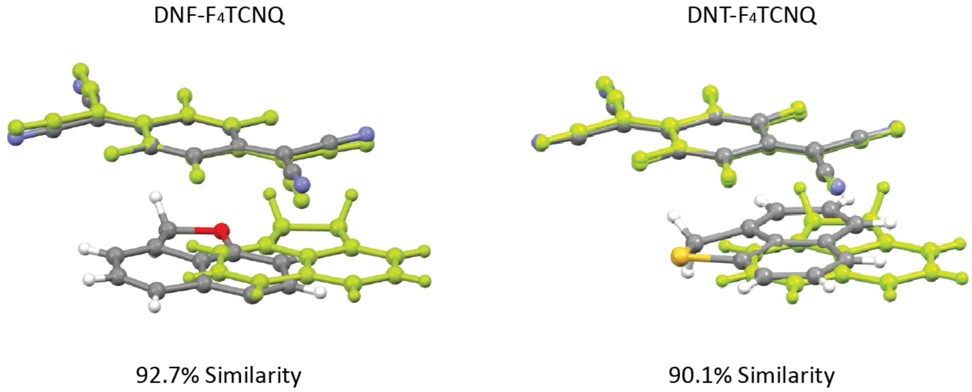

Figure 6.5. Structure Overlay of AN-F_4TCNQ, DNF-F_4TCNQ, and DNT-F_4TCNQ

Overlays of the DNF-F_4TCNQ (left) and DNT-F_4TCNQ (right) crystal structures colored by atom type with a similar view of the AN-F4TCNQ crystal structure with all atom types in green.

Table 6.1. Crystallographic Data for the F_4TCNQ-Based CT Cocrystals

	AN-F_4TCNQ	DNF-F_4TCNQ	DNT-F_4TCNQ
Space Group	*Pc*	$P2_1/c$	$P2_1/c$
a (Å)	9.467(3)	7.2839(3)	8.0852(7)
b (Å)	7.995(3)	7.1849(4)	7.3319(6)
c (Å)	13.369(4)	17.9139(7)	16.6414(10)
α (°)	90	90	90
β (°)	109.43(3)	95.506(4)	94.017(8)
γ (°)	90	90	90
V (Å^3)	954.2(6)	933.182	984.077

DNF and DNT were selected as dopant molecules because they were computationally predicted to increase the degree of CT (ρ) in solid solutions formed with AN-F_4TCNQ based on the relative energies of the F_4TCNQ LUMO and donor HOMOs. To investigate this prediction, ρ was quantified for the DNF-F_4TCNQ and DNT-F_4TCNQ cocrystals by measuring the F_4TCNQ nitrile stretching frequencies of the cocrystals using Raman spectroscopy (see Figure 6.6).[25, 26, 34] A Raman spectrum could not be obtained for the DNT-F_4TCNQ cocrystal due to a high background and low signal-to-noise likely attributable to a combination of sample fluorescence and degradation. A Raman spectrum could, however, be collected for the DNF-F_4TCNQ cocrystal. It was found that, in addition to the bands at 2223 cm^{-1} and 2214 cm^{-1} that represent primarily neutral F_4TCNQ (ρ = ~0.3 e), a band at 2199 cm^{-1} is present (see Figure 6.6), representing the primarily radical anionic F_4TCNQ^- (ρ = ~0.9 e).[34] This set of nitrile stretching frequencies suggests that the DNF-F_4TCNQ cocrystal exhibits a mixture of CT states between primarily neutral and primarily ionic, further supporting the use of DNF as a dopant in the AN-F_4TCNQ ferroelectric to alter ρ. Due to the similarity in calculated HOMO energy level, it is likely that the DNT-F_4TCNQ cocrystal shows a similar increase in ρ as DNF-F_4TCNQ.

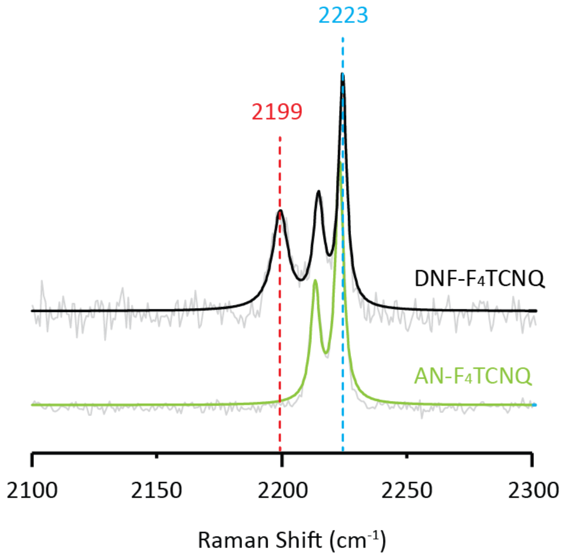

Figure 6.6. Fitted Raman Spectra of AN-F_4TCNQ and DNF-F_4TCNQ

Raman spectra fitted with Lorentzian line shapes of the AN-F_4TCNQ and DNF-F_4TCNQ cocrystals centered on the nitrile stretching region with the 2223 cm^{-1} and 2199 cm^{-1} vibrational bands highlighted in blue and red bands, respectively.

6.2.3 The Crystal Structures of $DNF_XAN_{(1-X)}F_4TCNQ$ and $DNT_XAN_{(1-X)}F_4TCNQ$ Solid Solutions

Ternary solid solutions formed between DNF and the AN-F_4TCNQ host material, $DNF_XAN_{(1-X)}F_4TCNQ$, were prepared from solutions containing variable DNF:AN concentrations in a mixed acetonitrile-diethyl ether solvent system. It was found that when growth of the solid solution phase was attempted from acetonitrile solutions in the absence of diethyl ether, DNF was not incorporated into the AN-F_4TCNQ host phase at appreciable concentrations. This behavior is likely due to the difference in solubility between the AN-F_4TCNQ and DNF-F_4TCNQ complexes under the crystallization conditions. DNF incorporation in single crystals of the $\text{DNF}_X\text{AN}_{(1-X)}\text{F}_4$TCNQ solid solution produced from acetonitrile-diethyl ether was determined by the relative integration of ^{1}H Nuclear Magnetic Resonance (NMR) spectroscopy proton peaks associated with the AN ethylene bridge and DNF ether bridge for dissolved $\text{DNF}_X\text{AN}_{(1-X)}\text{F}_4$TCNQ solid solution crystals. Using this method, it was found that solid solutions could be formed with 0 – 100% DNF incorporation, although it should be noted that single crystals with high incorporation (>83%) of DNF are morphologically distinct from those with low incorporation of DNF, suggesting the solid solution may show composition-dependent structural changes (morphotropism). Ternary solid solutions between DNT and AN-F_4TCNQ were also crystallized from an acetonitrile-diethyl ether solvent system and the incorporation of the dopant quantified by a combination of ^{1}H NMR spectroscopy and XRD. DNT was incorporated into the $\text{DNT}_X\text{AN}_{(1-X)}\text{F}_4$TCNQ solid solution at concentrations between 0 – 63%, above which concentration, crystals did not form by this crystallization method. Similar to the $\text{DNF}_X\text{AN}_{(1-X)}\text{F}_4$TCNQ solid solution crystals, at high incorporation of DNT (>44%), a physical mixture of different crystal morphologies were observed.

Table 6.2. Feed Ratios and Experimentally Determined Solid Solution Compositions

(a) Feed and crystal ratios for $\text{DNF}_X\text{AN}_{(1-X)}\text{F}_4$TCNQ determined from ^{1}H NMR integrations

Sample	Feed Ratio DNF : AN	^{1}H Integration Ratio DNF : AN	Crystal Ratio DNF : AN
A	0 : 100	-	0%
B	9 : 91	1 : 41.9	5%
C	19 : 81	1 : 12.5	14%
D	31 : 69	1 : 15.0	12%

E	42 : 58	1 : 9.0	18%
F	51 : 49	1 : 5.3	27%
G	60 : 40	1 : 5.0	29%
H	70 : 30	1 : 3.0	40%
I	80 : 20	1 : 1.2	63%
J	90 : 10	1 : 0.4	83%
K	100 : 0	-	100%

(b) Feed and crystal ratios for $DNT_X AN_{(1-X)} F_4TCNQ$ determined from ^{1}H NMR integrations

Sample	Feed Ratio DNT : AN	^{1}H Integration Ratio DNT : AN	DNT Incorporation
A	0 : 100	-	0%
B	11 : 89	1 : 21.1	9%
C	20 : 80	1 : 15.0	12%
D	30 : 70	1 : 8.1	19%
E	40 : 60	1 : 5.0	29%
F	49 : 51	1 : 4.0	33%
G	59 : 41	1 : 2.5	44%
H	72 : 28	**From XRD Data**	63%
I	80 : 20	Did Not Form	-
J	89 : 11	Did Not Form	-
K	100 : 0	-	100%

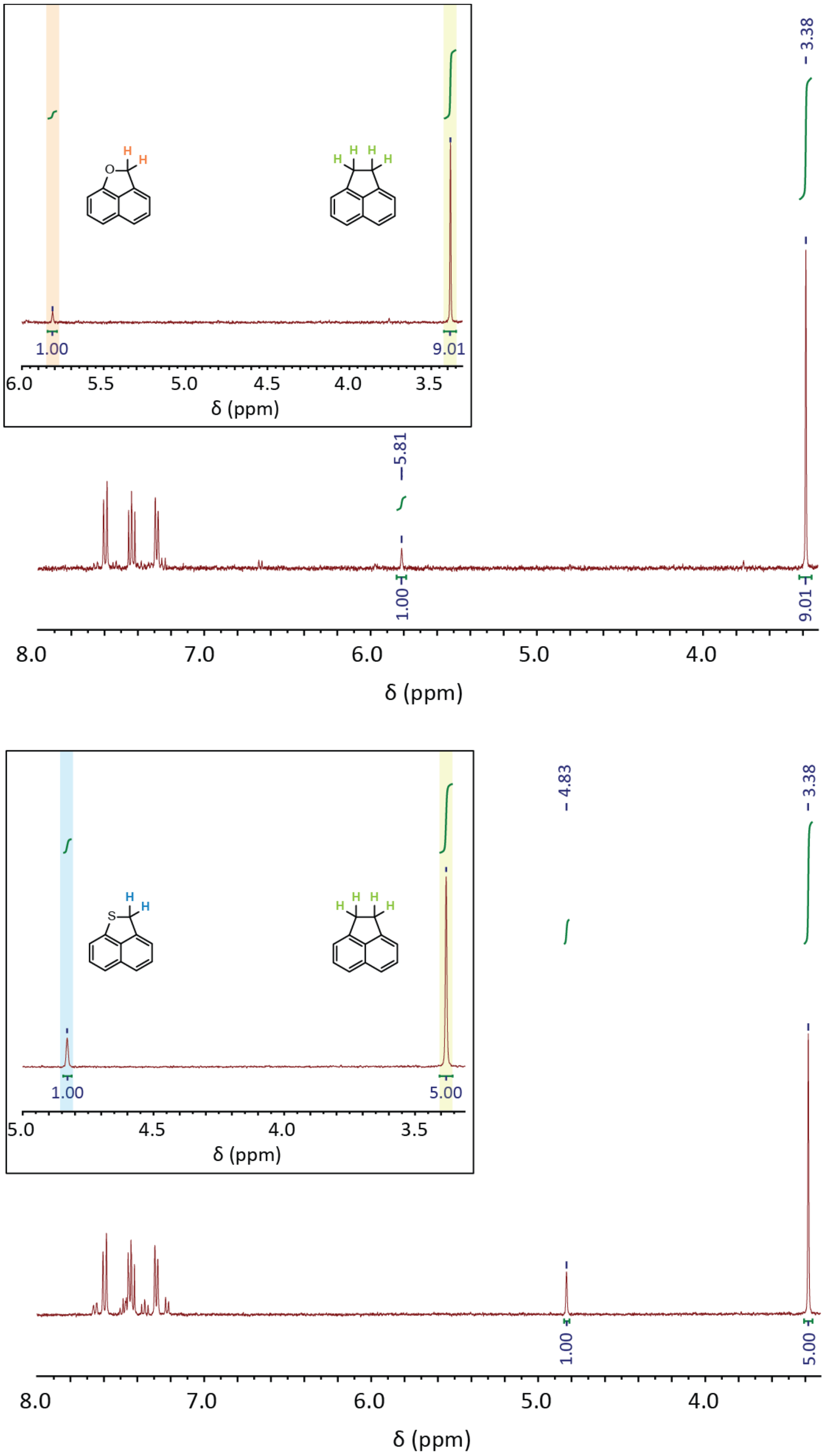

Figure 6.7. ^{1}H NMR Spectra for Intermediate Compositions of the Solid Solutions

(Top) Typical ^{1}H NMR spectrum for DNF-AN-F_4TCNQ sample E collected at room temperature in acetone-d_6. Integrations correspond to the ethylene on AN (3.38 ppm) and the methylene on DNF (5.81 ppm). (Bottom) Typical ^{1}H NMR spectrum for

DNT-AN-F_4TCNQ sample E collected at room temperature in acetone-d_6. Integrations correspond to the ethylene on AN (3.38 ppm) and the methylene on DNT (4.83 ppm).

To study the effect of dopant incorporation on solid state packing, the unit cell parameters were measured for the solid solutions as a function of DNF and DNT incorporation. It was found that the change in morphology for both solid solutions is associated with a change in the unit cell parameters from the AN-F_4TCNQ cocrystal phase ($\beta \sim 109°$) to the DNF-F_4TCNQ and DNT-F_4TCNQ cocrystal phase ($\beta \sim 95°$). Additional diffraction data were collected to determine the crystallographic centrosymmetry as a function of dopant incorporation. The $DNF_XAN_{(1-X)}F_4$TCNQ solid solution shows three structural phases as a function of DNF incorporation, confirming the morphotropism (see Figure 6.8): at DNF incorporation percentages between 0-14% (phase I), $DNF_XAN_{(1-X)}F_4$TCNQ adopts the polar *Pc* phase, at 15-63% incorporation of DNF (phase II), $DNF_XAN_{(1-X)}F_4$TCNQ solves in the $P2_1/c$ space group at room temperature with disorder of the donor over two positions related by inversion, and at >64% incorporation of DNF (phase III), $DNF_XAN_{(1-X)}F_4$TCNQ again solves in the $P2_1/c$ space group but is isomorphous with the DNF-F_4TCNQ cocrystal ($\beta \sim 95°$). The $DNT_XAN_{(1-X)}F_4$TCNQ solid solution also shows three distinct structural phases as a function of dopant incorporation identical to those for the $DNF_XAN_{(1-X)}F_4$TCNQ solid solution at low (0-12%), medium (12-63(10)%) and high (100%) DNT incorporation. These results indicate that, while DNT is much closer in molecular volume to AN than is DNF, both dopants show identical changes to the crystal packing at similar incorporation percentages, suggesting that crystallographic similarity may be a more reliable predictor of the structural effects of dopant incorporation on solid solutions given that DNF-F_4TCNQ and DNT-F_4TCNQ are isostructural.

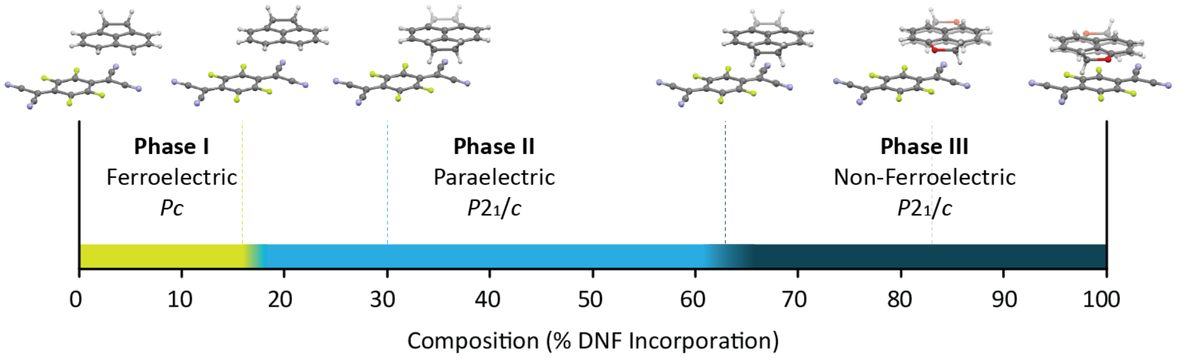

Figure 6.8. Structural Phases of the $DNF_{X}AN_{(1-X)}F_4TCNQ$ Solid Solution

Diagram showing the three structural phases for $DNF_{X}AN_{(1-X)}F_4TCNQ$ at room temperature as a function of DNF incorporation. Phase I solves in Pc and has therefore has the appropriate symmetry to show ferroelectricity. Phase II is isomorphous with the paraelectric phase of AN-F4TCNQ. Phase III is isomorphous with DNF-F4TCNQ, which does not show the appropriate symmetry for ferroelectricity.

Table 6.3. Unit Cell Parameters for $DNF_{X}AN_{(1-X)}F_4TCNQ$ and $DNT_{X}AN_{(1-X)}F_4TCNQ$

(a) Composition-dependent unit cell parameters for $DNF_{X}AN_{(1-X)}F_4TCNQ$ solid solutions

Sample	Crystal Ratio	Space Group	*a* (Å)	*b* (Å)	*c* (Å)	β (°)	V (Å^3)
A	0%	*Pc*	9.467(3)	7.995(3)	13.369(4)	109.43(3)	954.2(6)
B	5%	*Pc*	9.465(3)	7.988(3)	13.359(6)	109.33(4)	953.1(7)
C	14%	*Pc*, $P2_1/c$	9.469(3)	7.987(4)	13.386(5)	109.37(4)	955.1(6)
D	12%	$P2_1/c$	9.484(4)	7.960(3)	13.395(10)	109.31(6)	954.3(8)
E	18%	$P2_1/c$	9.482(6)	7.987(4)	13.378(6)	109.35(5)	955.9(9)
F	27%	$P2_1/c$	9.474(4)	7.982(4)	13.386(4)	109.42(4)	954.6(7)
G	29%	$P2_1/c$	9.477(2)	7.992(3)	13.376(4)	109.40(3)	955.6(5)
H	40%	$P2_1/c$	9.487(4)	7.935(8)	13.392(19)	109.25(8)	952(2)
I	63%	$P2_1/c$	9.485(6)	7.874(2)	13.428(4)	109.18(5)	947.2(7)
J	83%	$P2_1/c$	7.316(5)	7.303(14)	17.827(16)	95.13(7)	949(2)
K	100%	$P2_1/c$	7.2839(3)	7.1849(4)	17.9139(7)	95.506(4)	933.18(1)

(b) Composition-dependent unit cell parameters for $DNT_{X}AN_{(1-X)}F_4TCNQ$ solid solutions

Sample	DNT Incorp.	Space Group	*a* (Å)	*b* (Å)	*c* (Å)	β (°)	V (Å^3)
A	0%	*Pc*	9.467(3)	7.995(3)	13.369(4)	109.43(3)	954.2(6)
B	9%	*Pc*	9.4776(8)	7.9912(6)	13.3760(17)	109.346(11)	955.86(17)
C	12%	*Pc*	9.4729(8)	7.9903(4)	13.3922(8)	109.220(8)	957.17(12)
D	19%	$P2_1/c$	9.4827(10)	7.9825(5)	13.4148(15)	109.155(11)	959.22(17)
E	29%	$P2_1/c$	9.5442(12)	7.8632(13)	13.6736(12)	108.650(12)	972.3(2)

F	33%	$P2_1/c$	9.572(7)	7.836(5)	13.731(8)	108.63(6)	976(1)
G	44%	$P2_1/c$	9.597(6)	7.792(5)	13.771(8)	108.38(5)	977(1)
H	63(10)%	$P2_1/c$	9.65(4)	7.76(2)	13.89(10)	108.2(6)	988(9)
I	-		Did Not Form				
J	-		Did Not Form				
K	100%	$P2_1$	8.0852(7)	7.3319(6)	16.6414(10)	94.017(8)	984.07(1)

6.2.4 Degree of CT in $DNF_XAN_{(1-X)}F_4TCNQ$ and $DNT_XAN_{(1-X)}F_4TCNQ$ Solid Solutions

Raman spectra centered around 2220 cm^{-1} (F_4TCNQ nitrile stretching region) were collected for $DNF_XAN_{(1-X)}F_4TCNQ$ and $DNT_XAN_{(1-X)}F_4TCNQ$ solid solutions to investigate the degree of CT. Both solid solutions have three distinct peaks in the nitrile region at 2223 cm^{-1}, 2214 cm^{-1}, and 2199 cm^{-1}, similar to those observed for the DNF-F_4TCNQ cocrystal (see Figure 6.9), suggesting that the solid solutions also show a mixture of neutral and radical charge states. The relative height and area of the 2199 cm^{-1} Raman peak increases with dopant incorporation. Additionally, it was found that DNT leads to more dramatic increases in the height and area of the 2199 cm^{-1} Raman peak than does DNF at similar percent incorporations. This observation is consistent with the difference in energy between the calculated positions of the frontier molecular orbital energies for the dopant species and F_4TCNQ. The difference in frontier molecular orbital energy positions for the DNF-F_4TCNQ complex is 0.06 eV and that for the DNT-F_4TCNQ complex is 0.01 eV, which suggests that DNT-F_4TCNQ should show a greater population of ionic charge-transfer states. The ρ values were estimated for the $DNF_XAN_{(1-X)}F_4TCNQ$ and $DNT_XAN_{(1-X)}F_4TCNQ$ solid solutions as a function of dopant incorporation by fitting the three nitrile stretching frequencies to Lorentzian line shapes and averaging the relative areas of the Raman peaks at 2214 cm^{-1} and 2199 cm^{-1}, leading to ρ values ranging from 0.2 - 0.3 e for phase I DNF solid solutions and 0.2 – 0.7 e for phase I DNT solid solutions. It was found that the Raman peak associated with the radical anionic state was about eight times larger by area for the DNT$_X$AN$_{(1-X)}$F$_4$TCNQ solid solution than for the DNF$_X$AN$_{(1-X)}$F$_4$TCNQ solid solution at the same dopant incorporation.

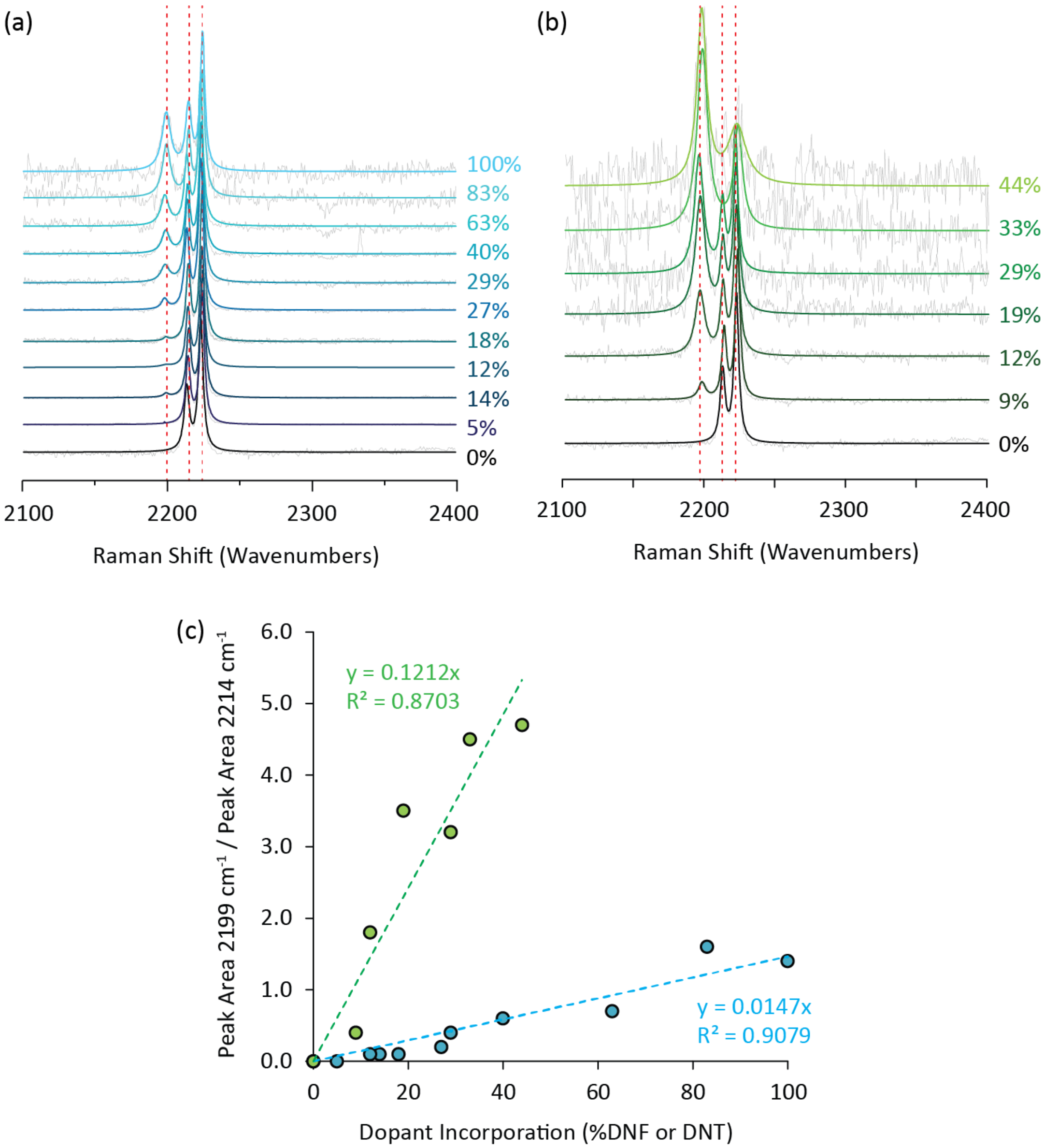

Figure 6.9. Composition-Dependent Fitted Raman Spectra for the Solid Solutions

(a) Composition-dependent fitted Raman spectra of the DNF$_X$AN$_{(1-X)}$F$_4$TCNQ solid solution focused on the nitrile stretching region with the AN-F$_4$TCNQ cocrystal shown in black and the DNF-F$_4$TCNQ cocrystal shown in light blue. Intermediate colors represent intermediate compositions; (b) composition-dependent fitted Raman spectra of the DNT$_X$AN$_{(1-X)}$F$_4$TCNQ solid solution focused on the nitrile stretching region with the AN-F$_4$TCNQ cocrystal shown in black and the DNT$_{0.44}$AN$_{0.56}$F$_4$TCNQ solid solution shown in light green. Intermediate colors represent intermediate compositions. Red dashed lines highlight the 2223 cm^{-1}, 2214 cm^{-1}, and 2199 cm^{-1} stretches; (c) composition-dependent increases in the 2199 cm^{-1} Raman peak area for DNF$_X$AN$_{(1-X)}$F$_4$TCNQ (blue) and DNT$_X$AN$_{(1-X)}$F$_4$TCNQ (green).

Table 6.4. Fitted Raman Peak Positions and Areas and CT for the Solid Solutions

(a) Table of peak positions and integrations from fitting $DNF_XAN_{(1-X)}F_4TCNQ$ solid solution Raman spectra with Lorentzian peak shapes. Peak positions were used to estimate ρ values in electrons.

Sample	Crystal Ratio	Peak 1 (cm^{-1})	Peak 2 (cm^{-1})	Peak 3 (cm^{-1})	Rel Peak 1 Integration	Rel Peak 2 Integration	Rel Peak 3 Integration	Average ρ (electrons)
A	0%		2213.4	2223.0		1	2	0.2
B	5%	2198.1	2214.3	2224.0	0	1	2	0.2
C	14%	2198.6	2214.2	2224.0	0.1	1	2	0.3
D	12%	2198.8	2214.2	2223.8	0.1	1	2	0.3
E	18%	2198.5	2214.1	2223.8	0.1	1	2	0.3
F	27%	2198.3	2213.8	2223.4	0.2	1	2	0.3
G	29%	2198.7	2214.0	2223.7	0.4	1	2	0.4
H	40%	2198.4	2213.6	2223.2	0.6	1	2	0.5
I	63%	2198.7	2213.8	2223.4	0.7	1	2	0.5
J	83%	2199.0	2214.3	2223.7	1.6	1	2	0.7
K	100%	2198.9	2214.2	2223.9	1.4	1	2	0.7

(b) Table of peak positions and integrations from fitting $DNT_XAN_{(1-X)}F_4TCNQ$ solid solution Raman spectra with Lorentzian peak shapes. Peak positions were used to estimate ρ values in electrons.

Sample	DNT Incorporation	Peak 1 (cm^{-1})	Peak 2 (cm^{-1})	Peak 3 (cm^{-1})	Rel Peak 1 Integration	Rel Peak 2 Integration	Rel Peak 3 Integration	ρ (electrons)
A	0%		2213.4	2223.0		1	2	0.2
B	9%	2198.7	2214.3	2223.9	0.4	1	2	0.4
C	12%	2197.4	2213.7	2223.1	1.8	1	2	0.7
D	19%	2197.5	2213.5	2222.7	3.5	1	2	0.8
E	29%	2197.2	2213.8	2222.7	3.2	1	2	0.8
F	33%	2198.3	-	2223.5	4.5	-	2	0.9
G	44%	2198.6	-	2223.5	4.7	-	2	0.9
H	63%	Poor Signal-to-Noise						
I	-	Did Not Form						
J	-	Did Not Form						
K	100%	Poor Signal-to-Noise						

6.2.5 $DNF_XAN_{(1-X)}F_4TCNQ$ and $DNT_XAN_{(1-X)}F_4TCNQ$ Solid Solutions and the T_C

The phase I solid solutions show the appropriate symmetry for ferroelectricity by adopting the same structural phase as the AN-F_4TCNQ cocrystal at room temperature. To investigate whether these materials show a T_C similar to that of the AN-F_4TCNQ cocrystal, differential scanning calorimetry (DSC) traces were collected for solid solutions solving in the *Pc* space group. Solid solutions of both dopant species showed relatively small thermal events at elevated temperature likely associated with the flip-flop disorder of the donor and change in crystallographic symmetry observed for the AN-F_4TCNQ cocrystal.[25] In both solid solutions, the temperature of the thermal event was depressed relative to the pure AN-F_4TCNQ cocrystal (68 °C): 66 °C for $DNF_{0.14}AN_{0.86}F_4TCNQ$ and 56 °C for $DNT_{0.12}AN_{0.88}F_4TCNQ$ (see Figure 6.10). In order to further investigate the phase transition identified by DSC, the temperature-dependent expansion of the *c*-axis length was measured.

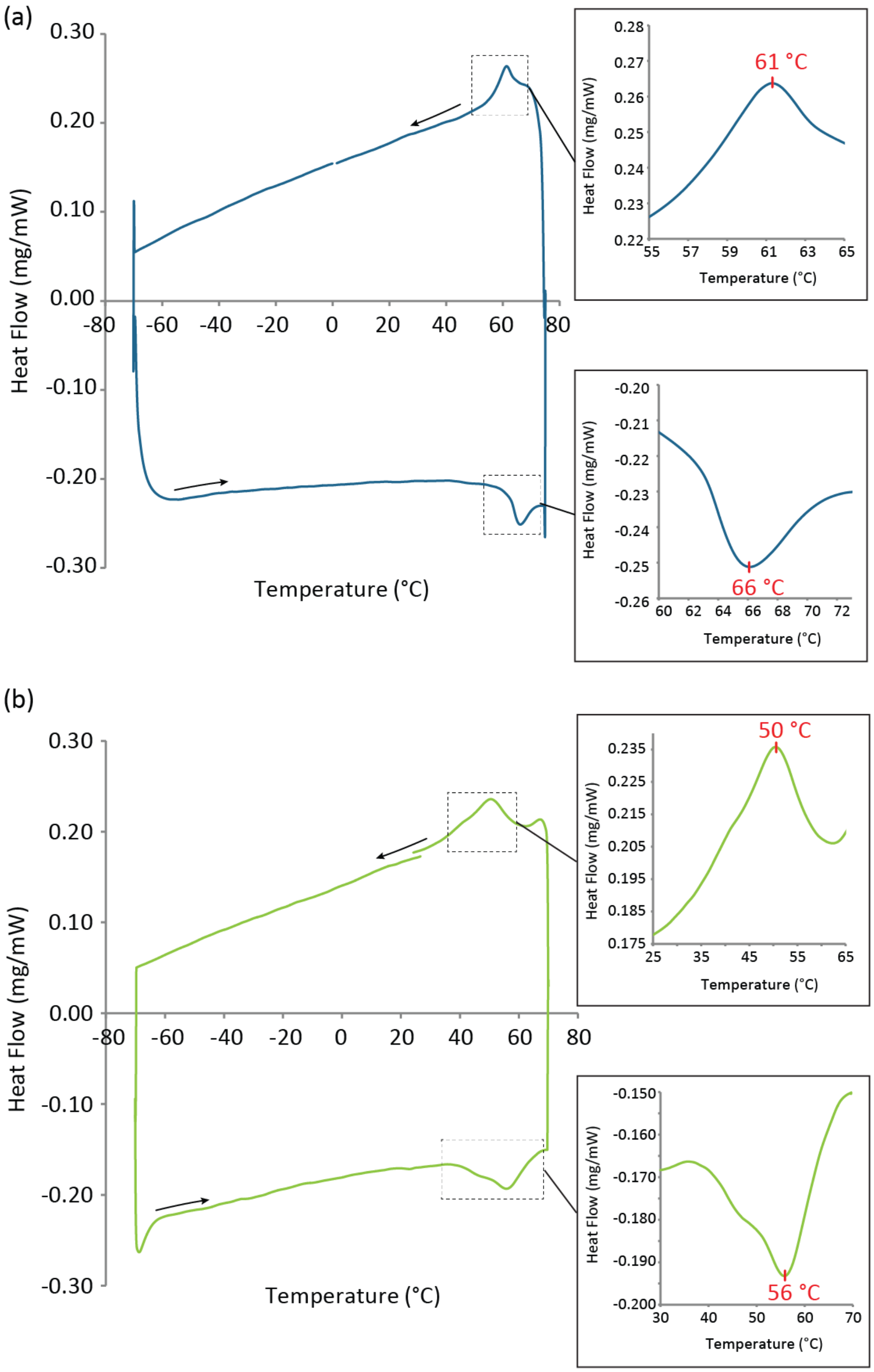

Figure 6.10. DSC Traces for DNF$_{0.14}$AN$_{0.86}$F$_4$TCNQ and DNT$_{0.12}$AN$_{0.88}$F$_4$TCNQ

(a) Differential scanning calorimetry trace for DNF$_{0.14}$AN$_{0.86}$F$_4$TCNQ (Sample C) with insets highlighting the transition between the ferroelectric and paraelectric phases. (b) Differential scanning calorimetry trace for DNT$_{0.12}$AN$_{0.88}$F$_4$TCNQ (Sample C) with insets highlighting the transition between the ferroelectric and paraelectric phases. Exotherms shown as upward peaks.

As shown in the original report of the AN-F_4TCNQ cocrystal, temperature-dependent expansion of the *c*-axis length can be used to approximate the temperature at which flip-flop disorder in AN is thermally activated, about 10 °C lower in temperature than the T_C.[25] This temperature is demarcated by a threefold increase in the linear coefficient of thermal expansion (CTE) of the *c*-axis length. For this reason, the *c*-axis length was measured as a function of temperature to determine whether and at what temperature(s) $DNF_{X}AN_{(1-X)}F_4TCNQ$ single crystals demonstrate thermally-activated flip-flop disorder of the dopant. Single crystals of phase I $DNF_{X}AN_{(1-X)}F_4TCNQ$ were indexed using VT-SCXRD, revealing a change in the linear CTE of the *c*-axis between 55 and 60 °C closely corresponding to that of the AN-F_4TCNQ cocrystal, indicating retention of the thermally-activated flip-flop transition necessary for ferroelectricity in AN-F_4TCNQ and suggesting that the thermal events observed by DSC are T_C values for the solid solutions. Variable-temperature Raman spectroscopy of $DNT_{0.12}AN_{0.88}F_4TCNQ$ was performed to determine whether the T_C was associated with a transition from a primarily ionic to primarily neutral charge state. It was found that there were minimal changes in the relative peak heights or areas of the 2223 cm^{-1}, 2214 cm^{-1}, and 2199 cm^{-1} peaks associated with nitrile stretching as a function of temperature (Figure 6.11), indicating that changes in the ionicity of the CT solid solution as a function of temperature are insignificant.

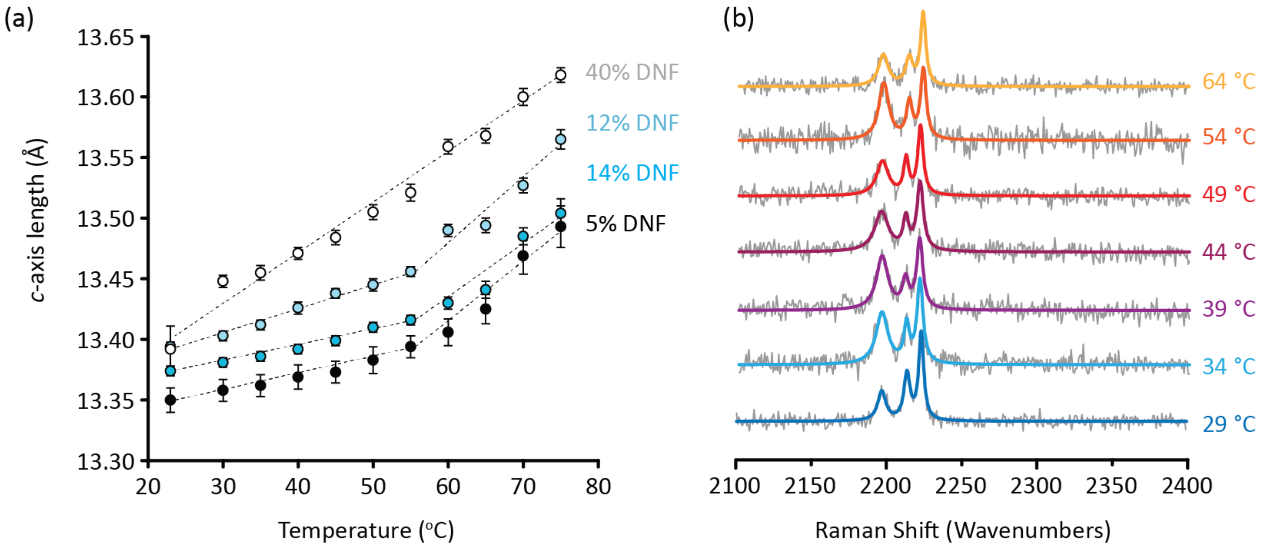

Figure 6.11. VT-SCXRD and VT-Raman Spectroscopy for the Phase I Solid Solutions

(a) Thermal expansion of the c-axis length for various $DNF_{X}AN_{(1-X)}F_4TCNQ$ solid solution compositions highlighting the change in the linear coefficient of thermal expansion (slope) near the T_C for phase I $DNF_{X}AN_{(1-X)}F_4TCNQ$ solid solutions. (b) Raman spectra of $DNT_{0.12}AN_{0.88}F_4TCNQ$ at various temperatures showing that the Raman peak intensities maintain consistent relative peak areas.

6.2.6 Electrical Characterization for $DNF_{X}AN_{(1-X)}F_4TCNQ$

Through a combination of X-ray diffraction and Raman spectroscopy it was shown that the structural characteristics of AN-F_4TCNQ necessary for ferroelectricity were retained when doped with 0-14% of DNF or DNT and that the average degree of CT was increased from 0.2 e for the AN-F_4TCNQ cocrystal to 0.3 e for $DNF_{0.14}AN_{0.86}F_4TCNQ$ and to 0.7 e for $DNT_{0.12}AN_{0.88}F_4TCNQ$; however, it was shown that traversing the T_C and undergoing the ferroelectric-to-paraelectric symmetry change did not lead to a significant change in the degree of CT for $DNT_{0.12}AN_{0.88}F_4TCNQ$. The effects of the increase in the average degree of CT on the remanent polarization were investigated for $DNF_{X}AN_{(1-X)}F_4TCNQ$ because large enough single crystals of the solid solution could be produced by implementing the crystallization method described in the Experimental Methods. Unfortunately single crystals of $DNT_{X}AN_{(1-X)}F_4TCNQ$, were not large enough to apply viable contacts with silver paint.

Single crystals of $DNF_{X}AN_{(1-X)}F_4TCNQ$ were contacted with silver paint on the (100) and (-100) faces, as described in the original report of AN-F_4TCNQ.[25] Direct polarization hysteresis loops were measured to inspect the quality and confirm the correct placement of the electrical contacts before collecting positive-up-negative-down (PUND) pulse measurements and remanent hysteresis loops. Polarization and PUND data were collected for cocrystal/solid solution samples containing 0%, 12%, 14%, and 27% DNF incorporation. The PUND measurements revealed that DNF incorporation in any of the measured samples contributed to the saturated polarization (P_S) without leading to an increase in the remanent polarization, which was interpreted as an increase in the dielectric character of the device. The dielectric contribution measured as P_S-P_r to the polarization was maximized for the $DNF_{0.14}AN_{0.86}F_4TCNQ$ solid solutions sample, which indicates a dependence on both the ferroelectric structural phase and composition (DNF incorporation) and attributed to disordered and reversible dimerization along the CT stacks. In the original AN-F_4TCNQ report, it was noted that rotation of AN in the AN-F_4TCNQ cocrystal leads to disruption and symmetrization of the dimerization pattern along the *a*-axis. Both the decrease in molecular volume between AN and DNF and the disorder of DNF in the room temperature crystal structure of the DNF-F_4TCNQ cocrystal structure suggest that the barrier to rotation of DNF is lower than that for AN, suggesting that DNF cannot productively contribute to ferroelectricity in $DNF_{X}AN_{(1-X)}F_4TCNQ$ solid solutions. Given the size difference between AN and DNT and the room temperature crystal structure of the DNT-F_4TCNQ cocrystal, it is predicted that DNT incorporation could productively contribute to ferroelectricity, although advancements must first be made in ferroelectric device construction for this material.

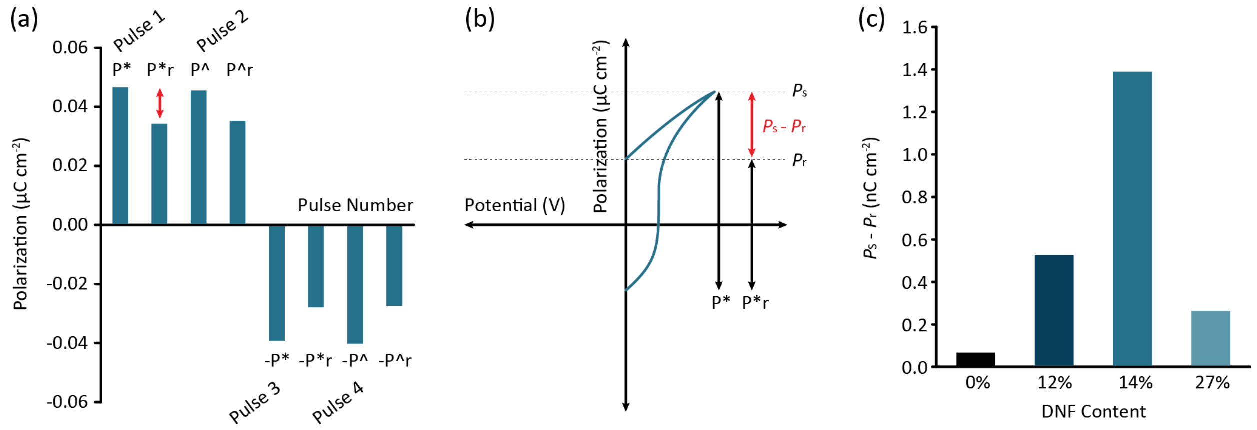

Figure 6.12. PUND Results for $DNF_{X}AN_{(1-X)}F_4TCNQ$ Single Crystals

(a) PUND data for $DNF_{0.14}AN_{0.86}F_4TCNQ$ single crystals with polarization responses to V_{max} pulses labeled as (+/-)P*, (+/-)P*r, (+/-)P^, and (+/-)P^r. (b) Diagram of a polarization hysteresis loop defining P*, P*r, P_S, P_r, and P_S - P_r. (c) P_S - P_r values for various $DNF_{X}AN_{(1-X)}F_4TCNQ$ solid solution compositions.

6.3 Conclusion

Room temperature ferroelectricity in the CT cocrystal AN-F_4TCNQ arises from thermally-activated rotation of AN at 68 °C. This is in contrast to conventional models of ferroelectricity in CT cocrystals, which claim that the transition between neutral and ionic CT states is the driving force for ferroelectricity. To investigate the mechanistic discrepancy between room-temperature ferroelectricity in AN-F_4TCNQ and low-temperature ferroelectricity in traditional CT ferroelectric cocrystals, the effects of increasing the population of ionic CT states in the AN-F_4TCNQ structure were investigated by doping in varying concentrations of the dopant molecules DNF and DNT, which were computationally predicted to increase the degree of CT in AN-F_4TCNQ. It was found that up to 14 mol% of DNF and 12 mol% DNT could be incorporated into the AN-F_4TCNQ ferroelectric structural phase without loss of the ferroelectric-to-paraelectric transition. Incorporation of DNF and DNT lead to increases in the average degree of CT of 0.3 e (increase of 0.1 e) and 0.7 e (increase of 0.5 e) in the ferroelectric phase, respectively. The increase in ionicity of the ferroelectric solid solution did not lead to a neutral-to-ionic transition at the T_C in $DNT_{0.12}AN_{0.88}F_4TCNQ$. Electrical characterization of $DNF_XAN_{(1-X)}F_4TCNQ$ solid solutions revealed that DNF incorporation into the ferroelectric structural phase leads to an increase in the dielectric character of the material without an increase in remanent polarization, which was ascribed to a lower energetic barrier to polarization switching for DNF due to the slight decrease in molecular volume relative to AN. Given these conclusions, it is predicted that DNT incorporation into AN-F_4TCNQ will lead to increases in the remanent polarization, although additional optimization of the crystallization methods towards $DNT_XAN_{(1-X)}F_4TCNQ$ solid solutions must first be made to enable construction of $DNT_XAN_{(1-X)}F_4TCNQ$ devices for electrical characterization.

6.4 Experimental Methods

*6.4.1 Synthesis of 2H-naphtho[1,8-bc]furan-2-one (**1**)*

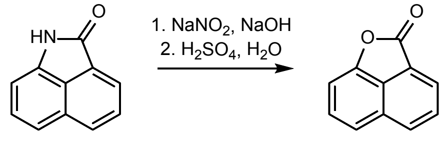

The synthesis of **1** was adapted from the literature.[35] Benz[cd]indol-2(1H)-one (1196 mg, 7.069 mmol) was refluxed in aqueous 0.5 M NaOH solution (60 mL) for 30 min, causing a color change from yellow to orange. The solution was cooled to 0 °C and $NaNO_2$ (501 mg, 7.261 mmol) in water (10 mL) was added to the solution of benz[cd]indol-2(1H)-one dropwise. This solution was added dropwise to a slurry of water and ice (150 mL) and concentrated H_2SO_4 (9 mL). The reaction contents were heated to 70 °C for 1h during which time a pale-yellow precipitate formed. The precipitate was collected by vacuum filtration, dissolved in ethyl acetate, and dried over anhydrous $MgSO_4$. The product was purified by column chromatography on silica gel using a 0-5% (v/v) ethyl acetate/hexanes solvent gradient (904 mg, 5.312 mmol, 75%). ^1H NMR data are consistent with the literature.[35]

*6.4.2 Synthesis of 8-(hydroxymethyl)naphthalen-1-ol (**2**)*

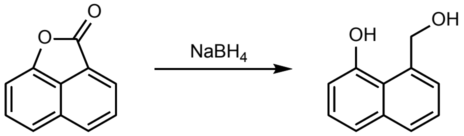

The synthesis of **2** was adapted from the literature.[35] Sodium borohydride was suspended in a solution of dry tetrahydrofuran (23 mL) and methanol (2 mL). The solution was cooled to 0 °C and a solution of intermediate **1** (904 mg, 5.312 mmol) in tetrahydrofuran (10 mL) was added dropwise to the suspension of sodium borohydride. The suspension stirred at 0 °C for 2 h. The reaction contents were quenched with water, diluted with 1 M HCl (100 mL), and the product extracted into ethyl acetate (3 x 50 mL). The organic fractions were combined and dried over anhydrous $MgSO_4$. The product was crystallized from ethyl acetate (854 mg, 4.902 mmol, 92%). ^1H NMR (400 MHz, acetone-d_6) δ 10.1 (s, 1H), 7.78 (d, 1H), 7. 42 (d, 2H), 7.36 (t, 1H), 7.34 (t, 1H), 6.98 (d, 1H), 5.48 (s, 1H), 5.12 (s, 2H).

6.4.3 Synthesis of Dihydronaphtho[1,8-bc]furan (DNF)

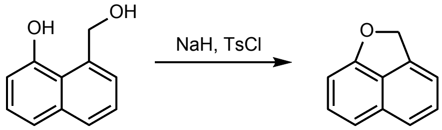

The synthesis of DNF was adapted from the literature.[36] NaH (60% dispersion in mineral oil, 193 mg, 4.83 mmol) was suspended in dry tetrahydrofuran (12 mL) and dry dimethylsulfoxide (4 mL) at room temperature. Intermediate **2** (398 mg, 2.23 mmol) was dissolved in tetrahydrofuran (2 mL) and added to the reaction suspension at room temperature. Tosyl chloride (435 mg, 2.28 mmol) was dissolved in tetrahydrofuran (2 mL) and added to the reaction suspension at room temperature. The reaction was heated to 70 °C for 7 h and cooled to room temperature. The reaction contents were quenched with water and the suspension diluted with 0.5 M HCl (100 mL). The product was extracted into ethyl acetate (3 x 50 mL). The organic fractions were combined and dried over anhydrous $MgSO_4$. The product was purified by column chromatography on silica gel using a 0-5% (v/v) ethyl acetate/hexanes solvent gradient (256 mg, 1.64 mmol, 72%). ^{1}H NMR (400 MHz, acetone-d_6) δ 7.65 (d, 1H), 7.53 (t, 1H), 7.38 (t, 1H), 7.32 (d, 1H), 7.24 (d, 1H), 6.66 (d, 1H), 5.81 (s, 2H).

*6.4.4 Synthesis of S-Naphthalen-1-yl Carbonochloridothioate (**3**)*

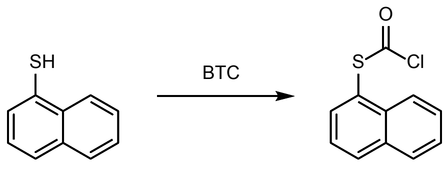

The synthesis of **3** was adapted from the literature.[37] Dry pyridine (1.6 mL) was added dropwise to a solution of 1-naphthalenethiol (785 mg, 4.899 mmol) and triphosgene (BTC, 4399 mg, 14.824 mmol) in dry dichloromethane (50 mL) at 0 °C, immediately forming a suspension. The suspension stirred at 0 °C for 3 h. The reaction contents were quenched with water (100 mL) and the product extracted in dichloromethane (3 x 50 mL). The organic fractions were combined, dried over anhydrous $MgSO_4$, and concentrated under reduced pressure. The product was purified by column chromatography on silica gel using a 0-15% (v/v) ethyl acetate/hexanes solvent gradient (908 mg, 4.077 mmol, 83%). ^{1}H NMR data are consistent with the literature.[37]

*6.4.5 Synthesis of 2-Naphtho[1,8-bc]thiophen-2-one (**4**)*

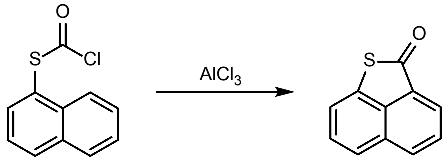

Synthesis of **4** was adapted from the literature.[37] A solution of intermediate **3** (908 mg, 4.077 mmol) in dry dichloromethane (mL) was added dropwise to a solution of aluminum trichloride (1630 mg, 12.224 mmol) in dry dichloromethane (180 mL). The reaction solution stirred at room temperature for 7 h, rapidly changing color from yellow to dark green. The reaction contents were quenched with water (200 mL) and the product extracted into dichloromethane (3x50 mL). The organic fractions were combined, dried over anhydrous $MgSO_4$, and concentrated under reduced pressure. The product was purified by column chromatography on silica gel using 0-10% (v/v) ethyl acetate/hexanes solvent gradient (736 mg, 3.952 mmol, 97%). ^{1}H NMR data are consistent with the literature.[37]

6.4.6 Synthesis of Dihydronaphtho[1,8-bc]thiophene (DNT)

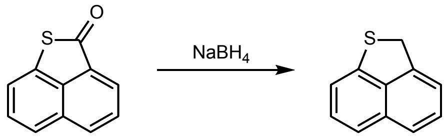

Sodium borohydride (118 mg, 2.96 mmol) was suspended in a solution of dry dichloromethane (50 mL) and methanol (2 mL). The solution was cooled to 0 °C and a solution of intermediate **4** (188 mg, 1.01 mmol) in dichloromethane (3 mL) was added dropwise to the suspension of sodium borohydride. The suspension stirred at 40 °C for 48 h. The reaction contents were quenched with water, diluted with 1 M HCl (50 mL), and the product extracted into dichloromethane (2x50 mL). The organic fractions were combined and dried over anhydrous $MgSO_4$. The product was purified by column chromatography on silica gel using hexanes (30 mg, 0.17 mmol, 17%). ^1H NMR (400 MHz, acetone-d_6) δ 7.65 (d, 1H), 7.46 (m, 3H), 7.36 (t, 1H), 7.22 (d, 1H), 4.83 (s, 2H).

6.4.7 Crystallization of $DNF_XAN_{(1-X)}F_4TCNQ$ Solid Solutions

Stock solutions of F_4TCNQ (88.49 mg, 3.20 x 10^{-1} mmol) in dry acetonitrile (1760 μL) and AN (24.58 mg, 1.59 x 10^{-1} mmol) in dry acetonitrile (550 μL) were prepared. For each solid solution sample, DNF was weighed out according to the masses given below and the corresponding volume of dry diethyl ether was added. To each sample of DNF in diethyl ether, AN in acetonitrile was added forming a colorless to pale-yellow solution. To this solution, F_4TCNQ in acetonitrile was added causing a color change to deep brown or deep purple. This solution was chilled to 0 °C for 6 min, precipitating brown blocky crystals with a green metallic sheen. The precipitate collected by vacuum filtration and stored at room temperature.

Table 6.6. Composition of $DNF_XAN_{(1-X)}F_4TCNQ$ Solid Solution Crystal Growth Solutions

	Mass DNF Theoretical/Actual	Volume Diethyl Ether	Volume AN Stock	Volume F_4TCNQ Stock
A	0 mg (0 mmol)/0 mg (0 mmol)	0 μL	100 μL	160 μL
B	0.45 (2.90E^{-3})/0.40 (2.56E^{-3})	10 μL	90 μL	160 μL
C	0.91 (5.81E^{-3})/0.87 (5.57E^{-3})	20 μL	80 μL	160 μL
D	1.36 (8.71E^{-3})/1.36 (8.71E^{-3})	30 μL	70 μL	160 μL
E	1.81 (1.16E^{-2})/1.90 (1.23E^{-2})	40 μL	60 μL	160 μL
F	2.26 (1.45E^{-2})/2.34 (1.50E^{-2})	50 μL	50 μL	160 μL
G	2.71 (1.74E^{-2})/2.70 (1.73E^{-2})	60 μL	40 μL	160 μL

H	3.17 (2.03E^{-2})/3.15 (2.02E^{-2})	70 µL	30 µL	160 µL
I	3.62 (2.32E^{-2})/3.60 (2.31E^{-2})	80 µL	20 µL	160 µL
J	4.07 (2.61E^{-2})/4.06 (2.60E^{-2})	90 µL	10 µL	160 µL
K	4.52 (2.90E^{-2})/4.51 (2.89E^{-2})	100 µL	0 µL	160 µL

6.4.8 Crystallization of $DNT_XAN_{(1-X)}F_4TCNQ$ Solid Solutions

Stock solutions of F_4TCNQ (89.26 mg, 3.23 x 10^{-1} mmol) in dry acetonitrile (1760 µL) and AN (24.62 mg, 1.60 x 10^{-1} mmol) in dry acetonitrile (550 µL) were prepared. For each solid solution sample, DNT was weighed out according to the masses given below and the corresponding volume of dry diethyl ether was added. To each sample of DNT in diethyl ether, AN in acetonitrile was added forming a colorless to pale-purple solution. To this solution, F_4TCNQ in acetonitrile was added causing a color change to deep brown or deep purple. This solution was chilled to 0 °C for 6 min, precipitating brown blocky crystals with a green metallic sheen. The precipitate collected by vacuum filtration and stored at 0 °C.

Table 6.7 Composition of $DNT_XAN_{(1-X)}F_4TCNQ$ Solid Solution Crystal Growth Solutions

	Mass DNT Theoretical/Actual	Volume Diethyl Ether	Volume AN Stock	Volume F_4TCNQ Stock
A	0 mg (0 mmol)/0 mg (0 mmol)	0 µL	100 µL	160 µL
B	0.50 (2.90E^{-3})/0.54 (3.08E^{-3})	10 µL	90 µL	160 µL
C	1.00 (5.81E^{-3})/1.02 (5.92E^{-3})	20 µL	80 µL	160 µL
D	1.50 (8.71E^{-3})/1.50 (8.71E^{-3})	30 µL	70 µL	160 µL
E	2.00 (1.16E^{-2})/1.99 (1.14E^{-2})	40 µL	60 µL	160 µL
F	2.50 (1.45E^{-2})/2.39 (1.39E^{-2})	50 µL	50 µL	160 µL
G	3.00 (1.74E^{-2})/2.98 (1.70E^{-2})	60 µL	40 µL	160 µL
H	3.50 (2.03E^{-2})/3.55 (2.03E^{-2})	70 µL	30 µL	160 µL
I	4.00 (2.32E^{-2})/3.97 (2.30E^{-2})	80 µL	20 µL	160 µL
J	4.50 (2.61E^{-2})/4.42 (2.57E^{-2})	90 µL	10 µL	160 µL
K	5.00 (2.90E^{-2})/5.02 (2.91E^{-2})	100 µL	0 µL	160 µL

6.4.9 Single Crystal X-Ray Determination

Single-crystal X-ray diffraction data were collected using a Rigaku XtaLAB Synergy-S X-ray diffractometer configured in a kappa goniometer geometry. The diffractometer is equipped with a low-temperature device and a PhotonJet-S microfocus Cu source ($\lambda = 1.54187$ Å) and operated at 50 kV and 1 mA. X-ray intensities were measured at 100 K or room temperature with the HyPix-6000HE detector placed 32.01 mm from the sample. The data were processed with CrysAlisPro version 38.46 (Rigaku Oxford Diffraction) and corrected for absorption. The structures were determined in OLEX2[38] using SHELXT[39] and refined using SHELXL[40]. All non-hydrogen atoms were refined anisotropically with hydrogen atoms placed at idealized positions. Single crystals were mounted on a 150 μm MiTeGen MicroMount using mineral oil.

6.4.10 Nuclear Magnetic Resonance Spectroscopy

^{1}H NMR measurements were carried out on Varian vnmrs 500 MHz spectrometer operating at room temperature, using 64 scans and a 10 second relaxation delay. Samples of $DNF_XAN_{(1-X)}F_4TCNQ$ and $DNT_XAN_{(1-X)}F_4TCNQ$ solid solutions were prepared by dissolution in acetone-d_6 within 10 min of collecting the ^{1}H NMR spectra. The ratio of DNF or DNT to AN for each spectrum was calculated by integration of the peaks using MestReNova v12.0.0-20080, Mestrelab Research, 2017.

6.4.11 Raman Spectroscopy

Raman spectra were collected using a Renishaw inVia Raman Microscope equipped with a Leica microscope, a 785 nm laser, 1200 lines/mm grating, a 65 μm slit, and a RenCam CCD detector. Spectra were collected in static mode centered about 2220 cm^{-1} and analyzed using the WiRE

3.4 software package (Renishaw) and OriginPro 8.6. Calibration was performed using a silicon standard in static mode centered about 500 cm^{-1}.

6.4.12 Differential Scanning Calorimetry

Differential scanning calorimetry (DSC) traces for each sample (~0.8 mg) were recorded on a TA Instruments Q20 DSC. All experiments were run in TzeroTM hermetic aluminum DSC pans with a heating rate of either 5 °C/min or 10 °C/min, covering a temperature range of -70 °C to 80 °C. The instrument was calibrated using an indium standard. DSC traces were analyzed using TA Universal Analysis 2000, V 4.5A, build 4.5.0.5.

6.4.13 Ferroelectric Measurements

Electrical measurements were taken on single crystals contacted with silver paint. BFDH morphology prediction was produced by Mercury CSD 4.1.3 offered by the CCDC and used to guide the placement of the electrode contacts on the (100) and (-100) faces. The P-E hysteresis loops were collected at room temperature on a ferroelectric testing probe station (Radiant Technologies Inc Ferroelectric Test System) operated using Vision Data Acquisition Software (Radiant Technologies Inc) using an alternating triangular double-wave field (preset-delay-measurement). PUND tests were also performed on single crystals using the Radiant Technologies Inc Ferroelectric Testing System. The data provided in this manuscript were collected from twelve representative single crystals. Despite guidance from morphology predictions, contact placement was imperfect for several samples due to the blocky morphology of the crystal, and these samples showed unreliable and unsymmetrical polarization loops with no remanent behavior. It was concluded that, although sample measurements were reliable for well-placed electrodes, the P-E measurements are very specific to sample orientation.

6.4.14 Computational Methods

Calculation of the frontier molecular orbital energy positions and molecular volumes on gas-phase equilibrium geometries of F_4TCNQ, AN, DNF, and DNT were performed with the B3LYP functional and the 6-311G(d,p) basis set using the Spartan ’16 Q-Chem package. Isosurfaces for determination of the molecular volumes were drawn at a potential of 0.002 electrons au^{-3}.

6.4.15 Crystal Structure Comparison

Crystal structures were compared using the Crystal Packing Similarity Wizard available in the Materials Module offered through Mercury CSD 4.1.3 (CCDC). A packing shell of 15 molecules, distance tolerance of 20%, and angular tolerance of 50% were used and ‘Allow Molecular Differences’ enabled for comparison.

6.5 References

1. Soos, Z. G., Theory of Pi-Molecular Charge-Transfer Crystals. *Annu. Rev. Phys. Chem.* **1974,** *25*, 121-153.
2. Torrance, J. B.; Vazquez, J. E.; Mayerle, J. J.; Lee, V. Y., Discovery of a Neutral-to-Ionic Phase Transition in Organic Materials. *Phys. Rev. Lett.* **1981,** *46*, 253-257.
3. Torrance, J. B.; Girlando, A.; Mayerle, J. J.; Crowley, J. I.; Lee, V. Y.; Batail, P., Anomalous Nature of Neutral-to-Ionic Phase Transition in Tetrathiafulvalene-Chloranil. *Phys. Rev. Lett.* **1981,** *47*, 1747-1750.
4. Horiuchi, S.; Okimoto, Y.; Kuami, R.; Tokura, Y., Ferroelectric Valence Transition and Phase Diagram of a Series of Charge-Transfer Complexes of 4,4'-Dimethyltetrathiafulvalene and Tetrahalo-p-benzoquinones. *J. Am. Chem. Soc.* **2001,** *123*, 665-670.

5. Horiuchi, S.; Kumai, R.; Okimoto, Y.; Tokura, Y., Chemical approach to neutral-ionic valence instability, quantum phase transition, and relaxor ferroelectricity in organic charge-transfer complexes. *Chem. Phys.* **2006,** *325*, 78-91.
6. Shokaryev, I.; Buurma, A. J. C.; Jurchescu, O. D.; Uijttewaal, M. A.; de Wijs, G. A.; Palstra, T. T. M.; de Groot, R. A., Electronic Band Structure of Tetracene-TCNQ and Perylene-TCNQ Compounds. *J. Phys. Chem. A* **2008,** *112*, 2497-2502.
7. Goetz, K. P.; Vermeulen, D.; Payne, M. E.; Kloc, C.; McNeil, L. E.; Jurchescu, O. D., Charge-transfer complexes: new perspectives on an old class of compounds. *J. Mater. Chem. C* **2014,** *2*, 3065-3076.
8. Goud, N. R.; Matzger, A. J., Impact of Hydrogen and Halogen Bonding Interactions on the Packing and Ionicity of Charge-Transfer Cocrystals. *Cryst. Growth Des.* **2017,** *17*, 328-336.
9. Horiuchi, S.; Okimoto, Y.; Kumai, R.; Tokura, Y., Quantum Phase Transition in Organic Charge-Transfer Complexes. *Science* **2003,** *299*.
10. Chen, S.; Xiao, C. Z., Design of Ferroelectric Organic Molecular Crystals with Ultrahigh Polarization. *J. Am. Chem. Soc.* **2014,** *136*, 6428-6436.
11. Horiuchi, S.; Kobayashi, K.; Kumai, R.; Minami, N.; Kagawa, F.; Tokura, Y., Quantum ferroelectricity in charge-transfer complex crystals. *Nat. Commun.* **2015,** *6*, 7469.
12. Tayi, A. S.; Kaeser, A.; Matsumoto, M.; Aida, T.; Stupp, S. I., Supramolecular ferroelectrics. *Nat. Chem.* **2015,** *7*, 281-294.
13. Burroughes, J. H.; Jones, C. A.; Friend, R. H., New semiconductor device physics in polymer diodes and transistors. *Nature* **1988,** *335*, 137-141.
14. Burroughes, J. H.; Bradley, D. D. C.; Brown, A. R.; Marks, R. N.; Mackay, K.; Friend, R. H.; Burns, P. L.; Holmes, A. B., Light-emitting diodes based on conjugated polymers. *Nature* **1990,** *347*, 539-541.
15. Su, Y.-W.; Lan, S.-C.; Wei, K.-H., Organic phtovoltaics. *Mater. Today* **2012,** *15*, 554-562.
16. Kaur, N.; Singh, M.; Pathak, D.; Wagner, T.; Nunzi, J. M., Organic materials for photovoltaic application: Review and mechanism. *Synth. Met.* **2014,** *190*, 20-26.
17. Anthony, J. E., The Larger Acenes: Versatile Organic Semiconductors. *Angew. Chem. Int. Ed.* **2008,** *47*, 452-483.
18. Zhu, L.; Yi, Y.; Li, Y.; Kim, E.-G.; Coropceanu, V.; Brédas, J.-L., Prediction of Remarkable Ambipolar Charge-Transport Characteristics in Organic Mixed-Stack Charge-Transfer Crystals. *J. Am. Chem. Soc.* **2012,** *134*, 2340-2347.
19. Goud, N. R.; Zhang, X.; Bredas, J.-L.; Coropceanu, V.; Matzger, A. J., Discovery of Non-linear Optical Materials by Function-Based Screening of Multi-component Solids. *Chem* **2018,** *4*, 150-161.
20. Kobayashi, K.; Horiuchi, S.; Kumai, R.; Kagawa, F.; Murakami, Y.; Tokura, Y., Electronic Ferroelectricity in a Molecular Crystal with Large Polarization Directing Antiparallel to Ionic Displacement. *Phys. Rev. Lett.* **2012,** *108*, 237601.
21. Horiuchi, S.; Tokura, Y., Organic Ferroelectrics. *Nature* **2008,** *7*, 357-366.
22. Tokura, Y.; Koshihara, S.; Iwasa, Y.; Okamoto, H.; Komatsu, T.; Koda, T.; Iwasawa, N.; Saito, G., Domain-wall dynamics in organic charge-transfer compounds with one-dimensional ferroelectricity. *Phys Rev. Lett.* **1989,** *63*, 2405-2408.
23. Horiuchi, S.; Kumai, R.; Okimoto, Y.; Tokura, Y., Design of quantum neutral-ionic phase transition in organic charge-transfer complexes. *Synth. Met.* **2003,** *133-134*, 615-618.

24. Castagnetti, N.; Kociok-Köhn, G.; Da Como, E.; Girlando, A., Temperature-induced valence instability in the charge-transfer crystal TMB-TCNQ. *Phys. Rev. B* **2017,** *95*, 0241011-0241017.
25. Wiscons, R. A.; Goud, N. R.; Damron, J. T.; Matzger, A. J., Room Temperature Ferroelectricity in an Organic Cocrystal. *Angew. Chem. Int. Ed.* **2018,** *57*, 9044-9047.
26. Lieffrig, J.; Jeannin, O.; Frąckowiak, A.; Olejniczak, I.; Świetlik, R.; Dahaoui, S.; Aubert, E.; Espinosa, E.; Auban-Senzier, P.; Fourmigué, M., Charge-Assisted Halogen Bonding: Donor–Acceptor Complexes with Variable Ionicity. *Chem. Euro. J.* **2013,** *19*, 14804-14813.
27. Castagnetti, N.; Masino, M.; Rizzoli, C.; Girlando, A.; Rovira, C., Mixed stack charge transfer crystals: Crossing the neutral-ionic borderline by chemical substitution. *Phys. Rev. Mater.* **2018,** *2*, 024602.
28. Nesse, W. D., *Introduction to Mineralogy*. Oxford University Press: New York, 2000.
29. Steed, J. W.; Atwood, J. L., *Supramolecular Chemistry*. 2 ed.; Wiley: Oxford, 2009; p 1002.
30. Lusi, M., Engineering Crystal Properties through Solid Solutions. *Cryst. Growth Des.* **2018,** *18*, 3704-3712.
31. Wiscons, R. A.; Coropceanu, V.; Matzger, A. J., Quaternary Charge-Transfer Solid Solutions: Electronic Tunability through Stoichiometry. *Chem. Mater.* **2019**.
32. Kitaigorodsky, A. I., *Mixed Crystals*. Springer: Berlin, 1984.
33. West, A. R., *Solid State Chemistry and its Applications*. 2 ed.; Wiley: New York, 2014.
34. Sutton, A. L.; Abrahams, B. F.; D'Alessandro, D. M.; Hudson, T. A.; Robson, R.; Usovb, P. M., Structural and optical investigations of charge transfer complexes involving the radical anions of TCNQ and F4TCNQ. *CrystEngComm* **2016,** *18*, 8906-8914.
35. Cammidge, A. N.; Öztürk, O., Selective Synthesis of meso-Naphthylporphyrins. *J. Org. Chem.* **2002,** *67*, 7457-7464.
36. Berry, D.; Smith, D. C. C., 2*H*-naphtho[1,8-*bc*]furan and 8-hydroxy-1-naphthaldehyde. *J. C. S. Perkin I* **1972**, 699-704.
37. Mitsudo, K.; Murakami, T.; Shibasaki, T.; Inada, T.; Mandai, H.; Ota, H.; Suga, S., Facile Synthesis of Naphthothiophenone Derivatives and Anthradithiophenedione via Friedel–Crafts Acylation and Their Fundamental Properties. *Synlett* **2016,** *27*, 2327-2332.
38. Dolomanov, O. V.; Bourhis, L. J.; Gildea, R. J.; Howard, J. K.; Puschmann, H., *OLEX2*: a complete structure solution, refinement and analysis program. *J. Appl. Cryst.* **2009,** *42*, 339-341.
39. Sheldrick, G. M., *SHELXT* - Integrated space-group and crystal-structure determination. *Acta Cryst.* **2017,** *A71*, 3-8.
40. Sheldrick, G. M., Crystal structure refinement with *SHELXL*. *Acta Cryst.* **2015,** *C71*, 3-8.